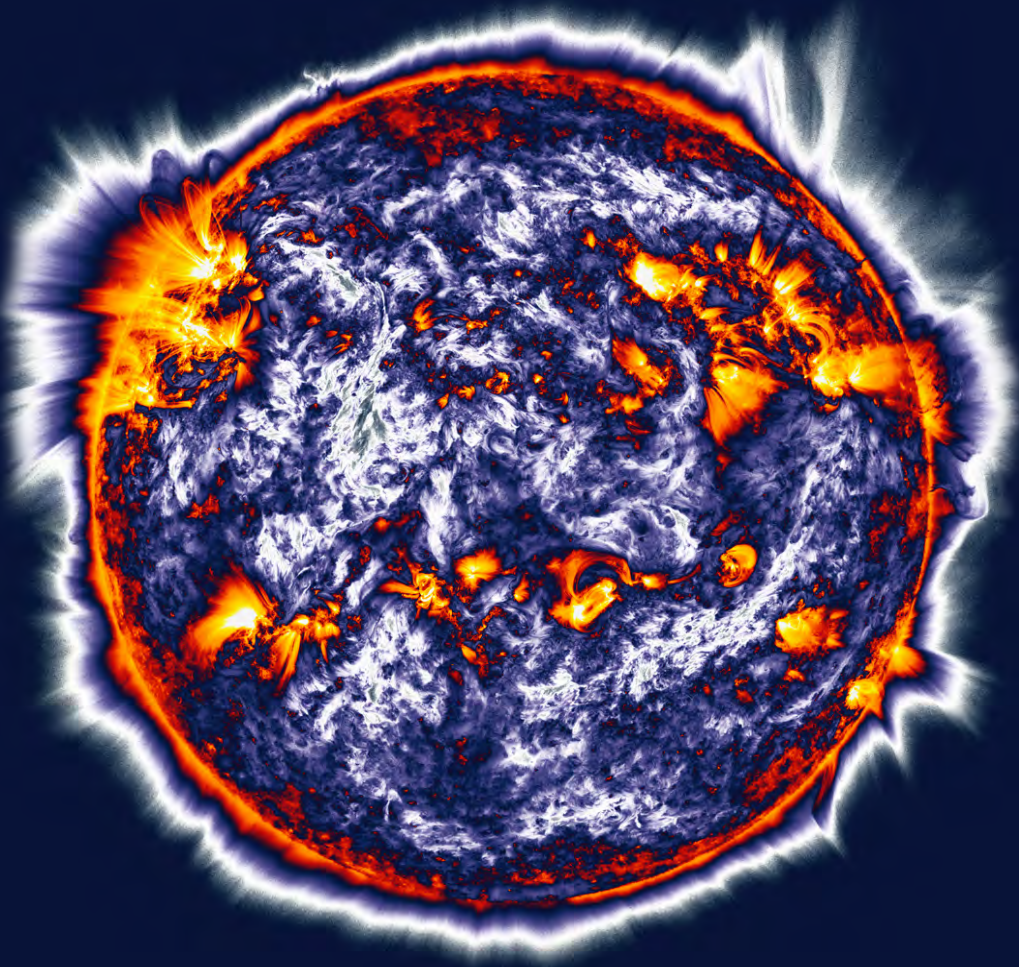


# 2018

---

Los Alamos Space Weather Summer School  
Research Reports



Jesse R. Woodroffe (*Editor*)

Cover image: NASA image of sun as observed by Solar Dynamics Observatory with additional spatial structure revealed through the application of a gradient filter (<https://svs.gsfc.nasa.gov/11105>)

# 2018

---

Los Alamos Space Weather Summer School  
Research Reports

Jesse R. Woodroffe  
*(Editor)*



# 2018

---

## Los Alamos Space Weather Summer School Research Reports

### *Preface*

The seventh Los Alamos Space Weather Summer School was held June 4<sup>th</sup> – July 27<sup>th</sup>, 2018 at Los Alamos National Laboratory (LANL). With renewed support from the Center for Space and Earth Sciences (CSES), we hosted a new class of seven students from various U.S. and foreign research institutions. The summer school curriculum includes a series of structured lectures as well as mentored research. Lecture topics including general and specialized topics in the field of space weather were given by a number of researchers affiliated with LANL.

Students were given the opportunity to engage in research projects through a mentored practicum experience. Each student works with one or more LANL-affiliated mentors to execute a collaborative research project, typically linked with a larger on-going research effort at LANL and/or the student's PhD thesis research. This model provides a valuable learning experience for the student while developing the opportunity for future collaboration.

This report includes a summary of the research efforts fostered and facilitated by the Space Weather Summer School. These reports should be viewed as work-in-progress as the short session typically only offers sufficient time for preliminary results. At the close of the summer school session, students present a summary of their research efforts.

It has been an honor for me to serve as the director of the Los Alamos Space Weather Summer School, and I am indebted to director emerita Misa Cowee for her assistance in so many things. I am grateful for all the administrative and logistical help I have received in organizing the program. Most of all, I am proud of the work done by the students, mentors and lecturers—their dedicated effort and unfailing professionalism were key to allowing our program to be successful.

Los Alamos, NM  
December 2018

Dr. Jesse Woodroffe  
*Summer School Director*

# 2018

---

## Los Alamos Space Weather Summer School Research Reports

### *New students*

Valerie Bernstein  
Shibaji Chakraborty  
Xu Liu  
Mykhaylo Shumko  
Talwinder Singh  
Alexandra Wold  
Lloyd Woodham

*University of Colorado Boulder*  
*Virginia Polytechnic Institute and State University*  
*University of Texas at Dallas*  
*Montana State University*  
*University of Alabama in Huntsville*  
*University of Colorado Boulder*  
*University College, London, UK*

# 2018

---

## Los Alamos Space Weather Summer School Research Reports

### *Project Reports*

<i>The Effect of Helium on Low Earth Orbit Atmospheric Drag</i> <b>Mentor:</b> Andrew Walker and Lisa Winter <b>Student:</b> Valerie Bernstein .....	1
<i>Quantifying Uncertainty in Space Weather Forecasting</i> <b>Mentor:</b> Steven Morley <b>Student:</b> Shibaji Chakraborty .....	11
<i>Global Simulation of Electron Cyclotron Harmonic Wave Instability in a Storm-time Magnetosphere</i> <b>Mentor:</b> Vania Jordanova and Miles Engel <b>Student:</b> Xu Liu .....	23
<i>Systematic Energy Spectra Uncertainty for Particle Detectors</i> <b>Mentors:</b> Brian Larsen and Phillip Fernandes <b>Student:</b> Mykhaylo Shumko .....	31
<i>Deriving Coronal Shock Properties from MHD Coronal Mass Ejection Simulations</i> <b>Mentor:</b> Fan Guo <b>Student:</b> Talwinder Singh.....	41
<i>Measuring Geomagnetic Cutoff with GPS Energetic Proton Data</i> <b>Mentor:</b> Matthew Carver and Steven Morley <b>Student:</b> Alexandra Wold .....	49
<i>Using High-Resolution 3D Hybrid Simulations to Investigate Plasma Turbulence at Ion-Kinetic Scales</i> <b>Mentors:</b> Misa Cowee and Xiangrong Fu <b>Student:</b> Lloyd Woodham .....	61

# 2018

---

## Los Alamos Space Weather Summer School Research Reports

### *Pictures*



#### **Class of 2018 Students and Mentors**

*(Students indicated in bold.) Back row (left to right): Matthew Carver, Steven Morley, **Shibaji Chakraborty**, **Xu Liu**, Phillip Fernandes, Miles Engel, Reiner Friedel, **Lloyd Woodham**, Andrew Walker; Front row (left to right): Xiangrong Fu, **Mykhaylo Shumko**, **Valerie Bernstein**, **Alexandra Wold**, Jesse Woodroffe, **Talwinder Singh**, Vania Jordanova, Fan Guo, Misa Cowee. Not Shown: Brian Larsen, Lisa Winter.*



# 2018

## Los Alamos Space Weather Summer School Research Reports

### *Lectures*

Introduction to the Magnetosphere .....	<i>Geoff Reeves</i>
Introduction to the Solar Wind .....	<i>Joe Borovsky</i>
Overview of LANL's Space Program .....	<i>Brian Larsen</i>
Particle Transport and Adiabatic Convection .....	<i>Michael Henderson</i>
Geomagnetic Storms: Ring Current and Plasmasphere Dynamics .....	<i>Vania Jordanova</i>
Comparative Magnetospheres .....	<i>Michelle Thomsen</i>
Magnetosphere-Ionosphere Coupling .....	<i>Jesse Woodroffe</i>
Historical Space Weather.....	<i>Delores Knipp</i>
The Sun and Solar Activity.....	<i>Lisa Winter</i>
Radiation Effects in Electronics .....	<i>Heather Quinn</i>
Atmospheric Drag .....	<i>Andrew Walker</i>
Hybrid and Particle-in-Cell Simulations .....	<i>Xiangrong Fu</i>
Radiation Effects in Aviation .....	<i>Stephen Wender</i>
Radio Waves in Geospace.....	<i>Jesse Woodroffe</i>
Quiet-time Evolution of the Radiation Belts .....	<i>Jean-Francois Ripoll</i>
Introduction to Magnetic Reconnection .....	<i>Ari Le</i>
Detectors for High Energy Particles, X-Rays, and Gamma rays.....	<i>Richard Schirato</i>
Spacecraft Charging.....	<i>Mick Denton</i>



# 2018

---

## Los Alamos Space Weather Summer School Research Reports

### *Sponsors*

Center for Space and Earth Sciences (CSES) at LANL

### *Contact Information*

Dr. Jesse Woodroffe  
Los Alamos Space Weather Summer School  
P.O. Box 1663, MS B241  
Los Alamos National Lab, NM 87545

Dr. Misa Cowee  
Los Alamos Space Weather Summer School  
P.O. Box 1663, MS B241  
Los Alamos National Lab, NM 87545

<http://www.swx-school.lanl.gov/>

### *Publication Release*

LA-UR 18-31636

# The Effect of Helium on Low Earth Orbit Atmospheric Drag

Valerie Bernstein

*University of Colorado Boulder, Boulder, CO 80309*

Andrew Walker

*Los Alamos National Laboratory, Los Alamos, NM 87545*

Lisa Winter

*Los Alamos National Laboratory, Los Alamos, NM 87545*

---

## Abstract

Atmospheric drag describes the perturbing force of the atmosphere on the orbital trajectories of Low Earth Orbit (LEO) objects and depends primarily on the spacecraft drag coefficient and the atmospheric mass density of the space environment. In a quiet, contracted thermosphere, mass transport processes governed by vertical diffusion and large scale meridional flow allow helium to concentrate around winter hemisphere polar latitudes at ~500 km altitude. Atmospheric drag is a significant source of uncertainty in orbital trajectories at these altitudes, and the effect of helium on atmospheric drag has not yet been quantified. The Thermosphere-Ionosphere-Electrodynamics General Circulation Model (TIEGCM) is a physics-based model of the Earth's upper atmosphere maintained by the National Center for Atmospheric Research (NCAR) that offers the ability to study the effects of including or neglecting atmospheric helium on atmospheric mass density and spacecraft drag coefficient estimates. To examine the spatial and temporal effects of helium on satellite drag, we simulate TIEGCM atmospheres with and without helium along the orbital trajectories of two LEO satellites, the Challenging Minisatellite Payload (CHAMP) at ~375 km altitude and the Gravity Recovery and Climate Experiment (GRACE) at ~500 km altitude. Physics-based atmospheric simulations were performed with TIEGCM for six one-week time periods. The breakdown of simulation time periods includes three active, moderate, and quiet geomagnetic activity time periods selected for both this past solar maximum and solar minimum. We compare TIEGCM atmospheric mass densities with and without helium included as a major species with accelerometer-derived density estimates for CHAMP and GRACE revised based on newly-computed drag coefficients modeled for TIEGCM atmospheres with and without helium during these time periods to identify the strengths and weaknesses of TIEGCM estimates attributed to helium. Including helium in TIEGCM is found to improve TIEGCM density predictions and significantly increase the drag coefficient for GRACE during quiet solar minimum conditions at polar latitudes in the winter hemisphere. We additionally compare TIEGCM atmospheres with and without helium to atmospheres simulated by the Naval Research Laboratory's Mass Spectrometer and Incoherent Scatter Extended Model (NRLMSISE-00), an empirical model of the atmosphere that includes helium, in order to assess trends in the variations in helium predicted from different atmospheric models. TIEGCM with helium consistently overestimates the densities and underestimates the drag coefficients compared to those associated with MSIS atmospheres during solar minimum, and this could be attributed to the fact that hydrogen, which is included in MSIS but neglected in TIEGCM, had a significant role in the atmospheric dynamics at GRACE altitudes during this past solar minimum.

*Keywords:* satellite drag, atmospheric density, drag coefficient, TIEGCM, CHAMP, GRACE

---

*Email addresses:* [valerie.bernstein@colorado.edu](mailto:valerie.bernstein@colorado.edu) (Valerie Bernstein), [awalker@lanl.gov](mailto:awalker@lanl.gov) (Andrew Walker), [lmwinter@lanl.gov](mailto:lmwinter@lanl.gov) (Lisa Winter)

## 1. Introduction

Atmospheric drag describes the perturbing force of the atmosphere on the orbital trajectory of a satellite at altitudes between 200 and 1000 km, which is a region in the Low Earth Orbit (LEO) space environment. Atmospheric drag produces the largest source of uncertainty in precise orbit determination for LEO objects (Marcos et al., 2006). The force exerted by atmospheric drag on an orbiting object is proportional to a quantity known as the drag coefficient ( $C_D$ ), the area-to-mass ratio of the object, the density of the space environment through which the object is moving, and the velocity of the object relative to the atmosphere.

$$\vec{a}_{drag} = -\frac{1}{2}C_D\frac{A}{m}\rho v_{rel}^2\frac{\vec{v}_{rel}}{|\vec{v}_{rel}|} \quad (1)$$

Both the drag coefficient and the atmospheric mass density are highly variable and are governed by atmospheric dynamics. The drag coefficient depends on the temperature of the surface of a satellite, the atmospheric temperature, the concentrations of atmospheric constituent species, and the way that particles are reflected from the satellite surface. Atmospheric density depends on a range of phenomena and conditions, such as solar geomagnetic activity levels, thermospheric winds and flow patterns, and gas interaction processes. Accurate modeling of the drag coefficient and the mass density is thus critical for precise positioning for Earth-orbiting satellites.

One recent area of research that has been of interest to the atmospheric density modeling community is the role of helium in density variations (Thayer et al., 2012; Liu et al., 2014a,b). The Winter Helium Bulge (Keating and Prior, 1967; Cageao and Kerr, 1984) refers to the abundance of helium at polar latitudes in the winter hemisphere during solar minimum conditions at  $\sim 500$  km altitude. An example of this phenomenon is shown in Figure 1. Figure 1 displays maps of the helium concentration represented as a fraction of the atmospheric composition at an instant of time in December of 2008, right in the middle of a very quiet solar minimum. In Figure 1a, a significant amount of helium is revealed at northern polar latitudes around 500 km. The approximate orbital altitudes of two LEO satellites, GRACE and CHAMP, are included on this plot to show the estimated amount of helium that they may have encountered along their orbits during this time period. Figure 1b shows helium across all latitudes and longitudes at an altitude of  $\sim 500$  km. Again, helium accumulates at polar latitudes in the northern hemisphere. This helium behavior can be explained by the vertical transport of lighter species upward and heavier species downward, known as vertical diffusion. Downward winds in the winter hemisphere enhance the helium concentration at these altitudes, while upward winds in the summer hemisphere depress the helium concentration at these altitudes because helium is pushed upward. The direction of these vertical winds is governed by the mass continuity equation. Additionally, high pressure in the summer hemisphere from high temperatures drives the horizontal transport of species toward the lower pressure winter hemisphere through large scale meridional flow, which explains the winter polar signature of the helium abundance. Helium makes more of a presence during solar minimum than during solar maximum because during solar maximum the atmosphere has more energy which leads to enhanced exospheric escape and high altitude winds that decrease polar helium concentrations. During solar minimum the atmosphere is contracted which allows more helium to accumulate at lower altitudes around the winter poles.

Most physics-based models of the atmosphere do not include helium (Liu, 2013). This is because the LEO environment is typically considered to be dominated by either molecular nitrogen (at lower altitudes) or atomic oxygen (at higher altitudes where satellite drag is a concern). However, an atmosphere dominated by helium instead of oxygen would increase the drag coefficient and decrease the mass density experienced by an orbiting satellite (Liu, 2013) because helium is much lighter than oxygen.

## 2. Methodology

We are interested in understanding where and when helium has the most significant impact on satellite drag. We approach this question by examining atmospheric simulations from the Thermosphere-Ionosphere-Electrodynamics General Circulation Model (TIEGCM) (Richmond et al., 1992) generated both with helium included as a major constituent and without helium included as a major constituent. In order to assess the accuracy of the TIEGCM simulations with and without helium, we compare the model results with observations from the CHAMP and GRACE satellites. Thus employing CHAMP and GRACE accelerometer-inferred atmospheric density data allows us to assess whether or not including helium as a major constituent makes TIEGCM better at predicting the measured state of

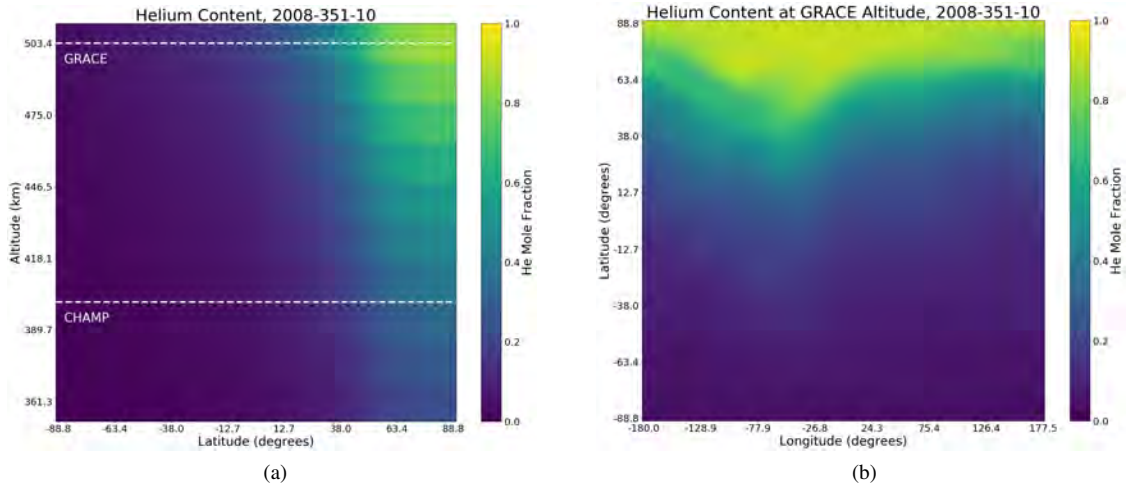


Figure 1: (a) Helium fractional concentration modeled by TIEGCM as a function of altitude and latitude for a given longitude and instant of time. CHAMP and GRACE approximate orbital altitudes are shown to reveal the helium they encountered at this time and position. (b) Helium concentration as a function of latitude and longitude at  $\sim 500$  km (GRACE’s orbital altitude) for an instant of time.

the atmosphere. Additionally, we want to determine how TIEGCM atmospheres with and without helium compare to atmospheres simulated by the Naval Research Laboratory’s Mass Spectrometer and Incoherent Scatter Extended (NRLMSISE-00, or MSIS) model (Picone et al., 2002). MSIS is an empirical model of Earth’s atmosphere that uses mass spectrometer and incoherent scatter radar data, and the reason we employ it for comparison in this study is because it includes helium concentration in its outputs.

### 2.1. Observations

CHAMP and GRACE were two LEO satellites equipped with accelerometers that have been used to probe atmospheric density. CHAMP was the Challenging Minisatellite Payload launched to investigate the gravity, magnetic, and electric fields around Earth from July of 2000 to September of 2010. CHAMP initially resided between 350 and 400 km. GRACE was the Gravity Recovery and Climate Experiment launched to accurately map Earth’s gravity field variations around  $\sim 500$  km altitude. The GRACE mission began in March of 2002 and ended in October of 2017 and incorporated two identical spacecraft, GRACE-A and GRACE-B, which flew  $\sim 220$  km apart, but we only examined GRACE-A data for this project. Both CHAMP and GRACE had high inclination angles of  $> 87$  degrees and nearly polar orbits, as shown in Figure 2. Thus, data from these satellites covers the full range of latitude and longitude values of interest to us.

### 2.2. TIEGCM Framework

TIEGCM offers us the ability to study the effects of including or neglecting helium in the atmosphere on mass density and drag coefficient estimates. TIEGCM is a physics-based model maintained by the National Center for Atmospheric Research (NCAR) that provides 3D numerical simulations of Earth’s upper atmosphere. It covers altitudes between  $\sim 100$  and  $\sim 600$  km and calculates compositional features and dynamics of the atmosphere. The latitude-longitude grid can be simulated with a resolution of either 2.5 degrees or 5 degrees. For each time step, the model solves the 3D momentum, energy, and continuity equations for neutral and ion species. The model assumes hydrostatic equilibrium and constant gravity force. The model input parameters are the F10.7 daily and 81-day averages to indicate the strength of UV and EUV radiation, Kp indices as indicative of auroral particle precipitation, electric field conditions from the magnetosphere, and lower boundary conditions. The model outputs the relative compositions of major and minor atmospheric constituent species, densities and temperatures of constituents, and neutral winds. TIEGCM can be executed with or without helium included as a major constituent (Sutton et al., 2015), which allows for comparison.

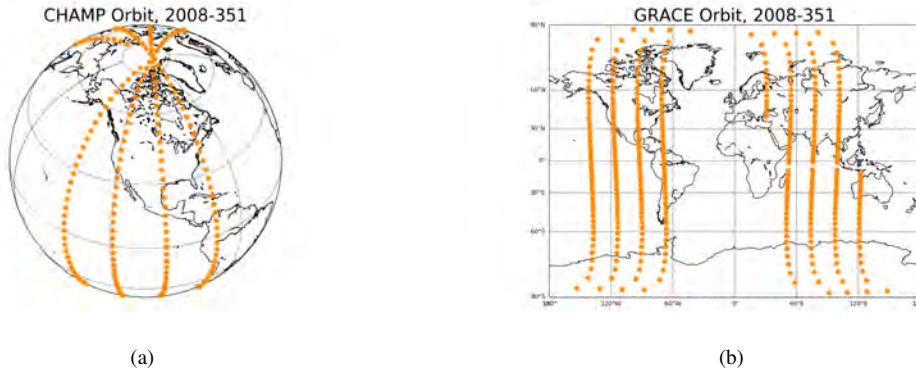


Figure 2: (a) Projection of 6 hours of CHAMP's orbit in December of 2008, on the 351st day of the year. (b) Projection of GRACE's orbit for the same time period.

### 2.3. Simulation Time Periods

We investigated the effect of helium on drag coefficients and mass densities for a variety of solar conditions. For both the previous solar maximum and solar minimum, we chose active, moderate, and quiet time periods based on archived DST indices<sup>1</sup>. The time periods are included in Table 1.

Table 1: Simulation Time Periods

	Solar Maximum	Solar Minimum
Active	2003/10/26 - 2003/11/02	2006/12/10 - 2006/12/17
Moderate	2003/06/13 - 2003/06/20	2009/07/17 - 2009/07/24
Quiet	2003/01/14 - 2003/01/21	2008/12/14 - 2008/12/21

For each of these six time periods, we simulated TIEGCM atmospheres for one week with and without helium with 2.5 degree latitudinal/longitudinal resolution using NCAR's supercomputer Cheyenne. We extracted CHAMP and GRACE orbital position information and prior accelerometer-inferred densities for the same time periods to allow for comparison. Additionally, we simulated MSIS atmospheres for mass density and constituent species' number densities comparisons. MSIS atmospheres for these time periods were generated based on Ap data and F10.7 averages<sup>2</sup>.

### 2.4. Obtaining Observed and Modeled Satellite Drag Parameters

Accelerometer data from both CHAMP and GRACE are used to obtain thermospheric density, and this has recently been done to a high level of accuracy by Sutton et al. (2007). This method involves setting the acceleration measurement equal to Eq. (1) and plugging in estimates for the drag coefficient and cross-sectional area of the satellite while neglecting atmospheric winds in the representation of relative velocity. Error is introduced in the mass density estimates when the drag coefficient is not accurately modeled, so Mehta et al. (2017) revised the Sutton et al. (2007) density estimates using more reliable drag coefficients computed with a response surface model that takes species concentrations as inputs. Physical drag coefficients can be modeled using the Test Particle Monte Carlo method which involves simulating shooting one particle into a volume, tracking the particle until it hits the satellite's surface, and calculating the force that the particle exerts on the satellite. Simulating these interactions for millions of particles gets computationally expensive quickly. Thus a response surface model was used as an alternative to cut down on computational effort, and it essentially operates as an interpolation scheme between 7 dimensions that can be trained

<sup>1</sup> Available from the World Data Center for Geomagnetism, Kyoto at <http://wdc.kugi.kyoto-u.ac.jp/dstdir/index.html>

<sup>2</sup> Available from Celestrak Space Weather Data at <http://celestrak.com/SpaceData/SW-All.txt>

by Test Particle Monte Carlo. Once a new, more robust drag coefficient has been estimated, taking the ratio of the old drag coefficient estimate to the new drag coefficient estimate and multiplying by the original density estimate allows for the determination of a newly calibrated density value.

$$\rho_{new} = \frac{C_{D_{old}}}{C_{D_{new}}} \rho_{old} \quad (2)$$

We employed this method to obtain revised drag coefficients and CHAMP and GRACE accelerometer-inferred mass densities with and without helium included in the response surface model. The fractional atmospheric constituent species inputs to the response surface model were obtained from TIEGCM atmospheres simulated with and without helium in order to arrive at revised drag coefficients. The old drag coefficient estimates were previously computed by Mehta et al. (2017) using MSIS species fractions as inputs to the response surface model, thus it is important to understand how TIEGCM and MSIS atmospheric species predictions compare in order to analyze the differences between the old and new drag coefficients.

TIEGCM atmospheric mass density and constituent species concentrations were parsed from TIEGCM model output along the observed orbital trajectories of CHAMP and GRACE for each of the six time periods with a one minute time resolution. Grid interpolations in altitude, latitude and longitude space were performed for the TIEGCM output variables of interest at each time step to obtain precise TIEGCM atmospheric estimates at locations along the orbits of CHAMP and GRACE. For the 2003 and 2006 time periods, TIEGCM provided model coverage for all CHAMP and GRACE orbital altitudes. However, for the 2008 and 2009 time periods, the atmosphere was contracted enough due to extremely quiet solar minimum conditions that the TIEGCM upper pressure level boundary dropped to altitudes below GRACE's altitudes along portions of GRACE's orbit. In these cases, extrapolations from TIEGCM altitudes to GRACE altitudes were performed to get TIEGCM atmospheric estimates along GRACE's orbit. TIEGCM mass density estimates along GRACE's orbit were obtained via exponential extrapolation from TIEGCM mass densities at the two uppermost altitudes covered by TIEGCM for the latitude and longitude of GRACE under the assumption of an isothermal atmosphere. TIEGCM He, N, N<sub>2</sub>, O and O<sub>2</sub> estimated concentrations along GRACE's orbit were obtained through linear interpolation from TIEGCM number densities at the two uppermost altitudes covered by TIEGCM for the latitude and longitude coordinates of GRACE. The results presented in Section 3 for quiet and contracted solar minimum conditions thus include these exponentially extrapolated TIEGCM mass densities and linearly extrapolated atmospheric species' concentrations in their analyses along the portions of GRACE's orbit not covered by TIEGCM model output.

### 3. Results

#### 3.1. CHAMP Altitudes

TIEGCM simulated atmospheres along CHAMP's orbit matched the profiles of the densities observed by CHAMP. This agreement was consistent for TIEGCM atmospheres modeled with helium and TIEGCM atmospheres modeled without helium as well as across all geomagnetic conditions. Representative examples of this behavior for CHAMP altitudes are shown in Figures 3 and 4. Both figures show the effect of including helium in TIEGCM on TIEGCM's ability to predict the atmospheric conditions seen by CHAMP. Figure 3 shows TIEGCM performance, both with and without helium, compared to CHAMP's measurements for a two-hour time period in the highly geomagnetically active solar maximum conditions of October of 2003. Figure 3a shows CHAMP-derived densities with and without helium as well as TIEGCM modeled densities with and without helium. Including or neglecting helium appears to have a negligible effect on density at this altitude region and this level of geomagnetic activity. Figure 3b shows the new drag coefficients modeled based on TIEGCM atmospheres with and without helium compared with the previous drag coefficient estimates based on an MSIS atmosphere. The drag coefficients computed with and without helium have essentially identical temporal profiles with a mean percent difference of 0.18% averaged over the full week of simulations for October of 2003. Figure 3c shows the mole fractions of the different atmospheric constituent species modeled by TIEGCM, both with and without helium, at this time along CHAMP's orbit. When helium is included in the model, it makes up a very small percentage of the atmosphere and thus has a negligible influence on density and drag coefficients.

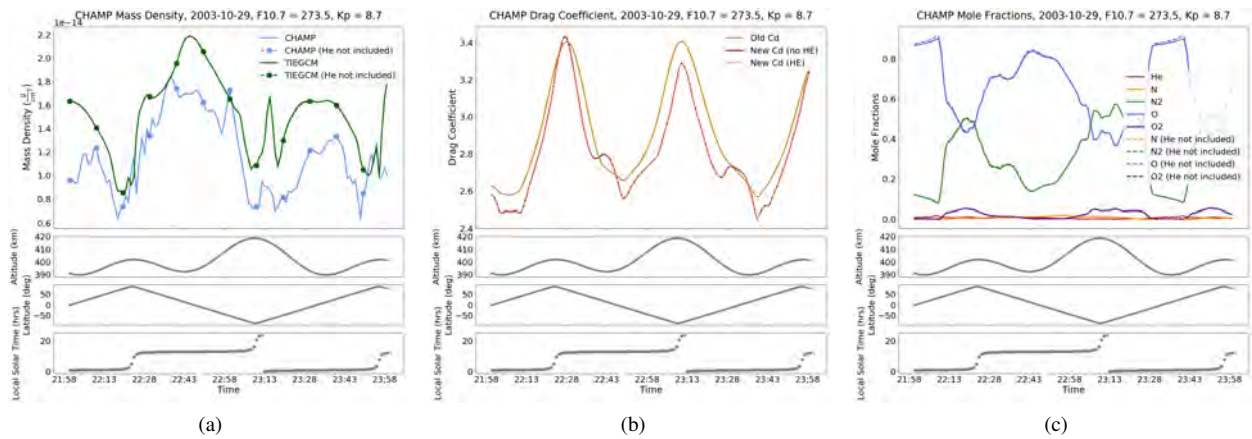


Figure 3: The three subpanels for each of (a), (b), and (c) indicate CHAMP's altitude, latitude in degrees, and local solar time along CHAMP's orbit during a two-hour time period in October of 2003. (a) CHAMP-derived densities with and without helium are included as the blue and blue dotted lines. TIEGCM modeled densities with and without helium are included as the green and green dotted lines. In this case, the blue solid and dotted lines match up perfectly, and the same behavior is displayed for the green solid and dotted lines. This indicates that the inclusion of helium does not impact atmospheric density at this altitude and level of geomagnetic activity. (b) The gold line represents the old, published drag coefficient values for GRACE computed from the response surface model based on MSIS atmospheric species concentrations. Newly computed drag coefficients based on a TIEGCM atmospheric composition without helium are shown in dark red, and newly computed drag coefficients based on a TIEGCM atmosphere that includes helium are shown in light orange. (c) Mole fractions of atmospheric species from TIEGCM without helium are shown by the dashed lines, while mole fractions of atmospheric species from TIEGCM with helium are included as the solid lines. Helium is displayed by the red line. This plot style and format is consistent throughout the remainder of this paper.

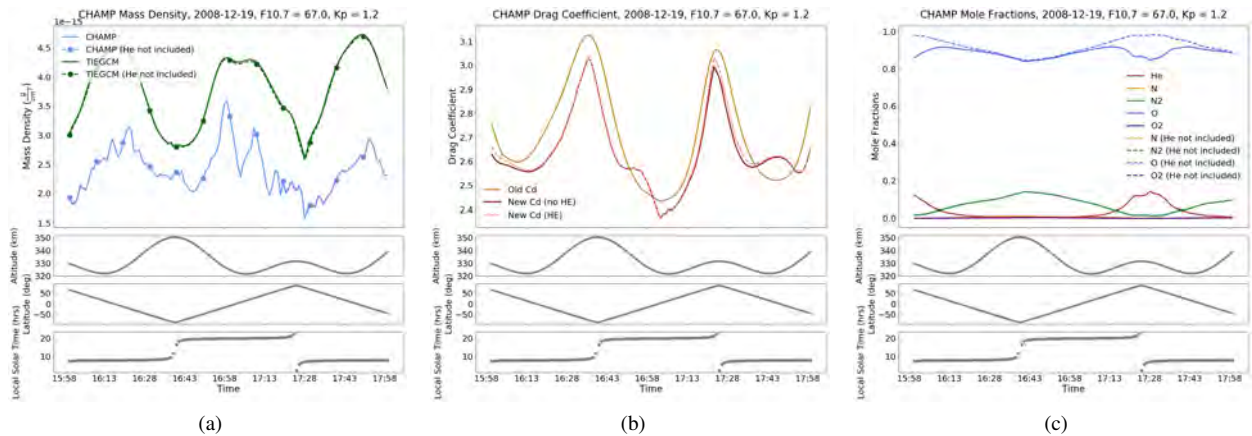


Figure 4: The same atmospheric quantities from Figure 3 along CHAMP's orbit are presented here, but in this case the comparisons are shown for a quiet solar minimum two-hour time period in December of 2008.

Figure 4 presents the same comparison between TIEGCM with and without helium and CHAMP measurements for a two-hour time period in extremely quiet solar minimum conditions in December of 2008. For this time period the helium concentration, when it is included in the TIEGCM model, starts to increase just slightly around the winter pole which supports a trade-off between helium and oxygen. Helium is still not reaching high concentrations at these low altitudes, so there is not a significant difference observed in TIEGCM or CHAMP densities/drag coefficients with and without helium. Thus essentially, at CHAMP altitudes, helium does not significantly impact satellite drag.

### 3.2. GRACE Altitudes

Helium concentration is higher at GRACE altitudes and behaves differently according to geomagnetic activity conditions. At higher altitudes, minor species like helium increase in concentration. The atmosphere additionally becomes more contracted during solar minimum conditions which serves to further increase the concentrations of



lighter species. To examine the effect of including helium in TIEGCM on TIEGCM's ability to predict the atmospheric conditions seen by GRACE, we can look at two representative examples corresponding to geomagnetically active solar maximum conditions and geomagnetically quiet solar minimum conditions in Figures 5 and 6. Figure 5 shows TIEGCM performance, both with and without helium, compared to GRACE's measurements for a two-hour time period in the geomagnetically active solar maximum conditions of October of 2003. Again, no quantitatively significant difference is observed between TIEGCM densities with and without helium in terms of how well TIEGCM can predict the GRACE-derived densities as revealed by a mean percent difference for TIEGCM densities with and without helium averaged over the full week of simulations for October of 2003 of 0.87%. Similarly, the newly computed drag coefficients for GRACE with and without helium do not present with significant differences. When helium is included in TIEGCM, its fractional concentration again increases by  $\sim 12\%$  at the northern pole.

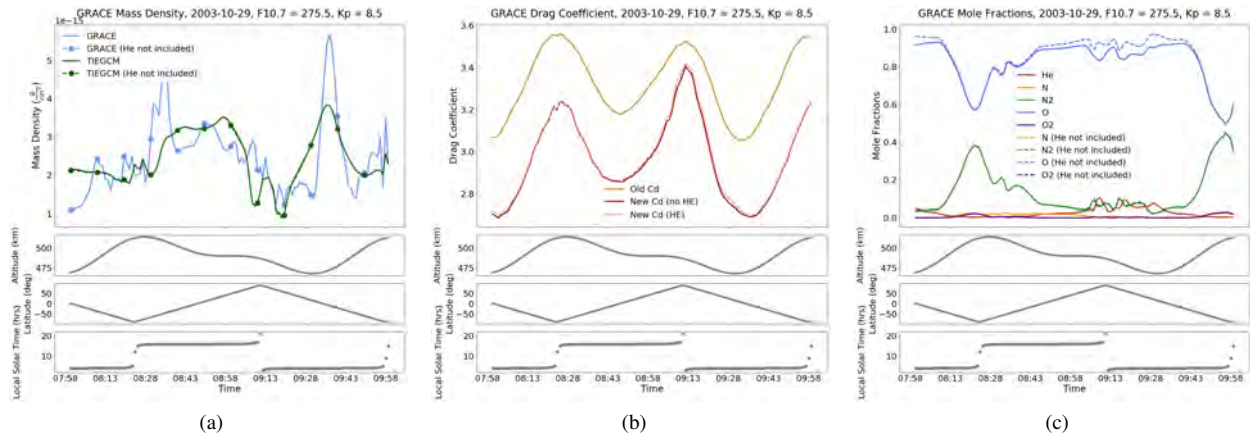


Figure 5: The same atmospheric quantities from Figures 3 and 4 are presented here, but in this case the comparisons are shown along GRACE's orbit for an active solar maximum two-hour time period in October of 2003.

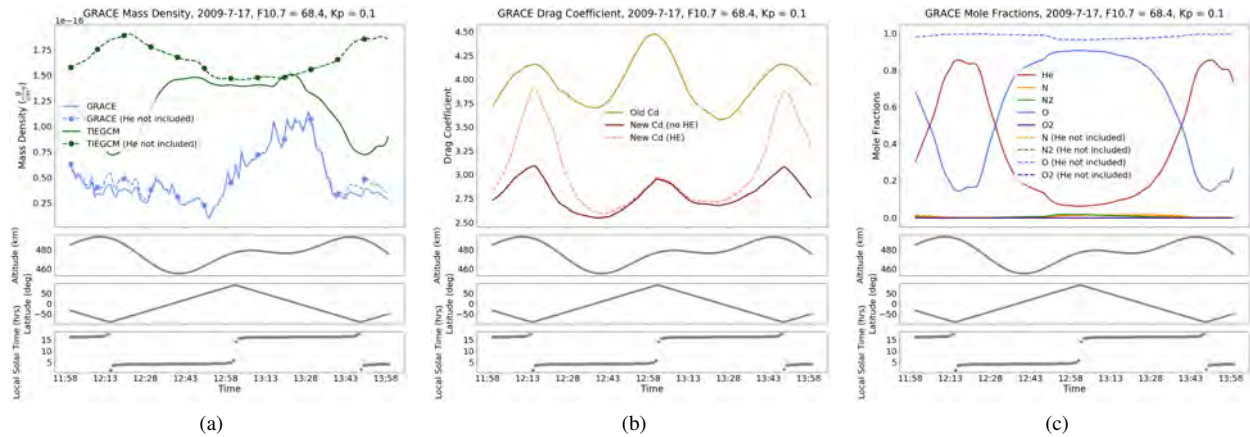


Figure 6: The same atmospheric quantities from Figure 5 along GRACE's orbit are presented here, but in this case the comparisons are shown for a quiet solar minimum two-hour time period in July of 2009.

Figure 6 shows a comparison between TIEGCM atmospheric quantities modeled with and without helium along GRACE's orbit for a quiet solar minimum time period during July of 2009. For this extremely geomagnetically quiet time period, large deviations (up to  $\sim 60\%$ ) between TIEGCM predicted density without helium and TIEGCM predicted density with helium are revealed. Additionally, small changes (up to  $\sim 25\%$ ) in the GRACE-derived density without helium and GRACE-derived density with helium become apparent. These deviations are maximized right at the winter pole, which in this case is in the southern hemisphere. In this case, TIEGCM with helium predicts

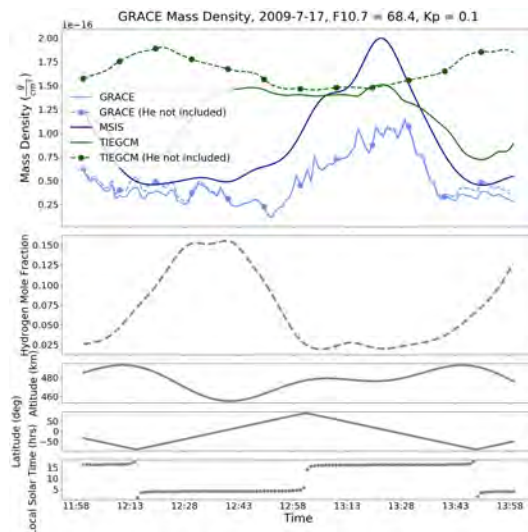


Figure 7: The same atmospheric quantities from Figure 6a along GRACE’s orbit for a quiet solar minimum two-hour time period in July of 2009 are presented here, but in this case the MSIS empirically modeled density is also included for comparison purposes. A subpanel including hydrogen concentration modeled by MSIS is added below the main panel.

a density that is closer to the density inferred from GRACE, especially at the winter pole. Helium inclusion also has an impact on the drag coefficients for GRACE during quiet solar minimum at the winter poles. The newly computed drag coefficients increase as helium increases because helium is much lighter than oxygen, and lighter species have higher velocities when interacting with the satellite. It is also interesting to note that the drag coefficients computed based on a TIEGCM atmosphere without helium are significantly lower than the previously published drag coefficients computed by Mehta et al. (2017) based on an MSIS atmosphere. This can be explained due to the fact that MSIS includes estimates of both atmospheric helium and hydrogen in its outputs which would serve to increase the drag coefficient due to their lighter relative molecular weights. To confirm the larger concentration of helium along GRACE’s orbit during solar minimum, Figure 6c shows a significant increase in helium concentration at the winter poles when helium is included in TIEGCM. Here helium becomes the dominant constituent, and the oxygen concentration largely decreases. When helium is left out of TIEGCM, TIEGCM predicts that oxygen dominates across all latitudes.

Helium inclusion in TIEGCM additionally appears to cause significant differences between TIEGCM atmospheres and MSIS atmospheres along GRACE’s orbit for quiet solar minimum conditions. For the same two-hour quiet solar minimum time period during July of 2009, Figure 7 shows TIEGCM and GRACE-inferred densities with and without helium overlaid with the MSIS empirically modeled density for comparison. An additional subpanel is included in Figure 7 which shows the hydrogen content along GRACE’s orbit as predicted by MSIS. Both TIEGCM densities with and without helium deviate largely from the MSIS density (with percent differences up to ~66% and ~73%, respectively). Overall, it appears that the TIEGCM density with helium better matches the MSIS density, however a large discrepancy between the TIEGCM with helium and MSIS densities occurs right at the time when hydrogen is modeled by MSIS to make up 15% of the atmosphere. TIEGCM does not include hydrogen in its computations, and this could be an explanation for why TIEGCM with helium overestimates the density here and could advocate for TIEGCM needing to include hydrogen, as it did helium, to be able to better predict these very quiet, contracted solar minimum conditions.

#### 4. Conclusions

Helium does not significantly improve TIEGCM estimates at CHAMP altitudes for any latitude or level of geomagnetic conditions. TIEGCM results with helium on average compare essentially the same to CHAMP inferred

densities and MSIS empirically modeled densities as TIEGCM results without helium. This is shown quantitatively in Table 2.

Table 2: Effect of helium at CHAMP altitudes

	Quantity	Average ( $g/cm^3$ )	% Difference
Solar Maximum	TIEGCM density with helium	4.64e-15	
	CHAMP density with helium	3.83e-15	21.37
	TIEGCM density without helium	4.62e-15	
	CHAMP density without helium	3.84e-15	20.57
Solar Minimum	TIEGCM density with helium	4.64e-15	
	MSIS density	4.68e-15	0.82
	TIEGCM density without helium	4.62e-15	
	MSIS density	4.68e-15	1.24
Solar Minimum	TIEGCM density with helium	3.83e-15	
	CHAMP density with helium	2.10e-15	82.69
	TIEGCM density without helium	3.80e-15	
	CHAMP density without helium	2.10e-15	81.02
Solar Minimum	TIEGCM density with helium	3.83e-15	
	MSIS density	3.18e-15	20.50
	TIEGCM density without helium	3.80e-15	
	MSIS density	3.18e-15	19.71

Helium makes a larger impact during solar minimum for GRACE altitudes. Most notably, helium improves TIEGCM predictions for density as compared to GRACE-inferred density and MSIS modeled density at winter polar latitudes during solar minimum conditions. Additionally, on average the drag coefficients computed for GRACE based on TIEGCM atmospheres with and without helium differed by nearly 7%. These results are quantified in Table 3. We see similar improvements attributed to helium such that TIEGCM densities better match GRACE densities for moderate Kp times, however the comparison to MSIS density during moderate Kp times is not as straightforward. TIEGCM density with helium appears to compare much worse to MSIS density than TIEGCM density without helium. However since TIEGCM density with helium compares better to the GRACE-derived density and worse to the MSIS density than TIEGCM density without helium, this could suggest that MSIS is for some reason not sufficiently equipped to accurately model solar minimum atmospheres at times of moderate geomagnetic activity.

Thus, helium makes a significant impact on TIEGCM satellite drag estimates at GRACE altitudes (~500 km) around the winter poles and during quiet and contracted solar minimum conditions. It is important to emphasize the role of the contracted atmosphere because this is what allows helium to dip down to these lower altitudes. For other conditions analyzed in this study, including solar maximum time periods, lower altitudes along CHAMP's orbit, and higher levels of geomagnetic activity, TIEGCM with helium did not improve atmospheric drag estimates. Lastly, during this past solar minimum it is likely that the atmosphere was contracted enough that there actually existed a significant percentage of hydrogen at GRACE altitudes as indicated by MSIS hydrogen estimates. Perhaps TIEGCM could improve its solar minimum atmospheric drag predictions if it were to include hydrogen as it did helium.

## Acknowledgments

This material is based upon work supported in part by the Center for Space and Earth Sciences at Los Alamos as well as the National Science Foundation Graduate Research Fellowship under Grant No. 1650115. We would also like to acknowledge high-performance computing support from Cheyenne (doi:10.5065/D6RX99HX) provided by NCAR's Computational and Information Systems Laboratory, sponsored by the National Science Foundation.

Table 3: Effect of helium at GRACE altitudes during solar minimum

	Quantity	Average ( $g/cm^3$ )	% Difference
Winter Polar Locations	TIEGCM density with helium GRACE density with helium	1.40e-16 9.36e-17	49.89
	TIEGCM density without helium GRACE density without helium	1.64e-16 1.01e-16	63.24
	$C_D$ with helium $C_D$ without helium	3.07 2.88	6.81
	TIEGCM density with helium MSIS density	1.4e-16 1.13e-16	23.71
	TIEGCM density without helium MSIS density	1.64e-16 1.13e-16	44.88
Moderate Kp Conditions	TIEGCM density with helium GRACE density with helium	1.51e-16 1.27e-16	18.81
	TIEGCM density without helium GRACE density without helium	1.69e-16 1.31e-16	29.01
	TIEGCM density with helium MSIS density	1.51e-16 1.71e-16	11.62
	TIEGCM density without helium MSIS density	1.69e-16 1.71e-16	1.36

## References

- Cageao, R., Kerr, R., 1984. Global distribution of helium in the upper atmosphere during solar minimum. *Planetary and space science* 32, 1523–1529.
- Keating, G., Prior, E., 1967. The winter helium bulge(diurnal atmospheric density bulge shifts observed by explorer, showing latitudinal-seasonal variation in helium concentration), in: COSPAR, Plenary Meeting, 10th, London, England, p. 1967.
- Liu, X., 2013. The effects of composition on thermosphere mass density response to geomagnetic activity .
- Liu, X., Thayer, J., Burns, A., Wang, W., Sutton, E., 2014a. Altitude variations in the thermosphere mass density response to geomagnetic activity during the recent solar minimum. *Journal of Geophysical Research: Space Physics* 119, 2160–2177.
- Liu, X., Wang, W., Thayer, J.P., Burns, A., Sutton, E., Solomon, S.C., Qian, L., Lucas, G., 2014b. The winter helium bulge revisited. *Geophysical Research Letters* 41, 6603–6609.
- Marcos, F., Bowman, B., Sheehan, R., 2006. Accuracy of earth’s thermospheric neutral density models, in: AIAA/AAS Astrodynamics Specialist Conference and Exhibit, p. 6167.
- Mehta, P.M., Walker, A.C., Sutton, E.K., Godinez, H.C., 2017. New density estimates derived using accelerometers on board the champ and grace satellites. *Space Weather* 15, 558–576.
- Picone, J., Hedin, A., Drob, D.P., Aikin, A., 2002. Nrlmsise-00 empirical model of the atmosphere: Statistical comparisons and scientific issues. *Journal of Geophysical Research: Space Physics* 107, SIA–15.
- Richmond, A., Ridley, E., Roble, R., 1992. A thermosphere/ionosphere general circulation model with coupled electrodynamics. *Geophysical Research Letters* 19, 601–604.
- Sutton, E.K., Nerem, R.S., Forbes, J.M., 2007. Density and winds in the thermosphere deduced from accelerometer data. *Journal of Spacecraft and Rockets* 44, 1210–1219.
- Sutton, E.K., Thayer, J.P., Wang, W., Solomon, S.C., Liu, X., Foster, B.T., 2015. A self-consistent model of helium in the thermosphere. *Journal of Geophysical Research: Space Physics* 120, 6884–6900.
- Thayer, J., Liu, X., Lei, J., Pilinski, M., Burns, A., 2012. The impact of helium on thermosphere mass density response to geomagnetic activity during the recent solar minimum. *Journal of Geophysical Research: Space Physics* 117.

# Quantifying Uncertainty in Space Weather Forecasting

Shibaji Chakraborty

*Virginia Tech., Blacksburg, VA 24061*

Steven Karl Morley

*Los Alamos National Laboratory, Los Alamos, NM 87545*

---

## Abstract

Space weather impacts various facets of our everyday life, from GPS navigation service accuracy to radiation dose on transpolar flights. Space weather effects at Earth are driven by a wide range of solar and solar wind phenomenologies. Geomagnetic storms, whose intensity are often described by a geomagnetic index ( $K_p$ ), are a space weather phenomenon that can affect both space and ground based electrical systems. Current operational forecasts of geomagnetic indices use empirically-derived coupling functions or computationally expensive physics models to forecast short-term  $K_p$ , and neural networks for 3–to–12 hour ahead prediction. None of these methods provide error or uncertainty estimation associated with their forecast. For higher values of  $K_p$ , the accuracy of current methods reduces. This work aims to provide a  $K_p$  forecast for 3–hour with uncertainty bounds associated with each prediction. We will explore both parametric and non-parametric techniques to provide a probabilistic  $K_p$  forecast and quantify the uncertainty. Key factors in obtaining a good prediction include appropriate choices of training data and model. We used selected solar wind parameters to predict  $K_p$ . Using transformed solar wind parameters, historical  $K_p$  values and different transfer functions can increase the accuracy of the models. Our candidate models mainly use dynamic training sets to produce forecasts. In accordance with this, we used variable training windows to find the best-fitted model, providing insights about the solar wind parameters and solar cycle and how they affect the coupling to the geospace environment.

*Keywords:* uncertainty quantification, space weather,  $K_p$ , probabilistic forecasting

---

## 1. Introduction

Many advanced electrical systems and equipment on the Earth such as navigation systems, communication systems, satellite systems, and power grid can be impacted by space weather (Ayala Solares et al., 2016). For this reason, it is desirable to predict the level of geomagnetic activity that results from solar wind driving. To describe the level of geomagnetic activity the  $K_p$  index was introduced by Bartels in 1949 (Bartels, 1949). A geomagnetic index describes the intensity of the magnetic disturbance for a certain period of time. There are two main classes of index available to describe the disturbances in the Earth’s geomagnetic field, range indices and mean indices.  $D_{st}$  is an example of the mean index, which is a good proxy for the strength of the ring current and obtained by averaging the low-latitude magnetometer measurements. On the other hand, we have  $A_p, K_p$  which are examples of range indices, which respond primarily to middle latitude geomagnetic activities and also a good proxy for magnetospheric convection. The  $K$  index is used to describe the geomagnetic disturbances at a single ground magnetometer observation for a 3–hour window. The  $K_p$  index is calculated by the weighted average of the  $K$  index of the 13 magnetometer stations around the Earth.  $K_p$  is a 3–hourly range index from starts from 0 (very quiet) to 9 (very disturbed) with 28 discrete values describe by  $[0, 0^+, 1^-, 1, 1^+, \dots, 9^-, 9]$  (Bartels, 1949). As  $K_p$  is used to quantify the geomagnetic disturbances in the upper atmosphere, hence it has been used to categorize the geomagnetic activity. NOAA Space Weather Prediction

---

*Email addresses:* shibaji7@vt.edu (Shibaji Chakraborty), smorley@lanl.gov (Steven Karl Morley)

Center (SWPC) classifies geomagnetic activity into six levels and the categorical division is shown in the Table-1. Also, note that the  $K_p$  index is widely used as an input to other magnetospheric models (Ji et al., 2013).

There are plenty of studies aiming to build coupled physics-based models to forecast  $K_p$  and understand the relationship between the  $K_p$  and solar wind. These physics-based models help us to boost our knowledge about the correlation between, for example, solar wind parameters and reconnection rate (Borovsky et al., 2008). However, the coupled physics-based models are able to provide a  $K_p$  forecast less than 1-hour ahead of time (which is the time taken by the solar wind to reach the Earth from  $L_1$  point)(Bala and Reiff, 2012). Along with this complex physics-based model, many data-driven studies (most of them use Neural Network; NN)(Wing et al., 2004; Costello, 1998; Boberg et al., 2000; Tan et al., 2017) also become very popular to extract relational dependencies between the solar wind and  $K_p$  during the last couple of decades. These data-driven methods do not provide physical insights in the solar wind as the physics-based models, but they are very good in capturing the complex and nonlinear trends (nonlinear physics) within the solar wind dataset and are able to forecast  $K_p$  for 3-to-12 hours ahead of time effectively. Hence, there are couple of options available to build a robust  $K_p$  forecast model. In this study, we will discuss a data-based  $K_p$  forecast model.

Storm Level	$K_p$ Range
$G_0$	$K_p < 5^-$
$G_1$	$5^- \leq K_p < 6^-$
$G_2$	$6^- \leq K_p < 7^-$
$G_3$	$7^- \leq K_p < 8^-$
$G_4$	$8^- \leq K_p < 9^-$
$G_5$	$K_p > 9^-$

Table 1: Table showing different categories of geomagnetic storm and associated  $K_p$ . The categorization is done based on intensity of the geomagnetic storm following the NOAA SWPC scales.

Since Costello proposed the first  $K_p$  prediction model based on a Neural Network (NN) (Costello, 1998), many subsequent forecast models (Wing et al., 2004; Boberg et al., 2000; Tan et al., 2017) exploited different solar parameters and implement different variants of NN to improve the forecast accuracy. Later, people also used historical  $K_p$  values including solar wind parameters to capture the state of the magnetosphere (Tan et al., 2017). Over the time as our understanding of the reconnection, physics improved modeler have started introducing new parameters or combinations of the solar parameters to their models to increase the accuracy of the models and incorporate the physics.

In this work we use a nonparametric-Bayesian method to forecast  $K_p$  and the associated uncertainty, then exploit the uncertainty bounds in  $K_p$  to provide a probabilistic forecast. The paper is organized as follows: Section 2 explains the data analysis, Section 3 describes the different methodologies, compare the results, then Section 4 shows how we develop a probabilistic forecast and finally paper closes with discussion and conclusion.

## 2. Data Analysis & Preprocessing

Different solar wind and IMF parameters are used in different models (Luo et al., 2016). We started using 22 years of 1 minute resolution solar wind data from OMNI database (with all  $x, y, z$  components of velocity and IMF parameter). Clearly, 22 years of 1 minute resolution data is difficult to process and train any model. Also, 1 minute resolution data may carry redundant temporal information about the solar wind structures. Most of these parameters are correlated with each other and might carry redundant solar wind structure information. We did a cross-correlation study among all the parameters to reduce redundant information about the solar wind. It seems parameters (including  $x, y, z$  components) have redundant information (few of them are highly correlated with each other). To check the redundancy in the temporal dataset we did an auto-correlation study. Figure-1 shows autocorrelation functions for various solar wind parameters, for both solar minima and solar maxima. Autocorrelation function shows that 2 – 3 hour interval dataset is good enough to represent the variability in the solar wind data. The autocorrelation functions show that many of the solar wind parameters are highly autocorrelated and thus points with small temporal separations are not independent and carry redundant information. For this reason we use to 3-hour resolution datasets to train our

models.

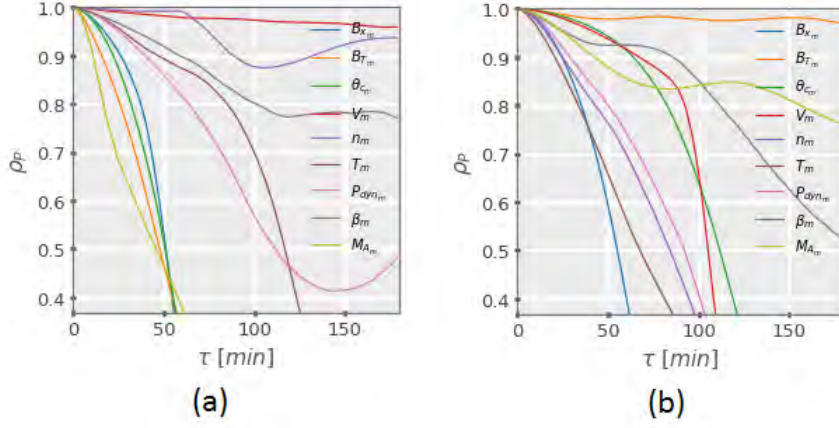


Figure 1: Auto-correlation functions of different solar-wind parameters during: (a) solar minima, and (b) solar maxima.

Features	Symbol	Units	Transformation
Anti-sun ward component of IMF	$B_{x_m}$	$nT$	<i>BoxCox</i>
Transverse component of IMF	$B_{T_m} = \sqrt{B_{y_m}^2 + B_{z_m}^2}$	$nT$	<i>BoxCox</i>
IMF clock angle	$\theta_c = \arctan \frac{B_{y_m}}{B_{z_m}}$	<i>radian</i>	<i>BoxCox</i>
Bulk Velocity	$v = \sqrt{v_{x_m}^2 + v_{y_m}^2 + v_{z_m}^2}$	$km\ s^{-1}$	<i>BoxCox</i>
Number Density	$n_m$	$m^{-3}$	<i>BoxCox</i>
Temperature	$T_m$	$K$	<i>BoxCox</i>
Dynamic Pressure	$P_{dyn_m}$	$Nm^{-2}$	<i>BoxCox</i>
Mach number	$M_{a_m}$	1	<i>BoxCox</i>
Plasma Beta	$\beta_m$	1	<i>Erf</i>
Historical $Kp$	$K_{P_m}(t_0 - 1)$	1	<i>BoxCox</i>

Table 2: Table showing input features of the model. Note that, the transformation is only needed to fit the data to Gaussian process model.  $BoxCox \rightarrow B(x) = sgn(x).log_e x$  and  $Erf \rightarrow erf(x) = sgn(x).\sqrt{2}erf^{-1}\left(1 - 2e^{-\frac{|x|a}{b}}\right)$

These solar wind energy and magnetospheric coupling are known to be constrained by the solar wind parameters and the state of the magnetosphere (Dungey, 1961; Baker et al., 1981). Many prior studies show that plasma velocity, components of the interplanetary magnetic field and particle density are the major driving parameters of solar wind coupling (Borovsky et al., 1998; Baker et al., 1981). People suggested many theoretically and empirically derived “coupling functions” as a function of different solar wind parameter since the 1960s, and validate them by correlating coupling functions with geomagnetic indexes  $D_{st}$ ,  $K_p$  etc (Kan and Lee, 1979). Studies also show that transverse coupling functions with geomagnetic activities, than individual IMF components (Kan and Lee, 1979; Newell et al., 2007). Recent studies show that solar wind plasma can be categorized into 4 different kinds, having different characteristics and associate with different types space weather activities. These different kinds of plasma can be categorized using temperature and plasma constituents (Xu and Borovsky, 2014). Studies also show that plasmaspheric drainage plumes slow down the solar wind reconnection rate and local magnetic field strength ( $B$ ) and plasma mass densities

( $\rho$ ) on the bow shock and magneto-sheath controls the reconnection rate (Borovsky et al., 2008). Based on this prior knowledge we consider 9 transformed solar wind parameters, and historical  $K_p$  to as model features, listed in Table-2.

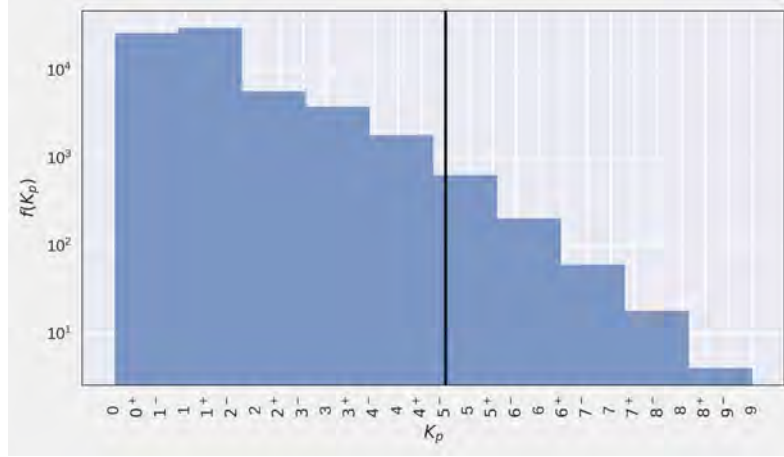


Figure 2: Distribution of  $K_p$ . 22 years 1995 – 2014 of data has been used in this plot.  $f(K_p)$  is the frequency (i.e. number of events) plotted on a logarithmic scale. Black vertical line is  $K_p = 5^-$ .

We converted the reported  $K_p$  values to decimal numbers using  $n \pm \frac{1}{3}$  following Tan et al. (2017). Now, this transformation of  $K_p$  from a quasi-logarithmic ranges to a decimal numbers and treating it as a continuous will introduce some error in  $K_p$  prediction.

### 2.1. Data Imbalance

We have analyzed the distribution of  $K_p$  values as shown in Figure-2. Figure-2 shows the distribution (number of  $K_p$ ) of 22 years of  $K_p$  data. From the figure we can conclude that, most of the events are distributed between  $[0, 5^-)$  and a very small number of extreme events  $\geq 7$ . From the distribution, it is clear that the ratio of storm events versus nonstorms has a ratio of  $\approx \frac{1}{20}$ . Note that, this number goes down with an increase in  $K_p$  level, i.e. if we take the ratio of more extreme events ( $K_p \geq 8^+$ ) versus nonstorm events then number drops to  $\approx \frac{1}{200}$ . Hence storm versus non-storm ratio is very small and it becomes a data imbalance (Estabrooks et al., 2004) or anomaly detection problem.

## 3. Methodology

In this section, we will discuss the basic characteristics and detailed architecture of the proposed model. The proposed model as shown in Figure-3 has two layers, a deterministic classifier to separate storm from nonstorm conditions and two different regressors; the regressor selection depends on the outcome of the classification step. The classifier separates extreme ( $K_p \geq 5^-$ ) versus quiet events ( $K_p < 5^-$ ), and the regressors are used to provide a probabilistic  $K_p$  forecast (provides a distribution of  $K_p$  as a forecast instead of one value). Also, note that these regressors use dynamic training window for model training. We used this type of mixed architecture to handle the data imbalance issue as described in the previous section-2. We tested multinomial classification over binary classification to subdivide the storm conditions to more classes ( $> 2$ ) to get a better prediction, but an introduction of a new class (severe storm, storm, and nonstorm) reduces the number of samples and accuracy of the classifier significantly, hence we have used a binary classifier. Now the question is how to build a probabilistic regressor? Also what type of classifiers and regressors will be suitable for these types of dataset and forecasting model and how to implement them? We tested various families of deterministic algorithms to examine which work the best for this case.



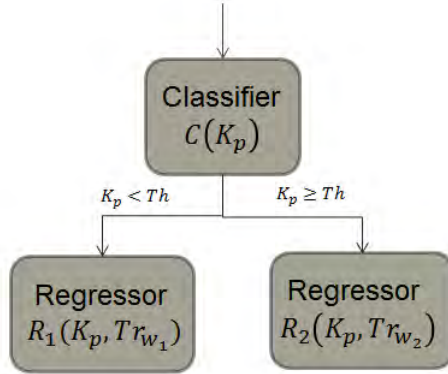


Figure 3: Proposed model architecture: Classifier is deterministic in nature, and regressors are probabilistic in nature. The threshold ( $Th$ ) for the classifier is  $K_p = 5^-$ .  $Tr_{w_1}$  &  $Tr_{w_2}$  are the variable training window for two regressors.

### 3.1. Binary Classifier

We use a deterministic binary classifier to separate active versus quiet time events. We tested different classes of deterministic classifiers. We have used 5-fold cross-validation with 22 years of data to train the classifier models. The receiver operating characteristic curves (ROC) for these they are shown in the Figure-4. The ROC curve is the true positive rate (TPR) against the false positive rate (FPR) at various threshold settings. Each panel in Figure-4 represents a family of deterministic binary classifier algorithm with more than one algorithm. The diagonal dashed lines represents no skill line and left top corner represents highest skill. Area enclosed by the individual ROC curve also represents the skill of the model. Among all these different categories Ensembles (Random Forest) and Linear Discriminant Analysis (LDA) performs the best, and we therefore adopted the random forest as our classifier.

### 3.2. Regression

The basic feature of the regressor has to be probabilistic. However, we also used a few deterministic algorithms to test out the performance of the model. Also, this part used dynamic training windows to train the model. The performance comparisons of different algorithms, as quantified by the root mean square error ( $RMS E$ ) of the output. The different lengths of training window is listed in Table-3 and the  $RMS E$  values were computed based on 22 years of test data.

<b>Algorithm (Deterministic)</b>	$Tr_w = 27 \text{ days}$	$Tr_w = 54 \text{ days}$	$Tr_w = 81 \text{ days}$
Linear Regression	0.78	0.78	0.78
Elastic Net	0.85	0.84	0.85
Bayesian Ridge	0.78	0.78	0.78
Decision Tree	0.91	0.88	0.86
Extra Tree	0.91	0.88	0.86
Bagging	0.87	0.87	0.87
Ada Boosts	0.90	0.87	0.86
Random Forests	0.81	0.79	0.79
K-Nearest Neighbor	1.18	1.05	0.99
Long Short Term Memory	0.94	–	–

Table 3: List showing performance comparisons of different regression algorithms (deterministic) with different training window. “–” denotes the configuration has not been tested.

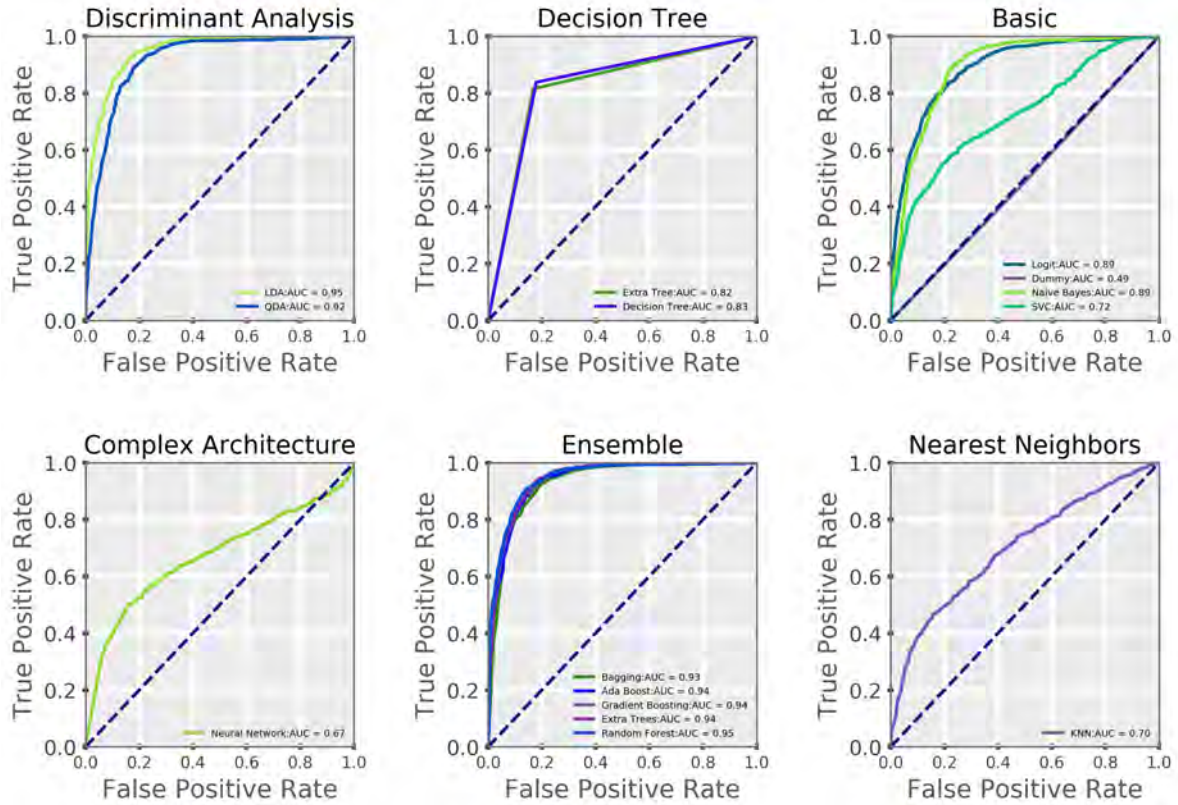


Figure 4: Receiver operating characteristic (ROC) curves for different families of classifiers. The diagonal dashed line inside each panel is no skill line and other lines are skill lines for individual algorithm. AUC is the area under the curve.

### 3.2.1. Dynamic Training Window

Instead of using a part of the dataset as training and a set for testing, we used a dynamic training window. For each time step the model is trained using the interval of preceding data and the prediction is then tested using subsequent intervals. Test shows that different phases of the solar cycle need different training windows to minimize the training error. Figure-5 shows one example of mean square error (MSE) with variation with training window (in days) during solar minima during 1995. Figure-5 clearly shows  $\approx 25-27$  days training window is sufficient to minimize the RMSE. Usually, for declining phase of solar minima, it takes  $\approx 27$  days to train the model while it takes  $\approx 7-14$  days training window during solar maxima period.

### 3.2.2. Non-parametric Bayesian Method

One of the main characteristics of the regressors is that they provide the probabilistic prediction, i.e. they predict a distribution of output parameter instead of only one value. Non-parametric models are a way of getting a very flexible model. Many can be derived by starting with a finite parametric model and taking the limit as an infinite number of parameters. Non-parametric models can automatically infer an adequate model size/complexity from the data. Bayesian methods assume that all the parameters which have been used to describe the dataset are coming from a distribution, hence the predicted output from a Bayesian model also follows a distribution. Bayesian method assumes some prior knowledge about the distribution which is updated based on the observations, given by the equation-1. Note that,  $\pi(\theta|X)$  is the conditional posterior distribution (which conditioned upon the data  $X$ , hence change in  $X$  will alter  $\pi(\theta|X)$ ),  $\pi(\theta)$  is the prior knowledge of the parameter  $\theta$  and  $L(\theta|X)$  is the likelihood function of  $\theta$ . Bayesian methods are most powerful when sufficient amount of observation ( $X$ ) is there to describe the reality or prior assumption is close approximation of the reality. The Gaussian process, and Dirichlet process are examples of non-parametric Bayesian

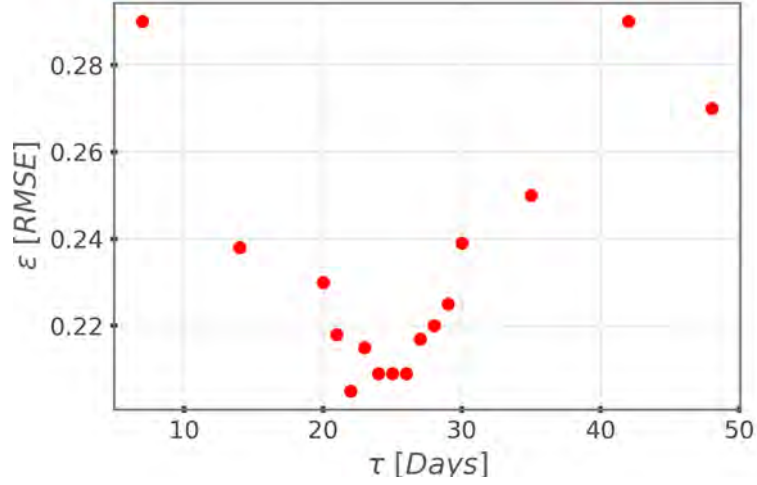


Figure 5: Variation of root mean square error (RMSE,  $\epsilon$ ) in with the length of the training window ( $\tau$ ) in days. Each point of this curve is generated using average RMSE of two months of data.

methods (Pozzo et al., 2018).

$$\pi(\theta|X) = \frac{L(\theta|X).\pi(\theta)}{\int_{\theta} L(\theta|X).\pi(\theta)d\theta} \quad (1)$$

### 3.2.3. Gaussian Process Regression (GPR)

Gaussian process regression (GPR) is a non-parametric Bayesian method, which assumes that the output parameter is a distribution, and it is Gaussian in nature. The underlying architecture of GPR is described in Gaussian Process. Gaussian Process is a stochastic process which assumes that all the data points are coming from a multivariate normal distribution. The distribution of a Gaussian process is the joint distribution of all random variables and it is a distribution over functions with a continuous domain. Equation-2 describes the mathematical backbone of the Gaussian Process:

$$\begin{bmatrix} f \\ f_* \end{bmatrix} \leftarrow N(M, \Sigma) = N\left(\begin{bmatrix} m_X \\ m_{X_*} \end{bmatrix}, \begin{bmatrix} \kappa_{XX} & \kappa_{XX_*} \\ \kappa_{XX_*} & \kappa_{X_*X_*} \end{bmatrix}\right) \quad (2)$$

where, \* denotes the unobserved or predicted values. In the above equation-2 “ $f$ ” is the output (in this case  $K_P$ ),  $X$  is a vector of regressors (here 10 features listed in Table-2),  $M$  is the mean vector described by  $\begin{bmatrix} m_X \\ m_{X_*} \end{bmatrix}$  and  $\Sigma$  is the correlation matrix described by  $\begin{bmatrix} \kappa_{XX} & \kappa_{XX_*} \\ \kappa_{XX_*} & \kappa_{X_*X_*} \end{bmatrix}$  and  $\kappa$  is the kernel function. Kernels are co-variance functions, define the correlation between two different points ( $x$  and  $x'$ ). Different co-variance/kernel functions have different behaviour. Based on problem description and dataset we adopt kernel. Some sample co-variance/kernel functions are squared error kernel, rational quadrature kernel, periodic kernel described by equations-3 to 5 respectively. Based on our analysis rational quadratic kernel  $\kappa_{RQ}$  performs the best on these OMNI datasets.

$$\kappa_{SE}(x, x') = \sigma^2 e^{-\frac{1}{2} \frac{(x-x')^2}{2\lambda^2}} \quad (3)$$

$$\kappa_{RQ}(x, x') = \sigma^2 \left( 1 + \frac{(x-x')^2}{2\alpha\lambda^2} \right)^{-\alpha} \quad (4)$$

$$\kappa_{PER}(x, x') = \sigma^2 e^{-\frac{2\sin^2 \pi |x-x'|/p}{\lambda^2}} \quad (5)$$

We used this algorithm for  $K_p$  prediction and the outputs are shown in the Figures 6 and 7. Figures 6 and 7 shows solar minima during 1995 and solar maxima during 2004 respectively. Each figure is showing mean prediction (blue dots), 50% and 95% confidence intervals (dark and light blue) and true observations (red dots) of  $K_p$  for 2 month window (July and August). Figure-6 shows most of the observations ( $\geq 90\%$ ) lie within the 95% predicted confidence interval. This shows, GPR is a good approach to forecast  $K_p$  with uncertainty. However, a meticulous examination of Figures 6 and 7 show that GPR is unable to capture the transient physics in the solar wind and variability within  $K_p$ . Not only model is unable to capture storm time high  $K_p$  values, but it also unable to capture the variability of  $K_p$  during the quiet time (there is very small variability in mean predicted  $K_p$ ). This leads to our next algorithm Long Short Term Memory (LSTM) with Gaussian Process Regression to increase the accuracy of the model. Long Short Term Memory networks typically known as LSTM are a special kind of Recurrent Neural Networks which are capable of learning long-term temporal dependencies. Capturing the information for long periods of time is the implicit behavior of an LSTM. It has a memory that is used to capture the state of the process and based on the requirements user can update the memory. Hence, LSTMs are well-suited for making predictions based on time series data.

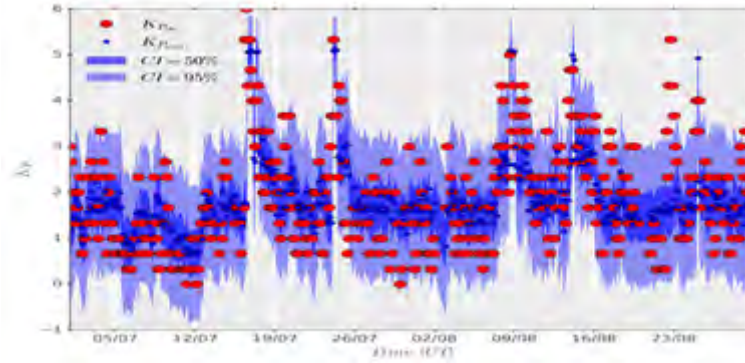


Figure 6: 3-hour forecast of  $K_p$  using Gaussian Process Regression (GPR) for a solar minimum period (1<sup>st</sup> July – 31<sup>st</sup> August, 1995). Blue dots are mean prediction and red dots shows observed  $K_p$ . Central dark blue shaded region shows 50% confidence interval and light shaded region shows 95% confidence interval.

### 3.2.4. Deep GPR (Long Short Term Memory + Gaussian Process Regression)

Probabilistic modeling with neural network architectures constitutes a well-studied area of machine learning (Hochreiter and Schmidhuber, 1997). The recent advances in the domain of deep (CireÅan et al., 2012) learning have brought this kind of models again in popularity. A deep neural network has multiple layers between input and output layers. Empirically, deep models seem to have structural advantages that can improve the quality of learning in complicated data sets associated with the abstract information. Deep GPR are a deep belief network based on Gaussian process mappings (Al-Shedivat et al., 2016). Deep architecture helps to capture the nonlinear trends in data to provide better accuracy. Figure-8 shows the output of deep GPR algorithm. This figure has the similar format to the the previous figures - 6 & 7. Clearly, we can see an improvement in prediction in  $K_p$  and is able to capture the variability during quiet time and geomagnetic active conditions. However, the confidence interval of the predicted  $K_p$  is smaller than the previous model which leads more than 10% of the observations lies outside 95% confidence interval. The probabilistic prediction is therefore is poorly calibrated. Additional technologies could be applied to the

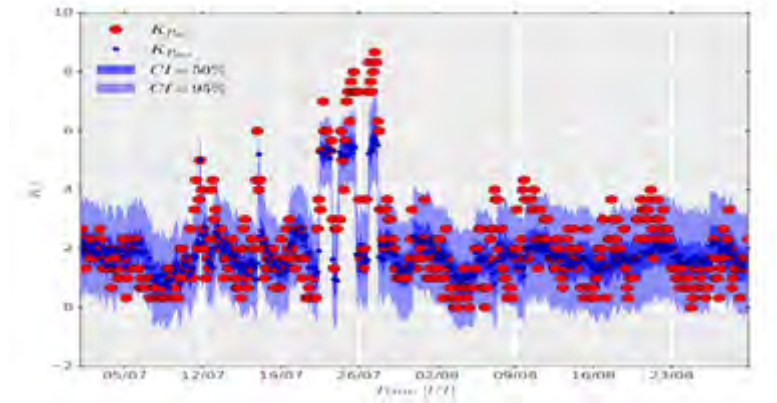


Figure 7: 3-hour forecast of  $K_p$  using Gaussian Process Regression (GPR) for a solar maximum period (1<sup>st</sup> July – 31<sup>st</sup> August, 2004). This figure has exactly similar format to the previous Figure-6.

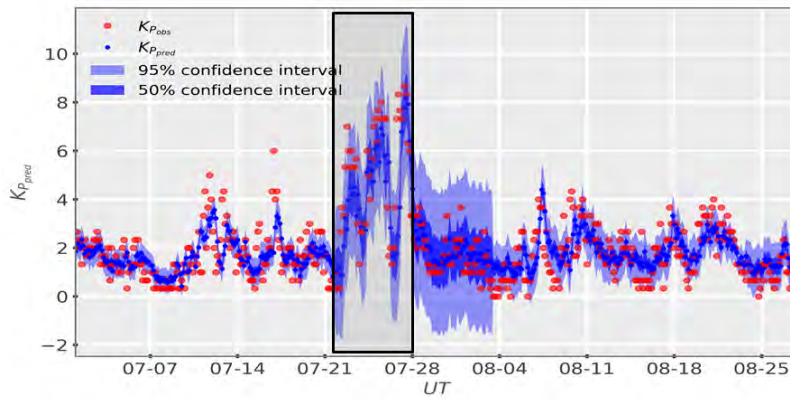


Figure 8: 3-hour forecast of  $K_p$  using LSTM + Gaussian Process Regression (GPR) for a solar maximum period (1<sup>st</sup> July – 31<sup>st</sup> August, 2004; same duration as Figure-7). This figure has exactly similar format to the previous Figure-6. The boxed region shows the increase in accuracy and ability to capture overall variability by introducing deep GP (LSTM + GP) algorithm.

calibrate forecast but this has not been done yet. Table-3.2.4 shows a quantitative comparison of RMSE between this algorithm (deep GPR) with simple GPR.

Algorithm (Probabilistic)	$Tr_w = 27 \text{ days}$	$Tr_w = 54 \text{ days}$	$Tr_w = 81 \text{ days}$
Gaussian Process Regression	1.04	–	–
LSTM + GPR	0.91	–	–

Table 4: List showing RMSE(performance) comparisons of different regression algorithms (probabilistic) with different training window. “–” denotes the configuration has not been tested.

### 3.3. Probabilistic Storm Forecast

This section describes how to exploit the uncertainty in predicted  $K_p$  (as described in previous section) to provide probabilistic storm forecast as shown in Figure-9. Figure-9a is a zoomed in version of Figure-8, which is one week (22<sup>nd</sup> July – 28<sup>th</sup> July, 2004) of 3-hour ahead of  $K_p$  prediction using deep GPR (LSTM with GPR) algorithm and also provide chance (probability) of storm associated with each predicted  $K_p$  (mean  $K_p$  values are shown in Figure-9a top

panel, color coded by probability of storm). Storms having probability greater than 30% are reported in the figure, while the color coded  $K_P$  show individual storm prediction following coloring scheme:  $Pr(e \geq G_1) < 30\%$  →green;  $30\% \leq Pr(e \geq G_1) \leq 60\%$  →orange;  $Pr(e \geq G_1) > 60\%$  →red. Figure-9b describes only one forecasted event denoted by vertical black line in Figure-9a. Vertical red and dotted black lines referenced to observed  $K_P$  and  $K_P = 5^-$ . The shaded area bounded by the predicted  $K_P$  distribution and  $K_P = 5^-$  line total chance (cumulative probability) exceeding a threshold value (in this case it is  $K_P = 5^-$ ), which is the probability of occurring a geomagnetic storm. Figure gave us a close look at the predicted  $K_P$ , which shows deep GPR provides reliable storm forecast. However, model is unable to capture the sharp transition of  $K_P$  later in this week, there is a delay associated with the prediction. We can use similar method to estimate the chance of exceeding  $K_P$  any threshold values to predict the chance of different levels of geomagnetic storm (as described in Table-1).

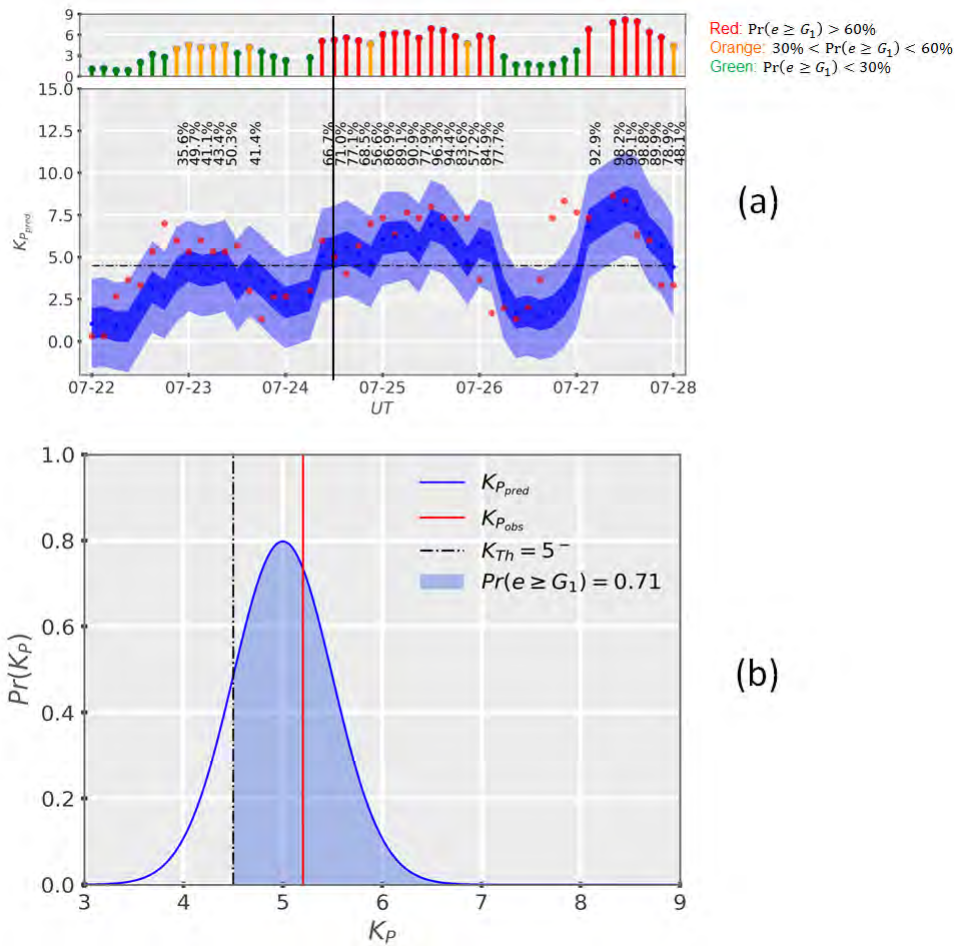


Figure 9: 3-hour forecast of geomagnetic storm &  $K_P$  using Deep Gaussian Process Regression (LSTM with GPR) for a solar maxima period (22<sup>nd</sup> July – 28<sup>th</sup> July, 2004): (a) predicted  $K_P$  distribution (same format as Figure-6) with probability shown in traffic light colors, (b) illustration of the method to extract probability of storm occurrence for one prediction marked by vertical black line in panel (a). Black dashed lines in both panels represent the threshold  $K_P = 5^-$ , red line in panel (b) is observed  $K_P$ .

## 4. Discussions

In this paper, we propose a dynamic model with two-layered mixed architecture to provide a probabilistic geomagnetic storm forecast. We compare different families of algorithms with proposed two-layered architecture with deep GPR. Most of the previous studies used physical models or neural network or NARMAX (nonlinear autoregressive moving average model with exogenous inputs) models to forecast geomagnetic storms, which are still state of the art. Recent studies have shown that LSTM is a good algorithm to capture temporal variations and transients in the solar wind data (Tan et al., 2017), which is also consistent in our method. The two-layered architecture is used to separate “storm” and “nonstorm” conditions which increase the accuracy of the forecasted  $K_p$  by treating it as a data imbalance problem. However, the errors in classifier (misclassification error) might increase the individual  $K_p$  prediction error, which raises the question of model credibility during storm time prediction. Also this can introduce a sharp transition in model behaviour in the boundaries. The ensemble random forest classifiers work best, but there is plenty of room to improve. Future studies will address the problems with the classifier. While working with the second layer (regression) of the proposed architecture we faced different challenges. We used the LSTM neural network with GPR to reduce the prediction errors and to get the uncertainty bound. In one of the optimization steps GPR inverts the covariance matrix, which is a computationally expensive task and explode exponentially with the training dataset. However, a neural network requires a large number of data sets to effectively train. To overcome this caveat we used a dynamic model with relatively shorter training window (the dataset is smaller as compared to other NN). This also helps us to infer physics about the solar wind parameter and some magnetospheric coupling.

In data analysis and preprocessing, we faced a few challenges, some of them are critical. Some of the minor problems is converting  $K_p$  from a quasi-logarithmic range values to a decimal continuous values using  $n \pm \frac{1}{3}$  this formula, which introduces errors in the system. Missing data was one of the critical problems as we are using LSTM. Also determining the length of the LSTM vector to capture sufficient temporal variation was challenging. We started using 1m interval data (we had to resample  $K_p$  to 1m), but data vector was too large to handle and there is high auto-correlation among the as shown in Figure-1. Hence we started using 3-hour mean values of the solar wind data. However, in Figure-9a we can clearly see the model is unable to capture the transients that drive rapid changes in magnetic activity and it responds much later ( $\approx 9$ -hours). Then we analyzed the correlation between solar wind parameters to reduce the number of an optimal number of parameters. We found that the 10 features described in Table-2 are good enough to build a storm forecast model. Although  $M_{a_m}$  and  $\beta_m$  shows large correlation, we used both of them into the model to capture reconnection physics. Future studies will try to address these problems and use higher resolution solar wind data to better capture the temporal variation. Future study also aim to provide the model with more information about what likely to happen with a horizon of more than 1-hour. One method would be to introduce more solar data, such as X-ray flux or magnetograms to capture the likelihood of solar transients.

To reduce the time complexity and increase model accuracy we used a dynamic model with different training windows. Study shows that (as shown in Figure-5) dynamic model takes almost  $\approx 27$  days of historical data to optimally train the data during declining phase of solar cycle, while it takes only a few days or a couple of weeks ( $\approx 7 - 14$  days) of data to minimize the MSE of the predicted  $K_p$ . This shows solar minima dominated by slow but consistent solar wind which repeats each 27 days while during solar maxima solar wind consists with turbulent structures which last for only for few days. There is plenty of opportunities to improve on this model, a few of them are discussed in this study and the rest of them will be targeted in the future studies.

## 5. Conclusions & Future Work

The main purpose of this study has been to build a probabilistic storm forecast model by exploiting the uncertainty in the forecasted  $K_p$ . Our secondary objective was to quantify the uncertainty in the  $K_p$  forecast. Results show that deep GPR (Gaussian Processes with LSTM) is a cutting-edge tool for probabilistic space weather forecast. But one bottleneck of introducing LSTM before the Gaussian process is reduction in the confidence interval of the predicted  $K_p$ , hence more than 10% observed  $K_p$  lies outside 95% confidence interval. Testing shows dynamic model takes 27 days to training window to provide an optimal forecast during declining phase & solar minima and 7 – 14 days window for solar maxima. This provides insights about the solar cycle and sun activity, which shows a slow and steady

long lasting solar wind during solar minima and more turbulent transients (short burst of intense energy) during solar maxima. Study shows solar wind data alone is not adequate to capture all the transient physics in solar activity. Future work will examine how the introduction of GOES X-ray & other datasets able to capture more solar transients.

## Acknowledgement

We thank the ISR-1, Los Alamos National Lab for organizing and supporting for Space Weather Summer School. We wish to acknowledge the use of the OMNI solar wind data, available at <https://omniweb.gsfc.nasa.gov/ow.html>. The  $K_p$  index was accessed through the GFZ-Potsdam website <https://www.gfz-potsdam.de/en/kp-index/>. The majority of analysis and visualization was completed with the help of free, open-source software tools such as matplotlib (Hunter, 2007), IPython (Pérez and Granger, 2007), pandas (McKinney, 2010), Spacepy (Morley et al., 2011), and others (e.g., Millman and Aivazis (2011)).

## References

- Al-Shedivat, M., Wilson, A.G., Saatchi, Y., Hu, Z., Xing, E.P., 2016. Learning scalable deep kernels with recurrent structure. arXiv preprint arXiv:1610.08936.
- Ayala Solares, J.R., Wei, H.L., Boynton, R.J., Walker, S.N., Billings, S.A., 2016. Modeling and prediction of global magnetic disturbance in near-Earth space: A case study for  $K_p$  index using NARX models. *Space Weather* 14, 899–916.
- Baker, D.N., Hones, E.W., Payne, J.B., Feldman, W.C., 1981. A high time resolution study of interplanetary parameter correlations with  $A_E$ . *Geophysical Research Letters* 8, 179–182.
- Bala, R., Reiff, P., 2012. Improvements in short-term forecasting of geomagnetic activity. *Space Weather* 10.
- Bartels, J.R., 1949. The standardized index,  $K_s$  and the planetary index,  $K_p$ . *IATME* 97.
- Boberg, F., Wintoft, P., Lundstedt, H., 2000. Real time  $K_p$  predictions from solar wind data using neural networks. *Physics and Chemistry of the Earth Part C: Solar Terrestrial and Planetary Science* 25, 275 – 280.
- Borovsky, J.E., Hesse, M., Birn, J., Kuznetsova, M.M., 2008. What determines the reconnection rate at the dayside magnetosphere? *Journal of Geophysical Research: Space Physics* 113.
- Borovsky, J.E., Thomsen, M.F., Elphic, R.C., Cayton, T.E., McComas, D.J., 1998. The transport of plasma sheet material from the distant tail to geosynchronous orbit. *Journal of Geophysical Research: Space Physics* 103, 20297–20331.
- CireÅan, D., Meier, U., Masci, J., Schmidhuber, J., 2012. Multi-column deep neural network for traffic sign classification. *Neural Networks* 32, 333 – 338. Selected Papers from IJCNN 2011.
- Costello, K.A., 1998. Moving the rice msfm into a real-time forecast mode using solar wind driven forecast modules. Ph.D. Dissertation, Rice University.
- Dungey, J.W., 1961. Interplanetary magnetic field and the auroral zones. *Phys. Rev. Lett.* 6, 47–48.
- Estabrooks, A., Jo, T., Japkowicz, N., 2004. A multiple resampling method for learning from imbalanced data sets. *Computational Intelligence* 20, 18–36.
- Hochreiter, S., Schmidhuber, J., 1997. Long short-term memory. *Neural Computation* 9, 1735–1780.
- Hunter, J.D., 2007. Matplotlib: A 2D graphics environment. *Computing In Science & Engineering* 9, 90–95.
- Ji, E.Y., Moon, Y.J., Park, J., Lee, J.Y., Lee, D.H., 2013. Comparison of neural network and support vector machine methods for  $K_p$  forecasting. *Journal of Geophysical Research: Space Physics* 118, 5109–5117.
- Kan, J.R., Lee, L.C., 1979. Energy coupling function and solar wind-magnetosphere dynamo. *Geophysical Research Letters* 6, 577–580.
- Luo, B., Liu, S., Gong, J., 2016. Two empirical models for short-term forecast of  $K_p$ . *Space Weather* 15, 503–516.
- McKinney, W., 2010. Data Structures for Statistical Computing in Python, in: van der Walt, S., Millman, J. (Eds.), *Proceedings of the 9th Python in Science Conference*, pp. 51 – 56.
- Millman, K.J., Aivazis, M., 2011. Python for Scientists and Engineers. *Computing in Science & Engineering* 13, 9–12.
- Morley, S.K., Koller, J., Welling, D.T., Larsen, B.A., Henderson, M.G., Niehof, J.T., 2011. Spacepy - a python-based library of tools for the space sciences, in: *Proceedings of the 9th Python in science conference (SciPy 2010)*, Austin, TX.
- Newell, P.T., Sotirelis, T., Liou, K., Meng, C.I., Rich, F.J., 2007. A nearly universal solar wind-magnetosphere coupling function inferred from 10 magnetospheric state variables. *Journal of Geophysical Research: Space Physics* 112.
- Pérez, F., Granger, B.E., 2007. IPython: a System for Interactive Scientific Computing. *Computing in Science and Engineering* 9, 21–29.
- Pozzo, W.D., Berry, C., Ghosh, A., Haines, T., Singer, L., Vecchio, A., 2018. Dirichlet process gaussian-mixture model: An application to localizing coalescing binary neutron stars with gravitational-wave observations arXiv:1801.08009.
- Tan, Y., Hu, Q., Wang, Z., Zhong, Q., 2017. Geomagnetic index  $K_p$  forecasting with lstm. *Space Weather* 16, 406–416.
- Wing, S., Johnson, J.R., Jen, J., Meng, C.I., Sibeck, D.G., Bechtold, K., Freeman, J., Costello, K., Balikhin, M., Takahashi, K., 2004.  $K_p$  forecast models. *Journal of Geophysical Research: Space Physics* 110.
- Xu, F., Borovsky, J.E., 2014. A new four-plasma categorization scheme for the solar wind. *Journal of Geophysical Research: Space Physics* 120, 70–100.



# Global Simulation of Electron Cyclotron Harmonic Wave Instability in a Storm-time Magnetosphere

Xu Liu

*William B. Hanson Center for Space Science, University of Texas at Dallas, Richardson, Texas, USA*

Miles A. Engel

*Los Alamos National Laboratory, Los Alamos, New Mexico, USA*

Vania K. Jordanova

*Los Alamos National Laboratory, Los Alamos, New Mexico, USA*

Lunjin Chen

*William B. Hanson Center for Space Science, University of Texas at Dallas, Richardson, Texas, USA*

---

## Abstract

Electron Cyclotron Harmonic Wave (ECH) is an electrostatic emission between electron cyclotron harmonic bands, naturally found in the Earth's magnetosphere. Such emission is dominant for precipitating energetic electron in the magnetotail. Magnetospheric ECH wave is excited by the loss cone distribution of hot electrons (0.1 – 10s keV). Statistically, its intensity is stronger at nightside and dawnside than at dayside and duskside, and increases with the geomagnetic-activity level. In this study, we, for the first time, simulate the global ECH wave evolution during a geo-storm (March 16<sup>th</sup> to March 18<sup>th</sup>, 2013). We use Ring current-Atmosphere interaction Model and Self-Consistent Magnetic (RAM-SCB) Model to simulate electron distribution in the equatorial plane from 3  $R_E$  to 6  $R_E$ , where  $R_E$  is Earth radius, and then use linear growth rate formula of ECH wave to evaluate ECH instability. We find our simulated results are consistent with the statistical observation. ECH wave growth rates are much more enhanced at nightside and dawnside, compared with those at dayside and duskside. During a weak activity prior to the storm, the unstable region of ECH wave locates at  $> 4 R_E$  to 6  $R_E$ , and the instability is moderate at nightside and dawnside. Just before the geo-storm (quiet time), the unstable region moves to 5 ~ 6  $R_E$ , and the ECH instability becomes very weak. During the main phase of the storm, the unstable region can extend to lower altitude (3  $R_E$  to 6  $R_E$ ), and the ECH instability is strongest and can extend to dayside. During the recovery phase, the unstable region returns to 5 ~ 6  $R_E$ , and only midnight instability is strong. The inner boundary of unstable ECH wave region is coincident with the plasmopause location during the storm, because the drifting path of energetic electrons, which store free energy for ECH waves, is well confined outside the plasmopause. Our work greatly advance our understanding of the ECH spatial and temporal evolution during storm times, and is an important step to build a storm-time physical model for ECH waves and their wave normal angles, which is valuable for radiation belt modeling work.

*Keywords:* ECH global instability, RAM-SCB, linear growth rate, geo-storm

---

## 1. Introduction

Electron Cyclotron Harmonic (ECH) waves are an electrostatic emission between electron cyclotron harmonic bands, which is also known as electron Bernstein mode. ECH waves are mostly observed at nightside and dawnside

---

*Email addresses:* xu.liu1@utdallas.edu (Xu Liu), mengel@lanl.gov (Miles A. Engel), vania@lanl.gov (Vania K. Jordanova), lunjin.chen@gmail.com (Lunjin Chen)

within  $\sim 6^\circ$  of the magnetic equator with  $4 < L < 10$  (Meredith *et al.*, 2009) with electric field amplitude up to several mV/m and can extend to magnetotail region with amplitude several tenth mV/m (Zhang *et al.*, 2015). For an enhanced geo-activity, the ECH waves can extend to the dayside and duskside (Ni *et al.*, 2017) and to inner L shell (Meredith *et al.*, 2009) with enhanced intensity. ECH wave is usually observed outside plasmopause.

In the Earth's magnetosphere, ECH waves are thought to be excited by the electron loss-cone distribution (Ashour-Abdalla and Kennel, 1978). Previously, the ECH wave instability is evaluated by solving the analytic hot electrostatic dispersion relation (Ashour-Abdalla and Kennel, 1978) with an electron phase space density composed by the subtraction of two bi-maxwellian distribution (Ashour-Abdalla and Kennel, 1978; Horne, 1989; Horne *et al.*, 2003; Ni *et al.*, 2012; Zhou *et al.*, 2017). However, such phase space density can hardly describe the observed phase space density. Recently, Liu and Chen provide a growth rate formula for ECH wave, which allows the phase space density to have core bi-maxwellian shape and a fine arbitrary shape. Such method is briefly introduced in the next section. By using Liu and Chen's formula, we can fit the observed phase space density by several bi-maxwellians  $f_0$  and find the difference  $f_1$  between observed and fitted phase space density. Then, we can apply the formula to find the linear growth rate of ECH waves.

ECH waves are dominant for forming pulsating aurora (Liang *et al.*, 2010) and diffusive aurora (Ni *et al.*, 2012; Zhang *et al.*, 2015). Liang *et al.* (2011) suggests that the fast flow-driven dipolarization and electron injection from the magnetotail can excite ECH waves, and then, those ECH waves precipitate energetic electron to form diffuse auroras.

To study the ECH wave-driven pitch angle scattering and determine the contributions of ECH waves to the diffuse auroral electron precipitation, one needs a storm-time physical model for ECH waves. In this study, we use RAM-SCB model and Liu and Chen's linear growth rate formula to provide a global ECH instability distribution for the inner magnetosphere during a geo-storm, which greatly advance our understanding of the ECH spatial and temporal evolution during storm times. This work is also an important step to build a storm-time physical model for ECH waves. We briefly introduce RAM-SCB model and Liu and Chen's formula in the section 2. A storm-time case is presented in section 3, followed by the conclusion and discussion.

## 2. Methods

In this section, we introduce the RAM-SCB model, which provides us the global electron phase space density during a chosen time period. Then, we present the Liu and Chen's ECH linear growth rate formula briefly.

### 2.1. RAM-SCB model

The Ring current Atmosphere interactions Model with Self Consistent magnetic field (RAM-SCB) is a model that combines a ring current plasma kinetic model with a 3-D force-balanced magnetic model. The RAM portion solves the particle kinetic equations to yield the bounce-averaged plasma differential flux as function of time, L shell, Magnetic Local Time (MLT), energy and pitch angle for  $H^+$ ,  $He^+$ ,  $O^+$  and  $e^-$ . The computational domain covers all MLT intervals with radial region from 2 to 6.5  $R_E$  in the equator of Solar-Magnetic coordinate. The SCB model provides the magnetic field by solving the force balance equation between  $\mathbf{J} \times \mathbf{B}$  force and pressure gradient force.

### 2.2. ECH linear growth rate formula

To solve the ECH linear growth rate, we consider that the electron distribution with two components  $f = f_0 + f_1$ , in which  $f_0$  is a dominant bi-Mawellian population (shown below), and  $f_1$  is a tenuous and arbitrary population.

$$f_0 = \frac{N_e}{\pi^{3/2} a_{e,\perp}^2 a_{e,\parallel}} \exp\left(-\frac{(v_{\parallel} - v_{e,d})^2}{a_{e,\parallel}^2}\right) \exp\left(-\frac{v_{\perp}^2}{a_{e,\perp}^2}\right) \quad (1)$$

, where  $N_e$ ,  $a_e$  and  $v_{e,d}$  denote number density, thermal velocity and drifting velocity of electron, respectively.

For only considering bi-maxwellian distribution  $f_0$ , the exact solution  $\omega_0$  of hot plasma dispersion relation, equation (1) of Ashour-Abdalla and Kennel (1978), satisfies

$$D_0(\omega_0) = 1 + \sum_n 2 \frac{N_e \omega_{pe}^2}{k^2} e^{-\lambda_e} I_n(\lambda_e) \left( \left( \frac{n \Omega_e}{k_{\parallel} a_{e,\parallel} a_{e,\perp}^2} + \frac{z_{e,n}}{a_{e,\parallel}^2} \right) Z(z_{e,n}) + \frac{1}{a_{e,\parallel}^2} \right) = 0 \quad (2)$$

, where  $k$  denotes wave number.  $\omega_{pe} = (\frac{q_e^2}{\epsilon_0 m_e})^{1/2}$  denotes electron frequency with unit number density, where  $q_e$  and  $m_e$  denote charge and mass of electron.  $\Omega_e$  denotes electron cyclotron frequency,  $\lambda_e = \frac{1}{2}(\frac{k_{\perp} a_{e,\perp}}{\Omega_e})^2$ ,  $I_n$  is first kind modified Bessel function of order  $n$  and  $Z(z_{e,n})$  is plasma dispersion function with argument  $z_{e,n} = \frac{\omega_0 - n\Omega_e - k_{\parallel} v_{e,d}}{a_{e,\parallel} k_{\parallel}}$ .  $\omega_0$  is the root of equation (2), which in general is a complex number.

The total linear growth rate satisfies

$$\omega_i \approx \omega_{0i} + Re \left[ -\frac{Im[D_1(\omega_{0r})]}{\frac{\partial D_0}{\partial \omega} |_{\omega=\omega_0}} \right] \quad (3)$$

, where

$$Im[D_1(\omega_{0r})] = -\sum_n \frac{\omega_{pe}^2}{k^2} \int_0^{\infty} 2\pi^2 v_{\perp} dv_{\perp} \frac{J_n^2}{|k_{\parallel}|} \left( \frac{n\Omega_e}{v_{\perp}} \frac{\partial f_1}{\partial v_{\perp}} + k_{\parallel} \frac{\partial f_1}{\partial v_{\parallel}} \right) \Big|_{v_{\parallel} = \frac{\omega_{0r} - n\Omega_e}{k_{\parallel}}} \quad (4)$$

Here  $\omega_{0r}$  and  $\omega_{0i}$  are real and imaginary part of  $\omega_0$ , respectively.  $J_n$  is first kind Bessel function.

### 3. Global ECH wave instability during a geo-storm

To investigate the ECH wave instability during a geo-storm, we choose a 'GEM event' from March 16<sup>th</sup> to March 18<sup>th</sup>, 2013. Figure 1 shows the storm began around 05:00 UT March 17<sup>th</sup> (Figure 1b), and Dst index reached the minimum around 20:30 UT, then it took two days to recover. During the main and fast recovery phase, the Kp (Figure 1a), Ap (Figure 1c) and AE (Figure 1d) indices enhanced greatly. The peak value of AE index is above 1800 nT. Before this big storm, a weak substorm happened from 00:00 UT to 12:00 UT, March 16<sup>th</sup> (Figure 1d).

We use the RAM-SCB model to simulate the global energetic electron phase space density (PSD) and magnetic field during this time period. Figure 2 shows a global electron PSD at  $L = 6$  with a 3-hour MLT interval at 09:00 UT, March 16<sup>th</sup> (first solid vertical line in Figure 1). The electron PSD is distorted from bi-maxwellian shape as electron drifts eastward. To find the linear instability, the electron PSD is fitted by a bi-maxwellian distribution. Then, the electron can be splitted into two parts: the bi-maxwellian part ( $f_0$  in subsection 2.2) and the difference ( $f_1$  in subsection 2.2) between the PSD from RAM-SCB model and fitted bi-maxwellian distribution.

The ECH instability corresponding to this electron PSD can be evaluated by equations (2)-(4). Figure 3 shows ECH normalized wave frequency and linear growth rate of 1<sup>st</sup> harmonic band as function of  $k/k_0$  and wave normal angle for  $MLT = 0$ ,  $L = 6$  at 09:00 UT, March 16<sup>th</sup>.  $k_0$  here is reciprocal of Larmor radius with thermal velocity of bi-max perpendicular temperature. The wave frequency decreases with  $k/k_0$  and is not sensitive to the wave normal angle at  $k/k_0 < \sim 170$ . However, the growth rate only confines at a small region with very oblique angle.

We then compare the growth rate value of 1<sup>st</sup> and 2<sup>nd</sup> harmonic bands for different L, MLT and for different storm phase. We choose 4 representative moments: 09:00 UT March 16<sup>th</sup> (weak substorm), 02:00 UT March 17<sup>th</sup> (pre-storm, as well as, quiet time), 18:00 UT March 17<sup>th</sup> (main phase) and 08:00 UT March 18<sup>th</sup> (recovery phase), shown by the solid vertical lines in Figure 1.

To erase the impact of the discontinuity of linear growth rate (Figure 3b) caused by the irregularity of electron PSD from RAM-SCB model, we use the mean value of the growth rate from thousandth of peak growth rate to peak growth rate. Figure 4 shows the global ECH wave instability for 1<sup>st</sup> harmonic band at those 4 moments. We find ECH wave growth rate are much more enhanced at nightside and dawnside, compared with those at dayside and duskside for active time (Figure 4a, 4c and 4d), which is consistent with the statistical observation. During the weak activity prior to the storm (Figure 4a), the unstable region of ECH wave locates at  $> 4 R_E$  to  $6 R_E$ , where  $R_E$  is Earth's radius. The instability is moderate at nightside and dawnside. Just before the storm (Figure 4b, quiet time), the unstable region recovers to  $5 \sim 6 R_E$ , and the ECH wave instability becomes very weak. During the main phase of the storm (Figure 4c), the unstable ECH wave region can extend to lower L shell region ( $3 R_E$  to  $6 R_E$ ), and ECH instability is strongest and can extend to dayside. During the recovery phase (Figure 4d), the unstable region returns to  $5 \sim 6 R_E$ , and only midnight instability is strong.

Then, we compare the location of unstable region with the plasmopause location from Liu *et al.* (2015) (sold black lines in Figure 4a-4d). We find the unstable region is always terminated by the plasmopause, because the drifting path of energetic electrons, which store free energy for ECH waves, is well confined outside the plasmopause. Figure 5 shows the global ECH wave instability for 2<sup>nd</sup> harmonic band with same format as Figure 4. It shows similar results compared with 1<sup>st</sup> harmonic band.

#### 4. Conclusion and Discussion

The energetic electron phase space density is simulated for a GEM-event storm (March 16<sup>th</sup>, 2013 to March 19<sup>th</sup>, 2013) by RAM-SCB model. The electron cyclotron harmonic (ECH) wave instability is analyzed for 4 chosen time (weak activity before storm, pre-storm, main phase and recovery phase) for 1<sup>st</sup> and 2<sup>nd</sup> harmonic bands. Our principal conclusions are as follows:

1. The ECH wave instability is stronger at nightside and dawnside, compared with dayside and duskside.
2. The ECH wave instability is very weak at quiet time, and the unstable region is only limited near 5 ~ 6 radii. At the main phase of a geo-storm, the ECH wave instability becomes stronger and the unstable region can extend to dayside and 3 radii in the nightside and dawnside. At the recovery phase, the ECH wave instability becomes weak again and the unstable region returns to 5 ~ 6 radii.
3. The inner boundary of unstable ECH wave region is coincident with the plasmopause during the storm.

We, for the first time, simulate the global ECH wave during a geo-storm by analyzing its instability. Our work greatly advances our understanding of ECH wave spatial and temporal evolution during storm times and is an important step to build a storm-time physical model for ECH waves and their wave normal angles. Such work is valuable for modeling of radiation belt.

For the electron phase density simulation, we do not consider the wave (ex. whistler mode, MS wave and EMIC wave etc) effect on phase space density. It should lead to small difference for weak activity, pre-storm and main phase, because for weak activity, the beginning of the simulation, the simulation time is too short for wave effect. At pre-storm, the wave should be weak and lead small difference for PSD. At main phase, even though the wave intensity is large, but it needs more time to scatter the injected electrons from magnetotail. Only at recovery phase, the wave should lead big difference to the PSD. This may be the reason that the simulated nightside ECH wave instability at recovery phase is still strong. However, the observed ECH wave intensity at recovery phase should be weak. To more realistically simulate the PSD for recovery phase of a storm, we need to include a well-established wave model in the future.

Using just one bi-maxwellian distribution to fit the PSD works well for nightside, but the fitting becomes worse and worse as the electron drifting to the duskside. To better fit the PSD, several bi-maxwellians may be needed for the dayside and duskside magnetosphere. To complete this fitting, we need an automatic method to find the initial guess parameters of those several bi-maxwellians by using non-linear fitting for different L, MLT and time. We will address this question in the future.

#### Acknowledgment

This work is supported by the Los Alamos Space Weather Summer School, ISR groups and Reinhard Friedel. We also acknowledge the great help from the school (co-)director Jesse Woodroffe and Misa Cowee. We acknowledge the help from all the lecturers, administrative and technique support staffs.

#### References

- Ashour-Abdalla, M., and C. F. Kennel (1978), Nonconvective and convective electron cyclotron harmonic instabilities, *J. Geophys. Res.*, *83*, 1531–1543, doi:10.1029/JA083iA04p01531.
- Horne, R. B. (1989), Path-integrated growth of electrostatic waves: The generation of terrestrial myriametric radiation, *J. Geophys. Res.*, *94*(A7), 8,895–8,909.
- Horne, R. B., R. M. Thorne, N. P. Meredith, and R. R. Anderson (2003), Diffuse auroral electron scattering by electron cyclotron harmonic and whistler mode waves during an isolated substorm, *Journal of Geophysical Research: Space Physics*, *108*(A7), doi:10.1029/2002JA009736.

- Li, L. Y., J. B. Cao, J. Y. Yang, J. J. Berthelier, and J.-P. Lebreton (2015), Semiannual and solar activity variations of daytime plasma observed by demeter in the ionosphere-plasmasphere transition region, *J. Geophys. Res.*, *120*(12), 10,640–10,653, doi:10.1002/2015JA021102, 2015JA021102.
- Liang, J., V. Uritsky, E. Donovan, B. Ni, E. Spanswick, T. Trondsen, J. Bonnell, A. Roux, U. Auster, and D. Larson (2010), Themis observations of electron cyclotron harmonic emissions, ulf waves, and pulsating auroras, *Journal of Geophysical Research: Space Physics*, *115*(A10), 235, doi:10.1029/2009JA015148.
- Liang, J., B. Ni, E. Spanswick, M. Kubyskhina, E. F. Donovan, V. M. Uritsky, R. M. Thorne, and V. Angelopoulos (2011), Fast earthward flows, electron cyclotron harmonic waves, and diffuse auroras: Conjunctive observations and a synthesized scenario, *Journal of Geophysical Research: Space Physics*, *116*(A12), 220, doi:10.1029/2011JA017094.
- Liu, X., W. Liu, J. B. Cao, H. S. Fu, J. Yu, and X. Li (2015), Dynamic plasmopause model based on themis measurements, *Journal of Geophysical Research: Space Physics*, *120*(12), 10,543–10,556, doi:10.1002/2015JA021801.
- Meredith, N. P., R. B. Horne, S. A. Glauert, D. N. Baker, S. G. Kanekal, and J. M. Albert (2009), Relativistic electron loss timescales in the slot region, *J. Geophys. Res.*, *114*, A03,222, doi:10.1029/2008JA013889.
- Ni, B., J. Liang, R. M. Thorne, V. Angelopoulos, R. B. Horne, M. Kubyskhina, E. Spanswick, E. F. Donovan, and D. Lummerzheim (2012), Efficient diffuse auroral electron scattering by electrostatic electron cyclotron harmonic waves in the outer magnetosphere: A detailed case study, *Journal of Geophysical Research: Space Physics*, *117*(A1), doi:10.1029/2011JA017095.
- Ni, B., X. Gu, S. Fu, Z. Xiang, and Y. Lou (2017), A statistical survey of electrostatic electron cyclotron harmonic waves based on themis fff wave data, *Journal of Geophysical Research: Space Physics*, *122*(3), 3342–3353, doi:10.1002/2016JA023433.
- Zhang, X., V. Angelopoulos, B. Ni, and R. M. Thorne (2015), Predominance of ech wave contribution to diffuse aurora in earth's outer magnetosphere, *Journal of Geophysical Research: Space Physics*, *120*(1), 295–309, doi:10.1002/2014JA020455.
- Zhou, Q., F. Xiao, C. Yang, S. Liu, Y. He, D. N. Baker, H. E. Spence, G. D. Reeves, and H. O. Funsten (2017), Generation of lower and upper bands of electrostatic electron cyclotron harmonic waves in the van allen radiation belts, *Geophysical Research Letters*, *44*(11), 5251–5258, doi:10.1002/2017GL073051.

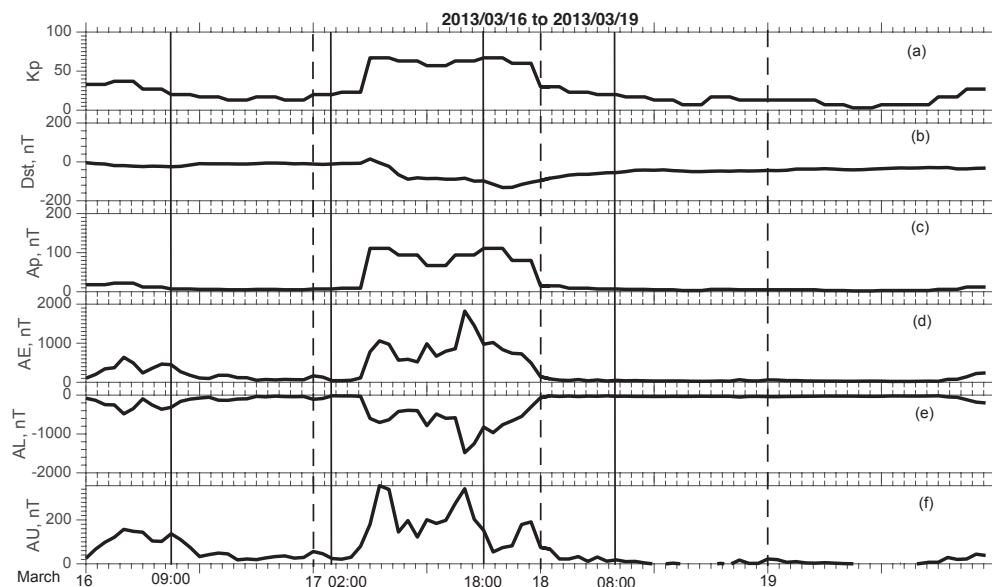


Figure 1: The (a) Kp, (b) Dst, (c) Ap, (d) AE, (e) AL, (f) AU indices from 2013/03/16 to 2013/03/19. A geo-storm happens between 2013/03/17 to 2013/03/18. A weak substorm happens during 00:00 to 12:00 UT 2013/03/16. Vertical solid lines indicate the times used for the analysis.

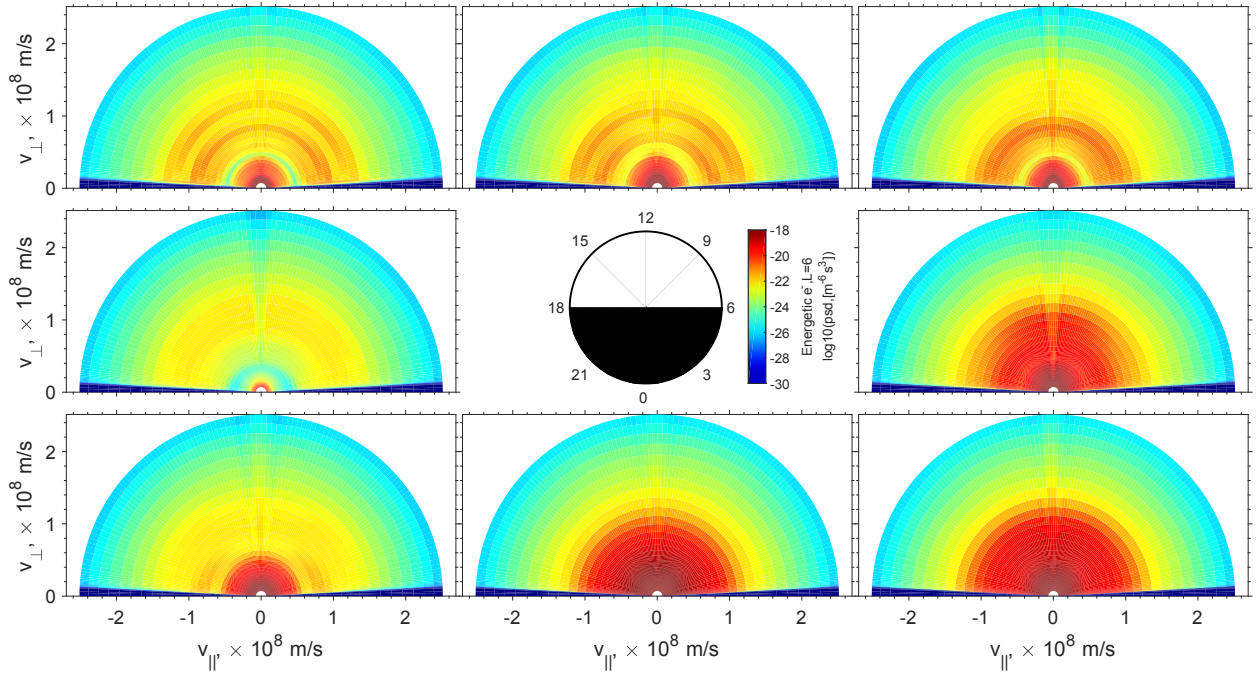


Figure 2: The electron phase space density from RAM-SCB model as function of  $v_{\parallel}$ ,  $v_{\perp}$  and magnetic local time at  $L = 6$ .  $v_{\parallel}$  and  $v_{\perp}$  are parallel and perpendicular velocities, respectively.

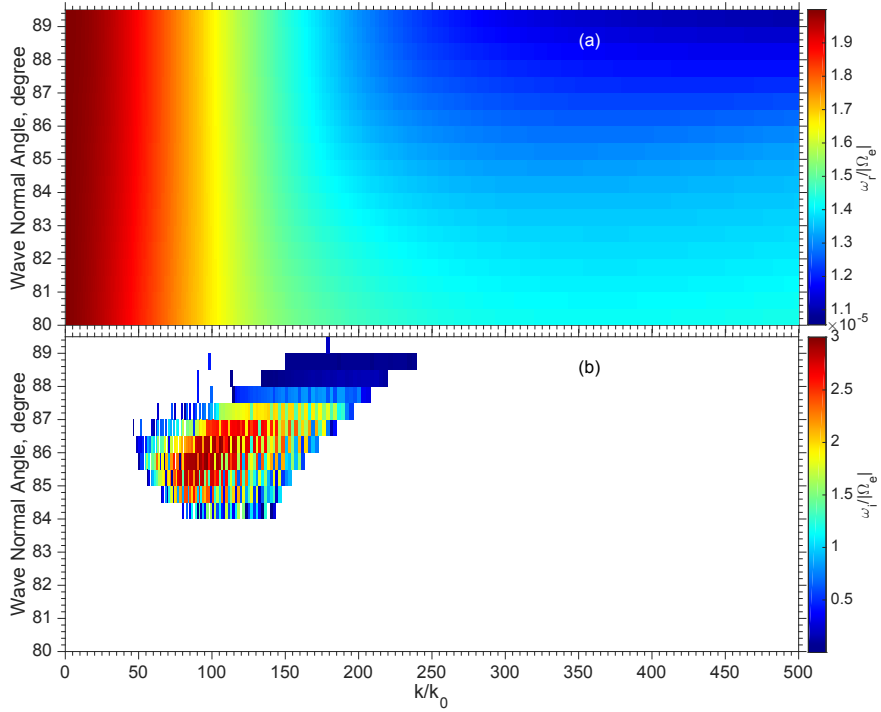


Figure 3: (a) The normalized wave frequency and (b) normalized growth rate as function of normalized  $k/k_0$  and wave normal angle at  $L = 6$  and  $MLT = 0$ .

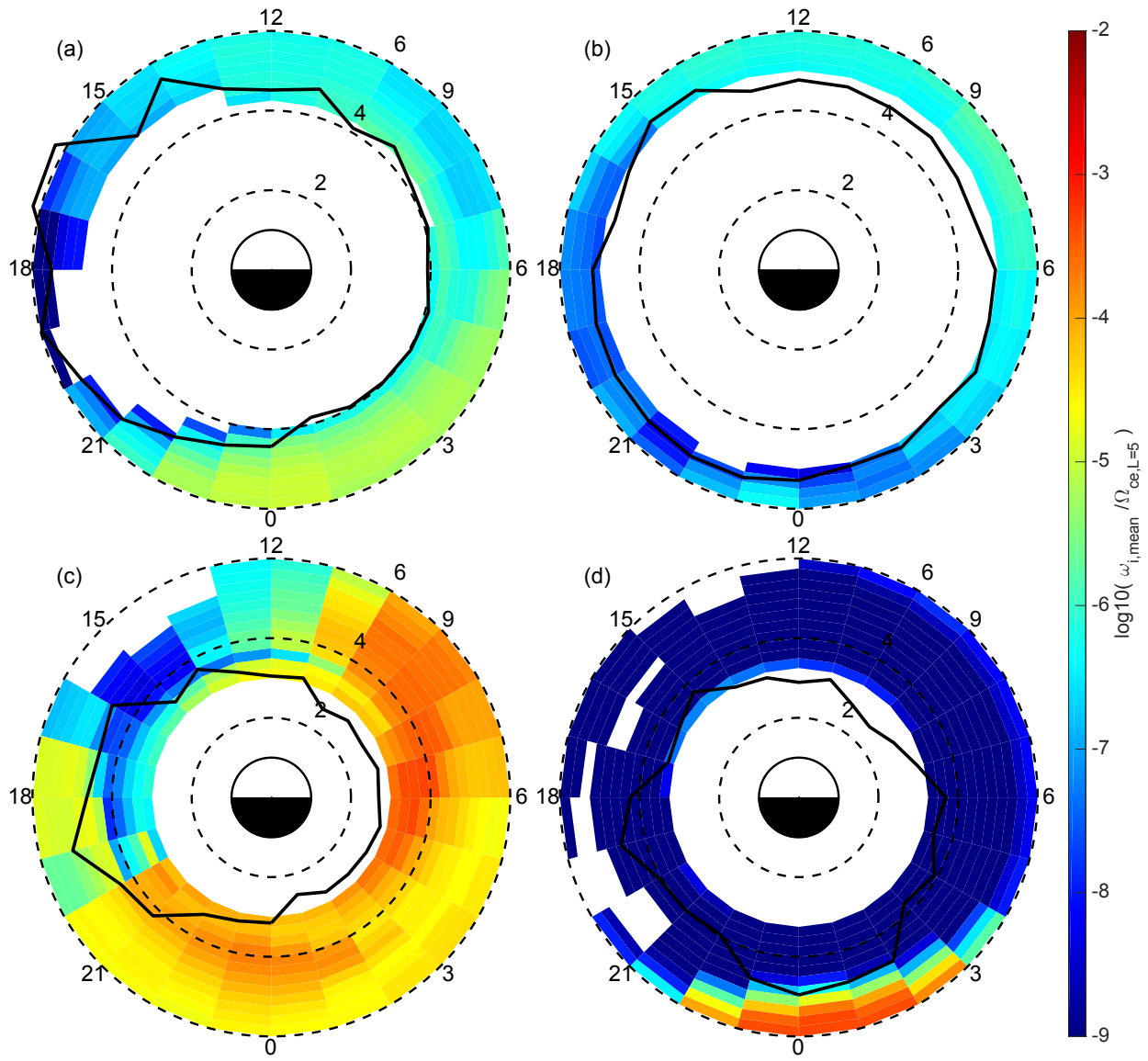


Figure 4: The global ECH wave instability as function of L, MLT at (a) weak activity, (b) pre-storm (quiet time), (c) main phase, (d) recovery phase for 1st harmonic band. solid black lines denotes plasmapause location by *Li et al.* (2015).

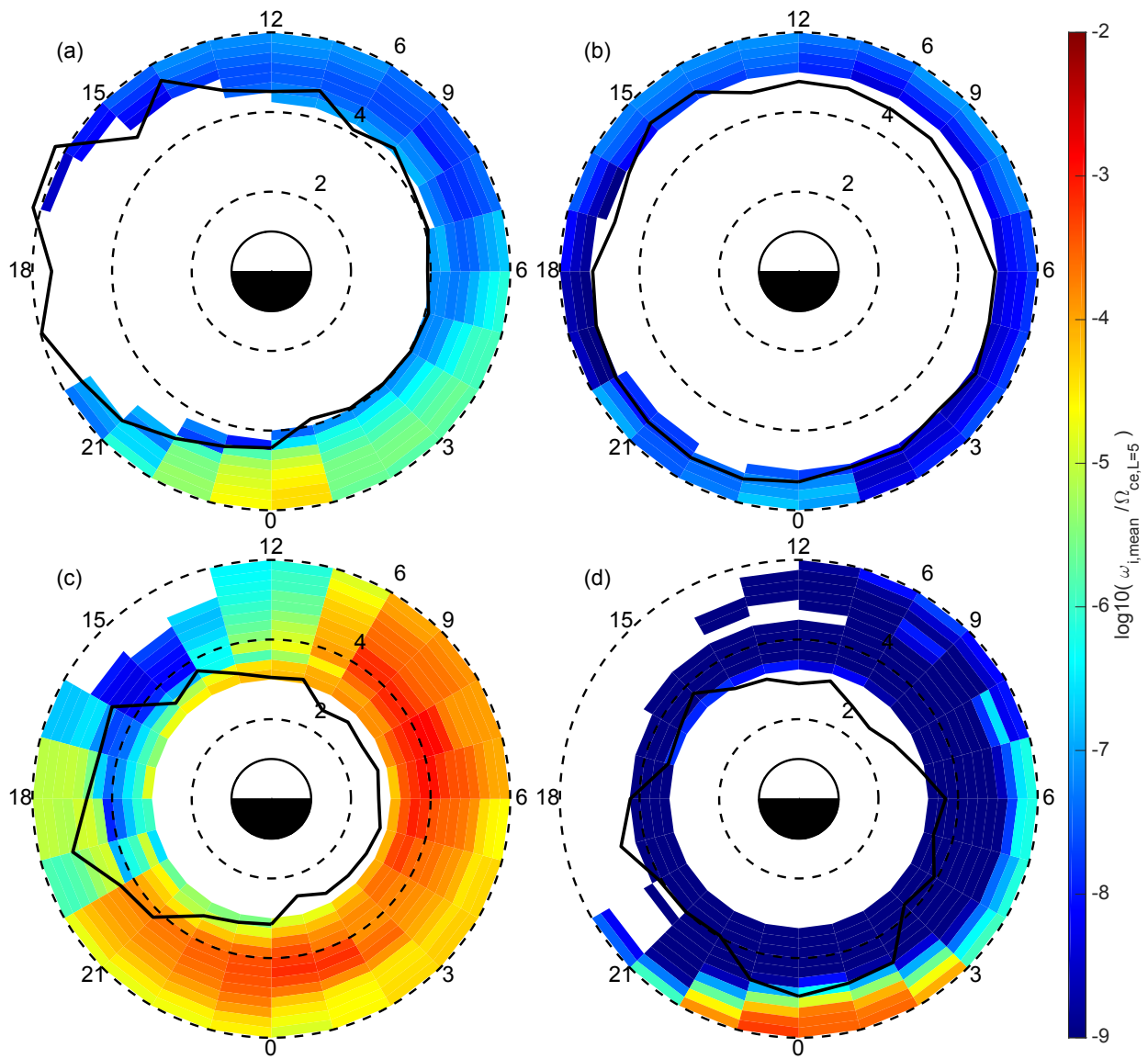




Figure 5: The global ECH wave instability as function of L, MLT for 2nd harmonic band with similar format to Figure 4.



# Systematic Energy Spectra Uncertainty for Particle Detectors

Shumko, M. S. <sup>a,b</sup>, Larsen, B. A. <sup>a</sup>, Fernandes, P. A. <sup>a</sup>

<sup>a</sup>*Los Alamos National Laboratory, Los Alamos, New Mexico, USA*

<sup>b</sup>*Montana State University, Bozeman, Montana, USA*

---

## Abstract

In this study we addressed the effects of systematic uncertainty on energy spectra parameters derived from measurements made by space-borne instruments. A flexible Markov chain Monte Carlo sampler model is presented which can be used to estimate the range of energy spectra that are statistically consistent with observations. Furthermore, the instrument response function uncertainty is considered in the model, which allows for the estimation of systematic uncertainty of the resulting energy spectra as a function of the response function uncertainty.

---

## 1. Introduction

In space physics, quantities such as particle flux, and the phase space density are important to determine the state of the magnetosphere (e.g Fennell et al., 2015; Boyd et al., 2018). The calculation of particle flux from an instrument requires thorough knowledge of the instrument response and its calibration. Since calibration in the lab cannot fully replicate the plasma environment in the magnetosphere, modeling must be done to further understand the instrument response. Analytic models (e.g Sullivan, 1971; Thomas and Willis, 1972) can characterize the instrument response for simple geometries and no particle scattering, but Monte Carlo simulations are required to capture the complexities of real instruments. One such modeling framework is Geant4 (Agostinelli et al., 2003) which has been used extensively to model instrument response as a function of particle energy, species, and direction (e.g Spence et al., 2010; Yando et al., 2011).


Since an instrument convolves the true energy spectra of the incident particle population with the instrument response, doing the reverse to extract the true spectra from the instrument counts is difficult. The spectra can be estimated with either a backward model such as the Bow-Tie analysis (Selesnick and Blake, 2000) or a forward model such as is developed here. The Bow-Tie method is convenient because the count to flux conversion is reduced to a nominal factor, but this factor is calculated from a specified family of spectra, e.g. a power law,

$$F = F_0 E^{-k}, \quad (1)$$

where  $k$  is the power law index,  $F$  is the flux,  $E$  is the energy, and  $F_0$  is the flux magnitude. Since the Bow-Tie analysis uses specified spectra, the flux conversion is most accurate when the true spectra follows that functional form. However, it is difficult to quantify uncertainty in the flux from this method which is caused by imperfect knowledge of instrument response.

Here, we present a forward model using Markov chain Monte Carlo (MCMC) methods. MCMC pseudo-randomly samples a spectral model with the observations, to construct the most likely distributions of the parameters (posteriors) given assumed initial distributions (priors). This model assumes an exponential spectra, and samples the realistic range of spectral parameters with a MCMC sampler to calculate the distribution of spectra parameters that are consistent with the observed counts. A major advantage of this model is that it allows statistical and response function uncertainties to be incorporated and propagated through to the uncertainty in the spectra parameters. For real instruments, systematic uncertainty can arise from a combination of sources including, simplified model geometry, temperature-dependent fields, fringe fields, detector efficiency, and angular response. For simplicity, here the overall response function

---

*Email address:* [msshumko@gmail.com](mailto:msshumko@gmail.com) (Shumko, M. S. )

uncertainty was combined into one parameter to quantitatively show how uncertain the spectra becomes as a function of this one instrument uncertainty.

## 2. Method and Results

To demonstrate the technique in a more concrete manner we explore the impact of systematic uncertainty utilizing the response functions of the Magnetic Electron Ion Spectrometer (MagEIS; Blake et al. (2013)) low energy instrument. MagEIS measures electrons and ions as a part of NASA’s Van Allen Probes mission which launched in 2012 (Mauk et al., 2013; Spence et al., 2013). The MagEIS-Low instrument is sensitive to 20 – 210 keV electrons. Figure 1a shows a diagram of MagEIS which consists of a chamber with an internal magnetic field which guides electrons towards a row of solid state detectors, where they are recorded. The MagEIS response functions were developed by Mark Looper with Geant4 and are shown in Fig. 1b.

To investigate the energy spectra parameter uncertainty an exponential energy spectra is assumed,

$$J = J_0 e^{-E/E_0}, \quad (2)$$

where  $E$  is the energy,  $J$  is the flux, and  $J_0$  and  $E_0$  are the two sampled parameters. Simply, the model consists of the following steps:

1. A “true” spectra is created given a choice of the  $E_0$  and  $J_0$  parameters. This spectra is then convolved with the energy channel-dependent response functions to calculate the “true” counts for the perfect case.
2. Poisson sampling is utilized on the perfect counts and used as data input into the MCMC model. Additionally, the response functions are allowed to move in amplitude and energy cutoff to represent uncertainties in their determination.  $E_0$  and  $J_0$  posterior distributions are then computed.
3. Results are compared to the input spectra and widths (uncertainties) in the posterior distributions explored.

Each of these steps is described in detail in the following sections.

### 2.1. Step 1: Calculate the true count rates

For this simplified model the true count rates were calculated assuming an exponential spectra with  $E_0 = 100$  keV and  $J_0 = 10^4$  (keV cm<sup>2</sup> s sr)<sup>-1</sup>. The energy-dependent flux was then convolved with the MagEIS response functions that are shown in Fig. 1b. This calculation gives us the true (i.e. population) count rates,  $\lambda$ . The sample count rates,  $c$  were picked from a Poisson distribution with a mean of  $\lambda$ . The observed count rates for this example are shown in Fig. 1c as green points.

### 2.2. Step 2: Sample the posterior distribution with the MCMC model

This work utilized PyMC3 (Salvatier et al., 2016), a MCMC library to pick  $E_0$  and  $J_0$  to construct a test spectra. As before, this spectra was then convolved with the MagEIS response functions. The resulting test count rates,  $c_t$  were compared to the observed count rates. In this model, the MCMC algorithm (e.g. (Metropolis et al., 1953)) sampled the posterior distribution  $10^4$  times after the burn-in period to assure convergence. The prior distributions on the spectra parameters were uninformative broad uniform distributions ( $\mathcal{U}$ ) with  $E_0 \sim \mathcal{U}(1, 500)$  and  $J_0 \sim \mathcal{U}(1, 10^6)$ . A few example model code snippets are included in the Appendix.

### 2.3. Step 3: Compare the true spectra to the spectra derived from the posterior distribution

The posterior distributions derived in step 2 demonstrate how well the model compares to the prescribed spectra in step 1. After the model run the MCMC posterior distributions are used to calculate the mean count rates, and are shown with red points in Fig. 1c. The modeled counts converged to the observed counts, which indicates that this model is suitable for this spectra. The modeled spectra are consistent with the prescribed spectra as shown in Fig. 1d (Fig. 1e,f show the spectra with systematic uncertainty which is described below).

The true spectra in Fig. 1d is very close to the modeled spectra calculated from the posterior means  $E_0 = 93 \pm 5$  keV and  $J_0 = 10,500 \pm 500$  (keV cm<sup>2</sup> s sr)<sup>-1</sup>. The 95% credible interval (CI) of the distributions was found to be  $9,500 < J_0 < 11,400$  and  $84 < E_0 < 103$ . In this framework, the 95% CI is interpreted as “from this one observation, we are 95% confident that the true spectra parameters are bounded by the CI”. Since systematic uncertainty was not incorporated yet, this CI represents only the statistical uncertainty.

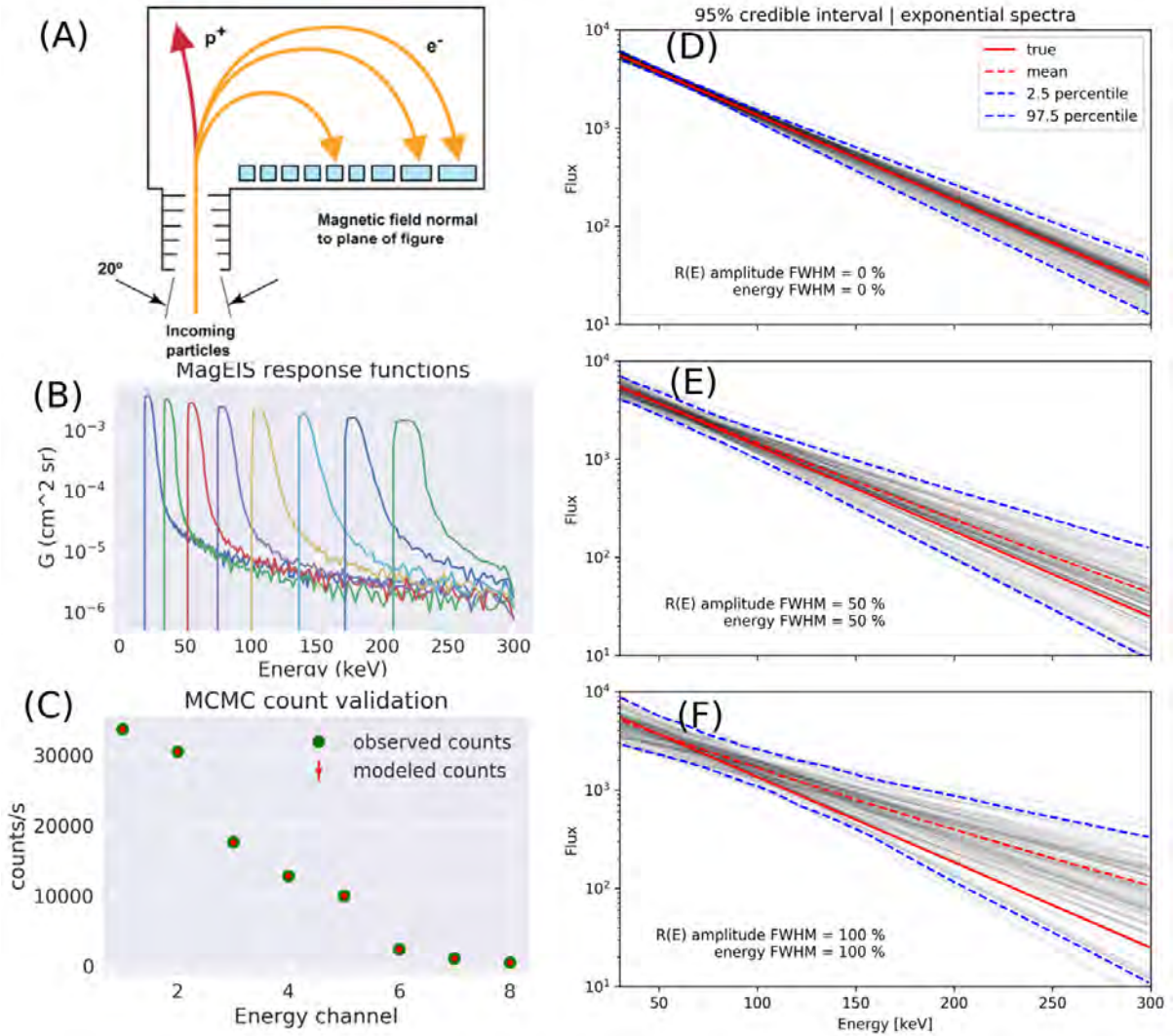


Figure 1: Simplified model overview. (A) MagEIS cross-section, Figure reproduced from Blake et al. (2013). (B) MagEIS-Low instrument response functions integrated over angle, provided by Mark Looper. (C) MCMC validation showing that the mean count rates from the posterior are identical to the observations. (D)-(F) Results from an example run of the simplified model with 10,000 samples after burn-in. The red dashed curve is the true spectra, while the red solid curve is the spectra derived from the mean of the  $E_0$  and  $J_0$  posterior distributions. The dashed blue curves bound the 95% credible interval of the posterior distributions. Panel (D) assumes no systematic uncertainty, and panels (E) and (F) assume a 50% and 100% response function uncertainty in both energy and amplitude.

### 2.3.1. Systematic uncertainty

Incorporating response function uncertainty then allows for the exploration of systematic uncertainties in the derived spectra. Using the same response functions, the amplitude (gain) and energy cutoffs were varied. This transformation can be thought of a translation in energy (left/right) and sensitivity (up/down) of response curves in 1b. The amount that each curve was shifted parameterized by the full width at half maximum (FWHM) as a percent uncertainty. With this methodology, we assume that the total systematic error is captured by the FWHM from all possible sources. After a FWHM was chosen, the MCMC adjusted the response functions by scaling the amplitudes and energies by a factor chosen randomly from a normal distribution,  $\mathcal{N}(1, \text{FWHM})$ . Figure 1e, and 1f show an increasingly wider range of consistent spectra as a function of FWHM.

With this simplified model, we explored how systematic uncertainty compares to statistical uncertainty as a function of FWHM. This model was run for both energy and amplitude FWHM up to 100% (factor of two uncertainty in the response functions) and the results are shown in Fig. 2. Fig. 2 shows the ratio of the total CI and the statistical CI, where the statistical CI was calculated with energy and amplitude FWHM set to 0 %. By design, the relative error in the lower left corner of both panels in Fig. 2 is 0 since there was no systematic uncertainty. As expected, Fig. 2 shows an increase in the systematic uncertainty as a function of FWHM. A relatively small FWHM uncertainty (e.g. 40%) in both energy and amplitude is enough for the systematic and statistical uncertainties to be equal. This is a critical result as relatively small systematic uncertainties can significantly contribute to the spectra uncertainty which is wildly underestimated. Without a full instrument uncertainty quantification, Fig. 2 can give us an idea of how the overall systematic uncertainty compares to statistical uncertainty.

## 3. Discussion and conclusions

The systematic uncertainties that are presented in Fig. 2 as a CI ratio present rules of thumb and do not represent the details of any particular instrument. It is illustrative to note that this work places bounds on how well one must understand the calibration in order to account for the uncertainties present.

This model is flexible and it can adapt to different types of response function transformations, as well as a variety of prior distributions. Besides the uninformative uniform prior, other priors such as  $\mathcal{N}(\mu, \sigma^2)$  has been explored, with similar results. Since the results in Fig. 2 shows a ratio of the systematic to statistical uncertainty, the choice of priors should not drastically influence the ratio. In the future, this model can be used on real data to determine which functional spectra better describes the data. Other spectra models can also include piecewise spectra. Lastly, this model can include outlier detection which flags data that are statistically unlikely (e.g. outside of the CI range).

One property of the Poisson distribution that biases these results is its asymmetry at low  $\lambda$ . When evaluating the likelihood the model overestimates the count rates in the low count regimes. Since plasma in the magnetosphere typically follows falling spectra as a function of energy, this bias hardens the spectra (increase  $E_0$ ) and decrease  $J_0$ .

To make more informed decisions from the data, one needs to consider uncertainty from imperfect instrument design, missing physics, edge effects, etc. When the scientist is informed by the data and its uncertainties, he/she can confidently make claims, and validate models. While this is a simplified model, it is general and flexible enough to incorporate further systematic uncertainty, and a variety of functional spectra to the uncertainty estimation.

## 4. Acknowledgments

We acknowledge the insight into the MagEIS instrument from T.P. O'Brien, S.G. Claudepierre, M.D. Looper, J.B. Blake, and J.G. Sample. The authors acknowledges the MCMC advise from M. Henderson and G.S. Cunningham. Lastly, one author (MS) acknowledges the assistance with the development of the initial MCMC simplified model from I. Michau. This work was sponsored by the Los Alamos National Laboratory's Space Weather Summer School.

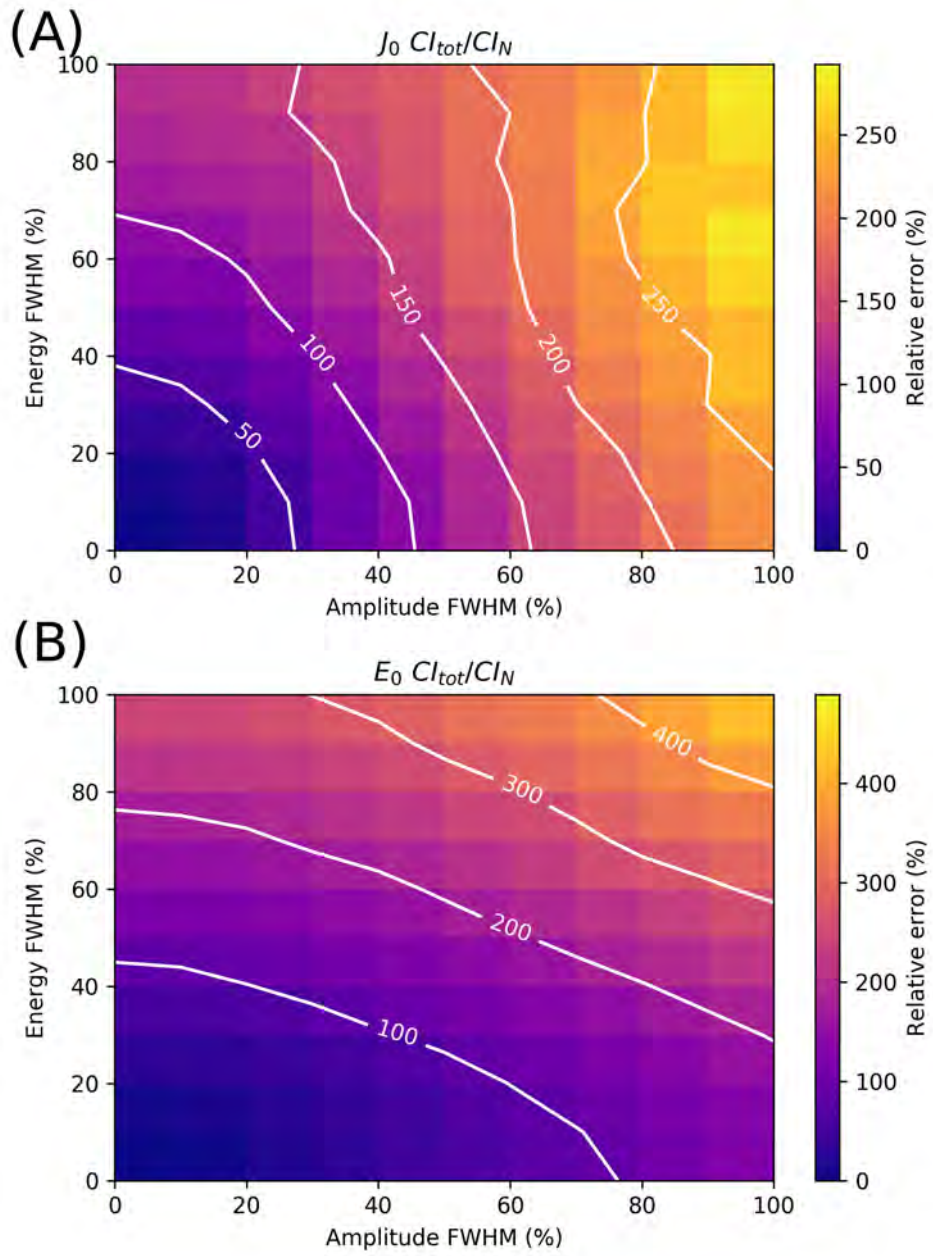


Figure 2: Ratio of the total uncertainty CI to the statistical CI as a function of amplitude and energy FWHM for  $E_0$ .

## Appendix A. Model code

This appendix contains example code snippets of the Python MCMC model. The complete code is found at <https://gitlab.com/mshumko/mageis-stats>.

This code snippet reproduces the statistical uncertainty MCMC.

---

```
m = pm.Model()

def lam(J, E0):
    """
    This function appears to be the only way to correctly work with pymc3 and
    propagate the sampled spectra through the 7 instrument response functions.
    """
    lams = 7*[None]
    for i in range(len(c_obs)):
        lams[i] = pm.Deterministic(
            'lam{}'.format(i),
            dE*pm.math.dot(J, R.response(R0=R0, Earr=Earr, ch=i))
        )
    return lams

with m:
    # Prior stochastic variables
    J0 = pm.Uniform('J0', lower=1, upper=1E6)
    E0 = pm.Uniform('E0', lower=1, upper=500)

    # Define an exponential spectra
    J = J0*pm.math.exp(-Earr/E0)

    lams = lam(J, E0)
    c_m = pm.Poisson('c_m', mu=lams, observed=c_obs, shape=len(c_obs))
    trace = pm.sample(1E4, tuning=2000, cores=3)
```

---

This code snippet reproduces the systematic uncertainty MCMC.

---

```
informedPrior = True # use uniform or normal priors on J0 and E0.
# This sets the R(E) scale to unity or normally distributed.
# If False, will not modify the response functions.
Roffset = 50 # R(E) fwhm amplitude offset off if 0 (percent)
Eoffset = 50 # R(E) fwhm energy offset off if 0 (percent)

def getPriors(informedSpecP, Roffset, Eoffset):
    """
    This function handles the exponential spectra priors,
    and can add uncertainty to the G(E) amplitude and
    energy offset.
    """
    if informedSpecP:
        BoundedNormal = pm.Bound(pm.Normal, lower=0.0)
        J0 = BoundedNormal('J0', mu=1E4, sd=1E5)
        E0 = BoundedNormal('E0', mu=100, sd=10)
    else:
        J0 = pm.Uniform('J0', lower=0, upper=1E7)
        E0 = pm.Uniform('E0', lower=0, upper=500)

    # G(E) modifications
    if Roffset:
        Roff = pm.Normal('Roff', mu=1,
                        sd=Roffset/(100*2*np.sqrt(2*np.log(2))),
                        shape=len(c_obs))
    else:
        Roff = np.ones_like(c_obs)
    if Eoffset:
        Eoff = pm.Normal('Eoff', mu=1,
                        sd=Eoffset/(100*2*np.sqrt(2*np.log(2))),
                        shape=len(c_obs))
    else:
        Eoff = np.ones_like(c_obs)
    return E0, J0, Roff, Eoff

def lam(E0, J0, Roffset, Eoffset):
    """
    This function appears to be the only way to correctly work with pymc3 and
    propagate the sampled spectra through the instrument response functions.
    My implementation of trapezium is not the fastest, but it will do.
    """
    lams = len(c_obs)*[None]

    for i in range(len(c_obs)):
        J = pymcExpSpectra(E*Eoffset[i], E0, J0)
        #f is channel-dependent offset * flux arr * interpolated
        # G(E * a random energy offset)
        f = Roffset[i]*J*G(E)[i]
        lams[i] = pm.Deterministic('lam{}'.format(i), pymcTrapz(f, E))
    return lams

m = pm.Model()
with m:
    # Prior stochastic variables
```

```
prior = getPriors(informedPrior, Roffset, Eoffset)
lams = lam(*prior) # Get prior deterministic variables

c_m = pm.Poisson('c_m', mu=lams, observed=c_obs, shape=len(c_obs)) # Likelihood
trace = pm.sample(1E4, tuning=10, cores=3) # MCMC
```

---



## References

- Agostinelli, S., Allison, J., Amako, K.a., Apostolakis, J., Araujo, H., Arce, P., Asai, M., Axen, D., Banerjee, S., Barrand, G., et al., 2003. Geant4 simulation toolkit. *Nuclear instruments and methods in physics research section A: Accelerators, Spectrometers, Detectors and Associated Equipment* 506, 250–303.
- Blake, J., Carranza, P., Claudepierre, S., Clemmons, J., Crain, W., Dotan, Y., Fennell, J., Fuentes, F., Galvan, R., George, J., et al., 2013. The magnetic electron ion spectrometer (MagEIS) instruments aboard the radiation belt storm probes (RBSP) spacecraft. *Space Science Reviews* 179, 383–421.
- Boyd, A., Turner, D., Reeves, G., Spence, H., Baker, D., Blake, J., 2018. What causes radiation belt enhancements: A survey of the van allen probes era. *Geophysical Research Letters* 45, 5253–5259.
- Fennell, J., Claudepierre, S., Blake, J., O'Brien, T., Clemmons, J., Baker, D., Spence, H.E., Reeves, G., 2015. Van allen probes show that the inner radiation zone contains no mev electrons: Ect/mageis data. *Geophysical Research Letters* 42, 1283–1289.
- Mauk, B., Fox, N.J., Kanekal, S., Kessel, R., Sibeck, D., Ukhorskiy, A., 2013. Science objectives and rationale for the radiation belt storm probes mission. *Space Science Reviews* 179, 3–27.
- Metropolis, N., Rosenbluth, A.W., Rosenbluth, M.N., Teller, A.H., Teller, E., 1953. Equation of state calculations by fast computing machines. *The journal of chemical physics* 21, 1087–1092.
- Salvatier, J., Wiecki, T.V., Fonnesbeck, C., 2016. Pymc3: Python probabilistic programming framework. *Astrophysics Source Code Library* .
- Selesnick, R., Blake, J., 2000. On the source location of radiation belt relativistic electrons. *Journal of Geophysical Research: Space Physics* 105, 2607–2624.
- Spence, H.E., Case, A., Golightly, M., Heine, T., Larsen, B., Blake, J., Caranza, P., Crain, W., George, J., Lalic, M., et al., 2010. Crater: The cosmic ray telescope for the effects of radiation experiment on the lunar reconnaissance orbiter mission. *Space science reviews* 150, 243–284.
- Spence, H.E., Reeves, G., Baker, D., Blake, J., Bolton, M., Bourdarie, S., Chan, A., Claudepierre, S., Clemmons, J., Cravens, J., et al., 2013. Science goals and overview of the radiation belt storm probes (rbsp) energetic particle, composition, and thermal plasma (ect) suite on nasas van allen probes mission. *Space Science Reviews* 179, 311–336.
- Sullivan, J., 1971. Geometric factor and directional response of single and multi-element particle telescopes. *Nuclear Instruments and methods* 95, 5–11.
- Thomas, G., Willis, D., 1972. Analytical derivation of the geometric factor of a particle detector having circular or rectangular geometry. *Journal of Physics E: Scientific Instruments* 5, 260.
- Yando, K., Millan, R.M., Green, J.C., Evans, D.S., 2011. A monte carlo simulation of the noaa poes medium energy proton and electron detector instrument. *Journal of Geophysical Research: Space Physics* 116.



# Deriving Coronal Shock Properties from MHD Coronal Mass Ejection Simulations

Talwinder Singh

*Department of Space Science, The University of Alabama in Huntsville, AL 35805, USA*

Fan Guo

*Theoretical Division, Los Alamos National Laboratory, NM 87545 USA*

Mehmet S. Yalim

*Center for Space Plasma and Aeronomic Research, The University of Alabama in Huntsville, AL 35805, USA*

Nikolai Pogorelov

*Department of Space Science, The University of Alabama in Huntsville, AL 35805, USA*

---

## Abstract

Particle acceleration by CME driven coronal shocks is of great interest to space physics community as the accelerated energetic particles can have adverse impacts on astronauts and satellites. Therefore, there is an urgent need to understand their origin to try and predict their properties. Computer simulations of the acceleration process is a promising tool for this purpose. To model realistic particle acceleration, we need data driven shock properties such as its 3-d geometry, speed and upstream and downstream plasma values such as density, speed and magnetic field. In this study, we derive these shock properties using MHD simulations of a Gibson-Low (GL) flux rope based CME propagating in a data driven solar wind background. GL flux rope parameters are constrained using observed CME speed and poloidal flux. Background solar wind is simulated using radial synoptic magnetogram at the inner boundary. We use the upstream and downstream plasma parameters to derive shock properties such as compression ratio and Mach number.

---

## 1. Introduction

Solar eruptions are sometimes associated with acceleration of particles like protons, electrons and heavy ions, that can increase their speeds to near relativistic speed limits (Reames 1999, Desai & Giacalone 2016). These particles are called Solar Energetic Particles (SEPs) and can follow interplanetary magnetic field lines to reach Earth. Since western hemisphere of Sun is magnetically connected to Earth due to Parker spiral, events in that region can send SEPs to Earth (Gopalswamy et al. 2012). There are two main mechanisms for particle acceleration during solar eruptions: (a) particle acceleration by magnetic reconnection in a solar flare and (b) particle acceleration by coronal shocks traveling in front of the CME.

---

*Email addresses:* talwinder.singh@uah.edu (Talwinder Singh), guofan@lanl.gov (Fan Guo), tmsy0002@uah.edu (Mehmet S. Yalim), np0002@uah.edu (Nikolai Pogorelov)

Particle acceleration by coronal shocks is the main focus of this study. The main process of particle acceleration in this case is the diffusive shock acceleration in which the particles move across the shock multiple times and gaining energy (Axford et al. 1977, Krymsky 1977). This acceleration has been shown to be dependent on the shock geometry, speed and shock upstream and downstream plasma parameters. The most important ones are the compression ratio of the shock and the angle between shock normal and upstream magnetic field vector. Perpendicular shock are more suitable for particle acceleration (Jokipii 1987). The other parameter that greatly impacts the SEP event flux is the presence of seed particles for shock to accelerate (Kahler et al. 2000). Most of the high energy SEPs originate when shock is below  $4 R_{\odot}$ . It has also been observed that more energetic SEP events were associated with multiple CMEs interacting in corona indicating the plasma in leading CME is providing seed particles to shock of the trailing CME's shock (Gopalswamy et al. 2004, Li et al. 2012).

Kong et al. (2017) simulated particle acceleration by assuming an analytic circular front shock and simplified streamer belt and radial configuration of coronal magnetic field. They found that the coronal magnetic field configuration plays an important role in the acceleration process. In this study, we aim at deriving shock properties and coronal magnetic field configuration from data so that a more realistic data driven study can be done. Section 2 shows the models for solar wind background and CME used in this study. In section 3, we show how model parameters can be constrained by observations. Section 4 shows the simulations results and finally concluding remarks are given in section 5.

## 2. Models

### 2.1. Global Solar Corona Model

A global MHD model of solar corona has been developed in Multi-Scale Fluid-Kinetic Simulation Suite (MS-FLUKSS, Pogorelov et al 2014, Yalim et al. 2017) (See Fig 1). This model is designed to be driven by a variety of observational solar magnetogram data. It solves the set of ideal MHD equations in inertial or corotating frame of reference with the Sun using volumetric heating source terms to model solar wind acceleration according to Nakamizo et al.(2009). This results in simulation of various solar magnetic structures such as streamers and coronal holes. The initial solution for magnetic field is calculated by Potential Field Source Surface (PFSS) method using either a spherical harmonics approach or a finite difference method by incorporating the solution provided by the Finite Difference Iterative Potential-field Solver(FDIPS) code (Toth et al. 2011) into MS-FLUKSS. For the rest of the plasma parameters, the initial solution is computed from Parker's isothermal solar wind model (Parker 1958).

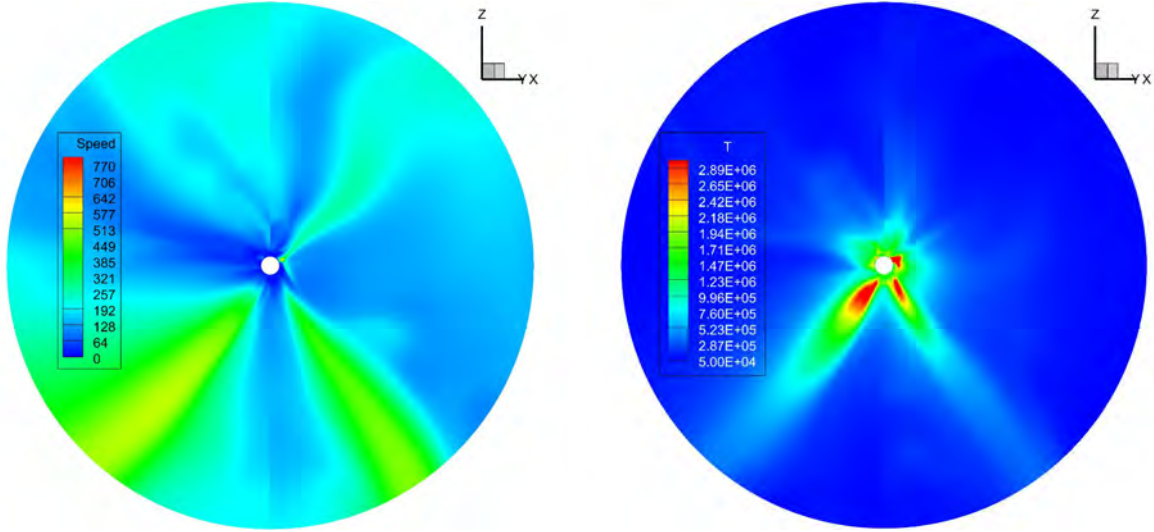


Figure 1: Solar wind background simulated using HMI LOS magnetogram of 7 March 2011 06:00 UT: (left) speed contours (km/s); (right) temperature contours (K).

## 2.2. Gibson Low flux rope model

Since CMEs have flux rope structure associated with them that drives the bulk plasma motion away from the Sun, we chose to use a flux rope based CME model called Gibson-Low (FL) flux rope model in this study (Gibson & Low 1998). This should result in more realistic CME parameters and by extension, more realistic shock parameters. Solution to GL flux rope is found by solving the force balance equation and Gauss's law for magnetism using Ideal MHD equations. This results in an analytical solution of spherical magnetic torus that can be stretched under the transformation  $r = r - a$  in spherical coordinates to convert it into a tear drop shape (Fig 2). The analytical solution of GL flux rope requires four parameters:

- Flux rope radius( $r_0$ ): This is the radius of initial GL spherical torus before stretching.
- Flux rope height ( $r_1$ ): This is the height of the center of the introduced spherical torus before stretching.
- Flux rope stretching parameter ( $a$ ): This is the amount by which each part of the spherical torus is stretched towards the origin.
- Flux rope field strength ( $a_1$ ): This is a free parameters that controls the magnetic field strength and pressure inside the flux rope being introduced.

As seen in fig. 2, the magnetic field lines imitate the flux rope in a CME and the mass is distributed like the typical 3 part structure of the CME, with bright front, dark cavity that contains flux rope and a bright core. To simulate a CME, the analytic solution of the flux rope is superimposed on the background solar wind. Due to unbalance in pressure with the background, the flux rope erupts as a CME.

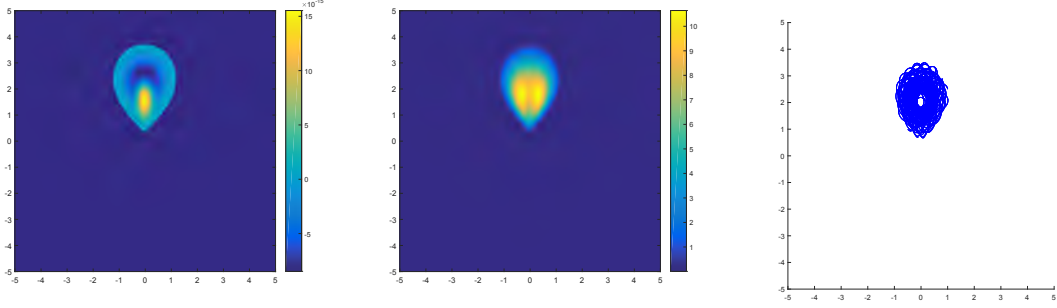


Figure 2: (From left to right) Density ( $g/cm^3$ ), magnetic field magnitude ( $G$ ), and magnetic field lines in stretched GL torus. All horizontal and vertical axis are in  $R_{\odot}$ . We used  $r_0 = 1.67$ ,  $r_1 = 3.03$ ,  $a = 1.01$  and  $a_1 = 0.23$  in these figures.  $(0,0)$  coordinate represents solar center.

### 3. Deriving parameters

To have realistic shock parameters, we need to simulate the solar wind background as well as the CME to match observations. Using synoptic magnetograms and volumetric expansion terms given in Nakamizo et. al. (2009), we get a background that matches observations in key coronal structures like active regions, coronal holes and streamers. To match the CME with observations we need to properly adjust the GL flux rope parameters. The key observations of the CME to match with simulation are its speed, direction, tilt and poloidal flux.

We have used Graduated Cylindrical Shell (GCS) model to derive CME speed, direction and tilt angle using multiple viewpoints of STEREO A, B Cor-2 and SOHO C3 coronagraphs (Thernisien et. al. 2006). GCS model consists of two conical legs and a circular front and can be adjusted in height, latitude, longitude, tilt, half angle and filling ratio to fit on a CME as seen from multiple viewpoints (See fig. 3). Doing this for a time series and finding height-time relation can give us the CME speed.

Poloidal flux of a CME cannot be calculated directly through coronagraph observations. Therefore we use an empirical relation given by Gopalswamy et al (2017) stating that the poloidal flux of a CME is equal to the reconnected flux in the source active region after the CME eruption. Reconnected flux can be calculated as half the unsigned radial flux in the magnetogram area covered by the Post Eruption Arcades (PEAs) (See fig. 4). While using this method, we need to restrict ourselves to CMEs that erupt from active regions within  $30^\circ$  latitude and longitude as otherwise the projection effect introduces errors in flux estimation.

To simulate a CME, a GL flux rope analytic solution is added to the background with GCS calculated location and tilt. The GL parameters required by the analytic solution are constrained using observed speed and poloidal flux of the CME. Singh et. al. (2018) found an empirical relation between speed of simulated CME, average background pressure in simulated solar wind and GL parameters. It can be given as:

$$V_{\text{CME}} = \begin{cases} (c_1 a_1 r_0^4 + c_2) \cdot (c_3 P_{\text{avg}} + c_4) \cdot (c_5 r_1 + c_6) & r_1 < 2.6 \\ (c_1 a_1 r_0^4 + c_2) \cdot (c_3 P_{\text{avg}} + c_4) & r_1 \geq 2.6 \end{cases} \quad (1)$$

where  $V_{\text{CME}}$  is the simulated speed of the CME,  $P_{\text{avg}}$  is the average solar wind pressure in the direction of CME propagation and  $r_1$ ,  $r_0$ ,  $a$  and  $a_1$  are GL parameters.  $c_i$ 's are constants found using a parametric study in Singh et. al. (2018). Using this relation, the speed of simulated CME can be found for every combination of GL parameters. We can also find poloidal flux of GL flux rope from its analytical solution. To find GL parameters to be used, we vary the

GL parameters in a range and find the combination of GL parameters that match simulated speed and poloidal flux of CME with the observed values.

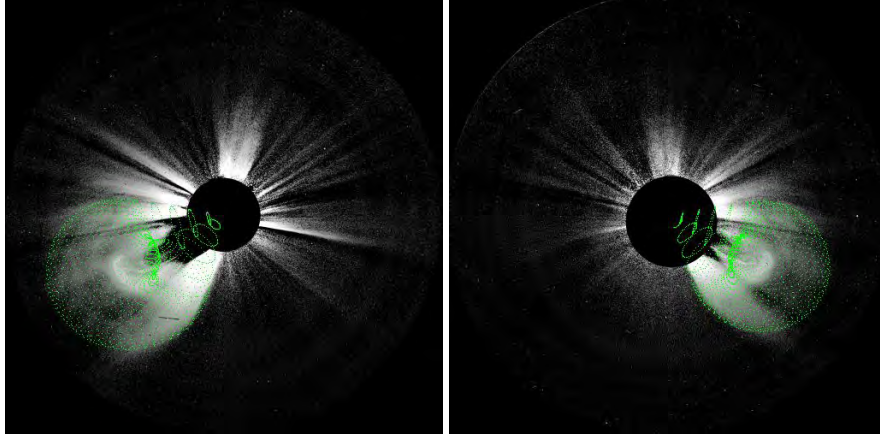


Figure 3: Graduate Cylindrical Shell (GCS) model applied to a CME observed by 2 viewpoints of STEREO A (*left*) and B (*right*). This model can be used to find CME speed, direction and tilt angle.

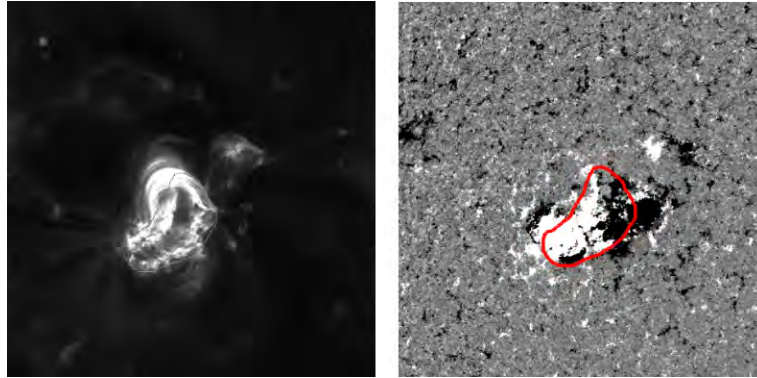


Figure 4: (*left*) Post eruption arcade (PEA) seen after the CME eruption in 193 Å wavelength EUVI imager onboard SDO (*right*) Same active region as seen in HMI magnetogram onboard SDO overlotted by the PEA area.

#### 4. Simulation Results

In this study, we use a CME that occurred on 7 March 2011 at 14:00 and was Earth directed. It was clearly seen by STEREO A & B and therefore, GCS method could be easily implemented on it. Also, the source active region AR-11166 was within  $\pm 30^\circ$  latitude and longitude thus reducing the error in magnetic flux calculation from magnetogram. We use CR-2107 synoptic magnetogram to simulate solar wind background as shown in fig. 1. We use spherical domain with resolution of  $180 \times 120 \times 240$  in  $r$ ,  $\theta$  and  $\phi$  with  $r$  ranging from  $1.03 R_\odot$  to  $30 R_\odot$ . We measured the CME speed as 812 Km/s and direction as  $-24^\circ$  longitude and  $+18^\circ$  latitude using GCS method. The tilt of the CME was found to be  $+85^\circ$  w.r.t. solar equator. The flux from post eruption arcade area as  $4.85 \times 10^{21}$  Mx. For these values, we found that using  $a_1$ ,  $r_0$ ,  $r_1$  and  $a$  as 2.51, 0.52, 1.34 and 0.14 respectively should simulate CME with speed 907 Km/s and poloidal flux  $4.90 \times 10^{21}$  Mx. With these parameters, the introduced GL mass is  $3.84 \times 10^{15}$

gm which is of the order of typical mass of a CME. These GL parameters ended up simulating a CME with speed 897 Km/s, which is very close to the actual speed. Figs. 5 shows the white light coronagraph image of observed CME compared with synthetic white light image of simulated CME from same viewpoint. Fig. 6 shows the agreement between the height vs. time graphs obtained from the LASCO/C3 observations and the simulation results. This agreement shows the possibility of predicting CME arrival time at 1AU using simulations.

Now that we have data driven CME simulation that matches well with the observations, we find the shock travelling in front of this CME and its properties. We are interested in finding the 3D shape, speed, compression ratio and mach number of the shock. The shock location in front of the CME can be located by the position of pressure jump along radial lines in multiple directions. The normal at each point on Shock is calculated by v-B coplanarity condition (Abraham-Shrauner 1972).

$$\hat{\mathbf{n}} = \frac{\mathbf{B}_1 \times (\mathbf{V}_2 - \mathbf{V}_1) \times (\mathbf{B}_2 - \mathbf{B}_1)}{|\mathbf{B}_1 \times (\mathbf{V}_2 - \mathbf{V}_1) \times (\mathbf{B}_2 - \mathbf{B}_1)|}$$

where  $\mathbf{B}$  and  $\mathbf{V}$  are magnetic field and velocity vectors and “1” and “2” subscripts indicate whether parameters are ahead or behind the shock. Speed of the shock can be found by finding the shock location along the normal direction at a later time. Then for each direction, we go to coordinate system in which the shock is stationary to find compression ratio. Magnetosonic mach number is found as ratio of shock speed in solar wind frame of reference and local magnetosonic wave speed. Figure. 7 shows the shock shape colored according to compression ratio, mach. number and shock speed at each point. Shock normal unit vectors are also shown for each point. Since this was a relatively slower CME with speed 900 Km/s, we see a small compression ratio in the shock. In the future, we will simulate a faster CME that occurred on 12 July 2012 with the discussed method and see its impact on shock properties. That event was associated with SEP detection at 1 AU so it will be more suitable to do diffusive shock acceleration simulations to model SEP generation.

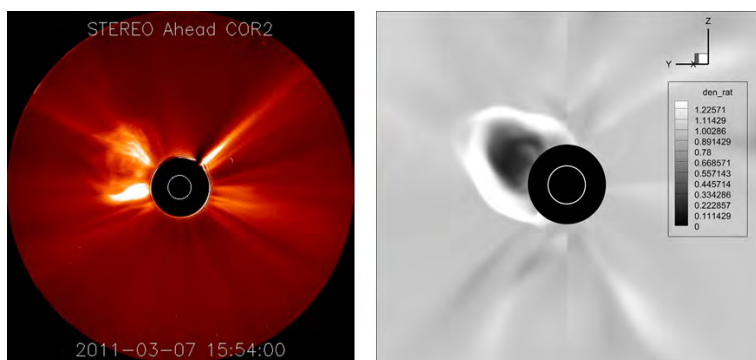


Figure 5: (left) 7 March 2011 CME observed by STEREO A Cor 2 coronagraph (right) Same CME simulated using GL flux rope shown by synthetic white light image.



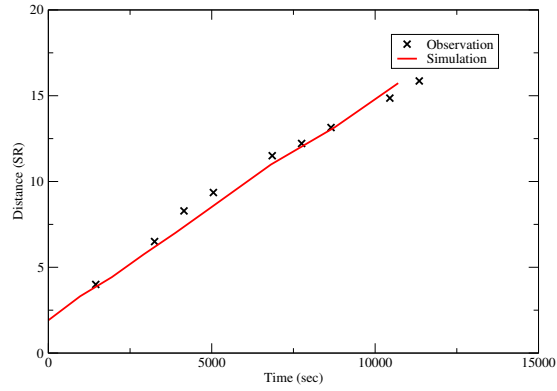


Figure 6: Height-Time graph showing agreement in time evolution of simulated and observed CMEs

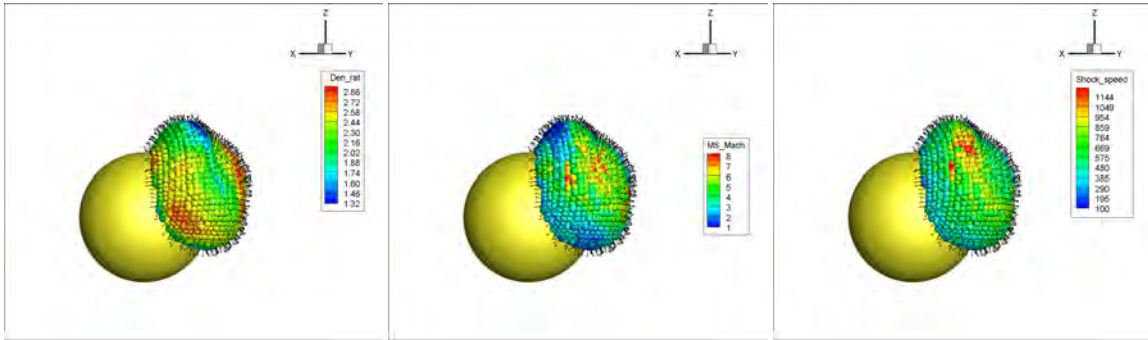


Figure 7: (From left to right) Compression Ratio, Mach number, and shock speed for the shock traveling in front of the simulated CME. The arrows in all 3 subpanels show the shock normal unit vector.

## 5. Conclusions

In this study, we have shown how to derive properties of coronal shocks using data driven MHD CME simulations. We simulated a CME that occurred on 7 March 2011 in a data driven solar wind background. We adjusted our model parameters such that simulated CME matches observations in speed, direction, tilt and poloidal flux. The shock traveling in front of the CME was identified by finding location of pressure jump and shock normal at each point on shock was found using v-B coplanarity condition. The shock speed, compression ration and mach number were also found.

This approach can be used to model particle acceleration by this shock by using diffusive shock acceleration simulations similar to Kong et. al. (2017). It will give is useful insight into the exact mechanism and location of particle acceleration in the corona.

## References

- Reames, D. V. 1999, SSRv, 90, 413  
 Desai, M. I., Giacalone, J. 2016, LRSP, 13, 3

Gopalswamy, N., Xie, H., Yashiro, S., et al. 2012, SSRv, 171, 23  
Axford, W. I., Leer, E., Skadron, G. 1977, Proc. ICRC (Plovdiv), 11, 132  
Krymsky, G. F. 1977, DoSSR, 234, 1306  
Jokipii, J. R. 1987, ApJ, 313, 842  
Kahler, S. W., Reames, D. V., Burkepile, J. T. 2000, in ASP Conf. Ser. 206, High Energy Solar Physics Workshop, ed. R. Ramaty N. Mandzhavidze (San Francisco, CA: ASP), 468  
Gopalswamy, N., Yashiro, S., Krucker, S. 2004, JGR, 109, A12105  
Li, G., Moore, R., Mewaldt, R. A., et al. 2012, SSRv, 171, 141  
Kong, X., Guo, F., Giacalone, J., Li, H., Chen Y. 2017, ApJ, 851,38  
Pogorelov, N., Borovikov, S., Heerikhuisen, J., Kim, T., Kryukov, I., Zank, G. 2014, XSEDE 2014 Proc., 22  
Yalim, M. S., Pogorelov, N. V., Liu, Y. 2017, in IOP Conf. Series: Journal of Physics: Conf. Series, 837, 012015  
Nakamizo, A., Tanaka, T., Kubo, Y., et al. 2009, J. Geophys. Res., 114, A07109  
Parker, E. N. 1958, ApJ, 128, 664  
Gibson, S. E., Low, B. C. 1998, ApJ, 493, 460  
Thernisien, A. F. R., Howard, R. A., Vourlidas, A. 2006, ApJ, 652, 763  
Gopalswamy, N., Akiyama, S., Yashiro, S., Xie, H. 2017, Proceedings IAU Symposium No. 335, 2017  
Singh, T., Yalim, M., Pogorelov, N. 2018, ApJ 864, 18  
Abraham-Shrauner, B. 1972, GJR-SP, 77, 4

# Measuring geomagnetic cutoff with GPS energetic proton data

Alexandra M. Wold

*University of Colorado Boulder, Boulder, CO*

Matthew R. Carver, Steven K. Morley

*Los Alamos National Laboratory, Los Alamos, NM*

---

## Abstract

The magnetosphere effectively shields low latitudes from most energetic protons. This shielding is dependent upon both the energy and angle of arrival of protons, and the latitude at which a particular energy of proton cannot reach is referred to as the cutoff latitude. The newly available Global Positioning System (GPS) energetic particle data presents an exciting opportunity to study solar energetic particle (SEP) events and cutoff latitude. With more than 20 satellites in 6 orbital planes at MEO covering a wide range of L-shells for a 16 year period (over 190 satellite years), this data set covers a longer time span and greater spatial distribution than most science missions. We present a study of geomagnetic cutoff evaluated with energetic proton measurements from the Combined X-ray and Dosimeter (CXD) instruments onboard the GPS satellites. At a four minute cadence, the CXD instrument detects protons with energies ranging from 10 MeV to >100 MeV on five channels and have been recently cross-calibrated with the NOAA GOES Energetic Particle Sensor. Cutoff latitude can be defined in multiple ways, and we investigate previously used and novel methods of cutoff determination from data. For several SEP events we calculate the GPS observed cutoff using different heuristics and compare to previous studies of cutoff variation during these events. We further compare the GPS-derived cutoff latitudes to modeled cutoffs.

*Keywords:* geomagnetic cutoff, solar energetic particles, GPS

---

## 1. Introduction

### 1.1. Global Positioning System (GPS) as a particle detector

On October 29, 2015, the National Space Weather Strategy and National Space Weather Action Plan was released by the White House Office of Science and Technology. This document instructed federal agencies to make space environment data from the US Air Force's GPS satellites publicly available. Next, in January 2016 the National Oceanic and Atmospheric Administration (NOAA) hosted 4 weeks of GPS energetic particle data from Los Alamos National Lab's (LANL's) sensors, and this was the first time the public could access this data. On August 4, 2016, [Knipp and Giles \(2016\)](#) called for a release of more of the GPS data: “[N]ow is the time for a new data revolution that makes months, if not years, of historical GPS space environment data available to those who support the nation’s space industry.” Finally, on October 13, 2016, under Executive Order 13744 “Coordinating Efforts to Prepare the Nation for Space Weather Events”, 16 years of LANL’s GPS energetic particle data was released. This historic data set covers December 2000 to December 2016 ([Morley et al., 2017](#)).

All GPS satellites are equipped with instruments that measure a wide range of energetic electrons and protons. The Combined X-ray and Dosimeter (CXD) resides on 21 of 31 of the currently operating spacecraft. The Burst Detector Dosimeter for Block II-R (BDD-IIR) resides on 2 currently operating spacecraft. Through using GPS data, we have a data set with a longer time span and greater spatial distribution than previous science missions. With CXD,

---

*Email addresses:* alexandra.wold@colorado.edu (Alexandra M. Wold), mrcarver@lanl.gov (Matthew R. Carver), smorley@lanl.gov (Steven K. Morley)

we have 16 years of data (over 190 satellite years) from the GPS satellites. Figure 1 shows the daily sunspot number versus time with the lifetimes of various missions overlaid. In red, we see CXD equipped satellites covering more than an entire solar cycle. Compared to the Van Allen Probes in blue, GPS cover a much larger time range. GPS have  $\sim 12$  hour orbits, and the CXD measurements are made at a 4 min cadence. The GPS constellation covers six orbital planes in mid-Earth orbit (MEO) at approximately 20,200 km altitude. GPS have a nearly circular orbit and fly through a wide range of L-shells. A visualization of the GPS distribution is shown in Figure 2. Compared to GOES, the science standard for space environment monitoring from geostationary orbit, we can visually see the increase in spatial distribution of GPS measurement from sheer number of satellites alone. With this large spatial distribution, fast cadence, and multi-year coverage, there are exciting opportunities to study the geospace environment (Morley et al., 2016, 2017; Carver et al., 2018).

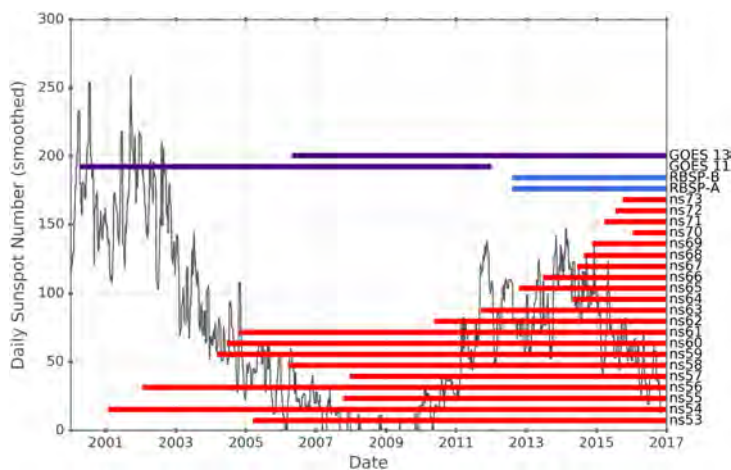


Figure 1: Plot from Carver et al. (2018) illustrating the time coverage of spacecraft from 2000 to 2017. In black, daily sunspot number vs. time. In red, time coverage of CXD-equipped GPS satellites. In blue, time coverage of National Aeronautics and Space Administration Van Allen probes, (purple) time coverage of Geostationary Operational Environmental Satellite Energetic Particle Sensor (GOES EPS).

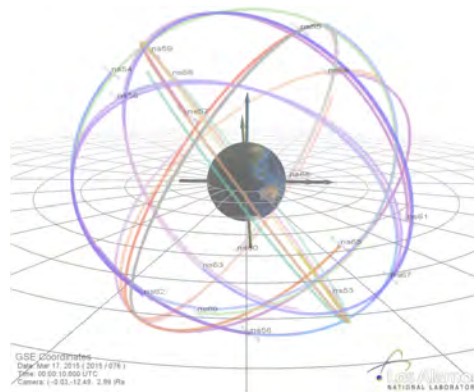


Figure 2: A visualization from Morley et al. (2016) of the spatial distribution of CXDequipped GPS satellites in geocentric solar ecliptic (GSE) coordinates. The satellite names mark their positions at midnight on 17 March 2015 with a colored trail showing their path over the previous 12 hours.

We focus on CXD as the primary data source for this project. CXD measures proton energies ranging from 6 MeV to  $>75$  MeV on five different channels. The data product includes differential omnidirectional fluxes, integral fluxes, count rates, geomagnetic parameters from several magnetic field models including L-shell, and more (Morley et al., 2016). Figure 3 shows a photo of the instrument with the Low Energy Particle (LEP) and High-energy X-ray and Particle (HXP) sensors labeled, the two detectors used for energetic electron and proton sensing.

Before studies utilizing the GPS proton data could be performed, the data needed to be proven reliable. Carver et al. (2018) presented a cross calibration of CXD with the Energetic Particle Sensor (EPS) onboard GOES. Figure 4 shows the log scaled integral flux measured by EPS versus the same measured by CXD for four different energy thresholds. The black dotted line represents where the data would follow if the two instruments were perfectly matched in what they measured. The green solid lines show the actual fit of the cross calibration. For proton energies  $>30$  MeV, CXD fluxes are within 20% of EPS. For proton energies  $>10$  MeV, CXD fluxes are within 40% of EPS. With this validation of the GPS proton data, GPS can be used reliably to study SEP events, geomagnetic shield-



Figure 3: Energetic Particle Sensors on CXD. LEP: Low Energy Particle subsystem has 5 electron channels. HXP: High-energy X-ray and Particle subsystem has 7 electron channels. Eleven electron channels on 19 block IIR and IIF satellites.

ing/access, and galactic cosmic rays. For this project, we focused on geomagnetic access during SEP events.

### 1.2. Solar Energetic Particle Events and Geomagnetic Cutoff

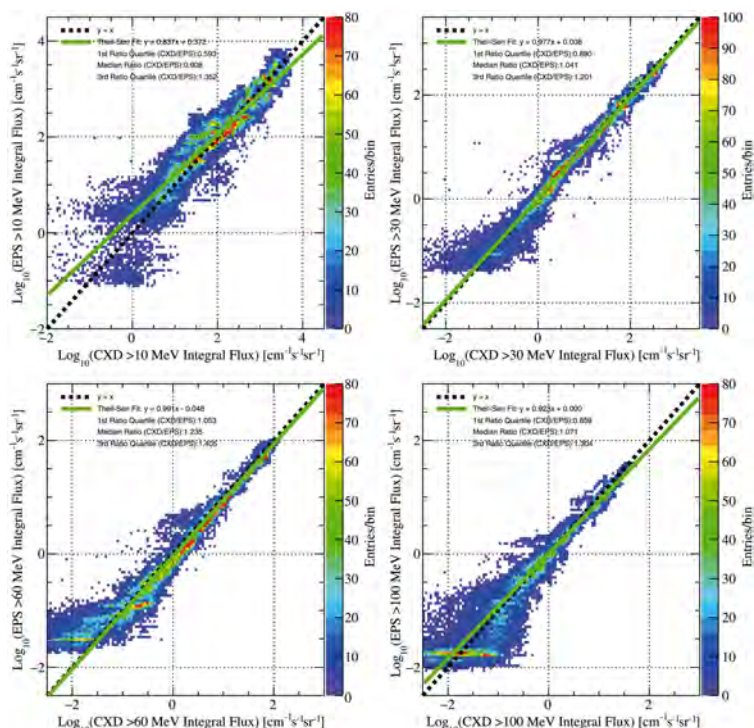


Figure 4: Plot from Carver et al. (2018) of GOES-11 and GOES-13 EPS versus GPS CXD integral proton fluxes >10 MeV (top left), >30 MeV (top right), >60 MeV (bottom left), and > 100 MeV (bottom right) protons. A  $y = x$  line (dotted black) represents perfect correlation, and a TheilSen line of best fit (solid green) shows the actual fit.

netic field, and allow the energetic protons to access lower latitudes than typical, increasing radiation exposure significantly compared to quiet conditions (Leske et al., 2001).

We call this latitude that the SEPs can reach the cutoff latitude. Depending on the energy and angle, particles cannot penetrate below their cutoff latitude. Suppression of the cutoff latitude has been observed by multiple missions during SEP events. We need to investigate different cutoff determination methods, as previous studies estimate the cutoff latitude from data from spacecraft with differences in pointing, incident angles, orbit altitude, and inclination than GPS. Essentially, the GPS CXD instrument is measuring a different population of the SEPs at different arrival angles.

Leske et al. (2001) estimated cutoff from data from the polar-orbiting Solar, Anomalous, and Magnetospheric Particle Explorer (SAMPEX) satellite during SEP events from 1992 to 1998. They found that cutoff latitude correlated well with both  $K_p$  and Dst, with cutoff latitude decreasing as storm activity increased, shown and discussed later in Figure 7. They measured typical suppression of the cutoff latitude between 5 and 10 degrees, with suppression as large as 15 degrees also measured. Rodger et al. (2006) also utilized SAMPEX, and determined the  $K_p$  dependent rigidity cutoff energies during a 4-10 November 2001 SEP event. Nesse Tyssøy et al. (2013) evaluated the cutoff latitude during a January 2012 SEP event using data from the POES 16-19 and METOP02 satellites. All of these studies saw a good correlation between geomagnetic activity and cutoff suppression.

Solar energetic particle (SEP) events are the most variable source of energetic protons in the near-Earth environment in time, energy, and flux, (compared to the more constant Galactic Cosmic Ray flux) and cause a variety of space weather effects (Carver et al., 2018). SEP events are caused when flares or coronal mass ejections accelerate particles to relativistic speeds, which travel along magnetic field lines. SEPs can arrive at the Earth from the Sun in an hour or less and may have damaging effects on spacecraft including ionizing and non-ionizing dose as well as single event effects.

The magnetosphere effectively shields low latitudes from most energetic protons. SEPs can access high latitudes in the magnetosphere and pose radiation dangers to high latitude aviation and high inclination LEO satellites. Most LEO spacecraft that do not traverse the polar region are not affected by the SEPs that access the magnetosphere, as the protons do not penetrate low enough. However, geomagnetic storms reconfigure the Earth's mag-

## 2. Methodology

Our approach to studying GPS measured cutoff latitude started with selecting SEP events in Section 2.1. Next, we determined the GPS measured cutoff with two definitions in Section 2.2. After, we compared to geomagnetic activity in Section 2.3 and previous spacecraft measurements in Section 2.4. Finally, we began a comparison to an analytic model in Section 2.5.

### 2.1. Selection of SEP events

The SEP intervals selected for this study are the same as used by Carver et al. (2018) to perform the GPS/GOES cross calibration. These four events provide a good variation in peak fluxes and temporal evolution. After the initial introduction here, each period will be referred to only by month and year. Each of the following descriptions follow those provided in Carver et al. (2018).

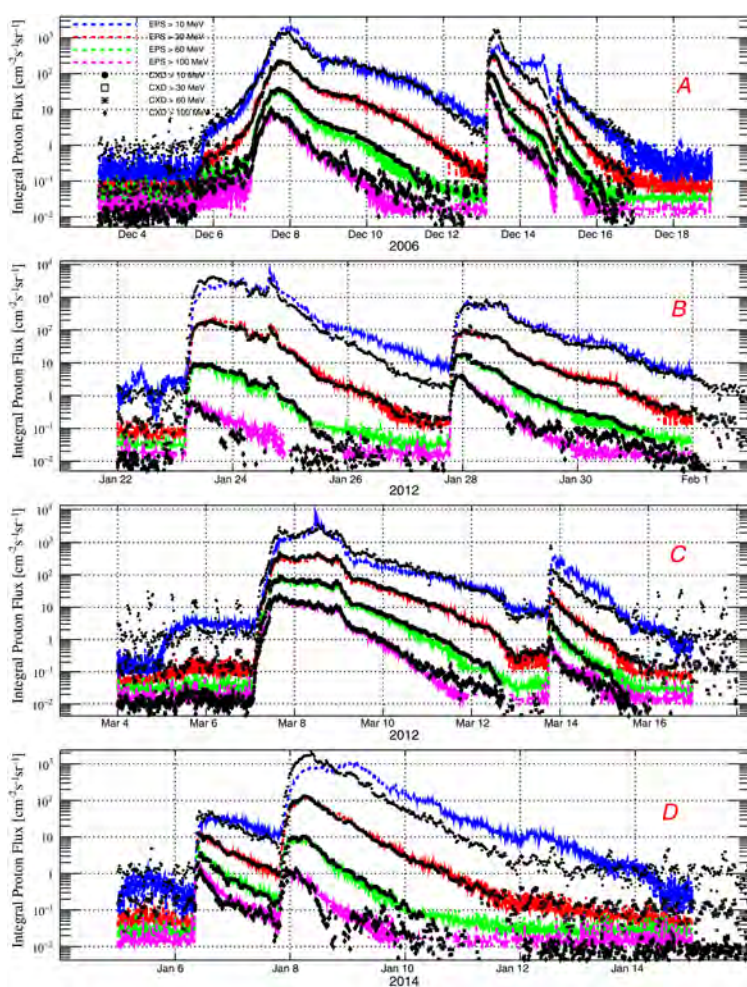


Figure 5: Integral proton flux versus time from Carver et al. (2018) for December 5-15, 2006 (a), January 22-31, 2012 (b), March 4-16, 2012 (c), and January 6-14, 2014 (d). GOES-11 and GOES-13 EPS 1 min average fluxes are shown as colored dotted lines for >10, >30, >60, and >100 MeV, while fluxes from all available CXD instruments are shown in black on 20 min averages.

below half the average flux above 70 degrees. Leske et al. (2001) used this method when determining the cutoff latitude from SAMPEX proton flux measurements. In Figure 6 from Leske et al. (2001), the 20-29 MeV proton counts per second measured by SAMPEX Proton/Electron Telescope (PET) are plotted versus latitude. We can see

The first SEP interval is December 5-15, 2006 (Figure 5A). This event has three intensifications, a gradual flux increase from an X-class flare followed by a prompt increase from a halo CME and an increase from a second halo. This event provides both variation in onset (gradual and prompt), as well as different acceleration mechanisms (flare and CMEs). 7 CXD instruments were operational to measure this event.

The second SEP interval is January 22-31, 2012 (Figure 5B). During this time, 2 SEP events occurred. A prompt onset from a CME is followed by a prompt onset from an X-class flare. This pair of SEPs disrupted commercial aviation and atmospheric composition. It was observed by 11 CXD instruments.

The third SEP interval is March 4-16, 2012 (Figure 5C). There was a minor enhancement which was not considered an SEP by NOAA's definition. This was followed by two rapid onset SEPs, and was measured by 11 CXD instruments.

The fourth SEP interval is January 6-14, 2014 (Figure 5D). The first SEP in this interval was small with a prompt onset, and the second SEP had a more gradual onset. This interval was measured by 13 CXD instruments.

### 2.2. Determine GPS measured cutoff

In data, cutoff latitude can be estimated as where the proton flux drops

a relatively constant count rate of about 800 counts per second from 70 degrees and above. The latitude where the count rate halves (400 counts per second) is approximately 65 degrees. Thus the cutoff latitude for this time period (1 Nov. 1992, 6:35-6:52) is 65 degrees by this determination method. After repeating this determination, a time series of cutoff latitudes is created, shown in Figure 7 from Leske et al. (2001) as the squared markers. The cutoff points are overlaid with the Dst (solid black line), showing the correlation between cutoff latitude suppression and geomagnetic activity.

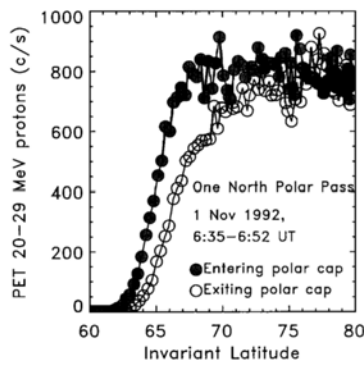


Figure 6: From Leske et al. (2001), the rate of  $\sim 20$ -29 MeV protons from SAMPEX PET measured every 6 seconds versus latitude for a single pass through the northern polar region.

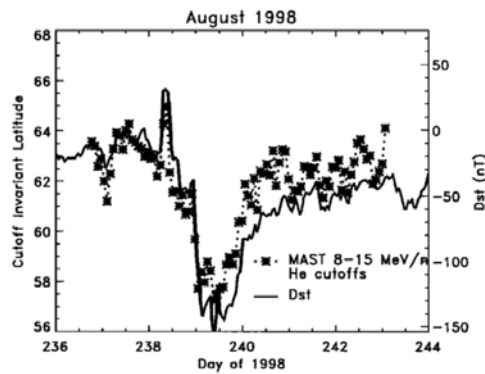


Figure 7: From Leske et al. (2001), the orbit averaged cutoff latitude (left scale, dotted) versus time compared to the geomagnetic activity index  $Dst$  (right scale, solid).

We started with this technique of defining cutoff as the location where flux is reduced by half from an average flux above some latitude. Figure 8 shows proton flux versus latitude for a single GPS satellite over a 6 hour period. We have a similar profile of constant flux above some latitude followed by a sharp decrease as the flux hits the cutoff. Note that the drop only appears more gradual than that in Figure 6 because we are now plotting differential flux on a log scale instead of linear. Instead of using the average above 70 degrees as our reference, we used 65 degrees since the GPS foot-point latitude is not often above 70 degrees. This determination method illustrated the capability to determine cutoff latitude from GPS measurements. We then investigated how to determine the cutoff L-shell.

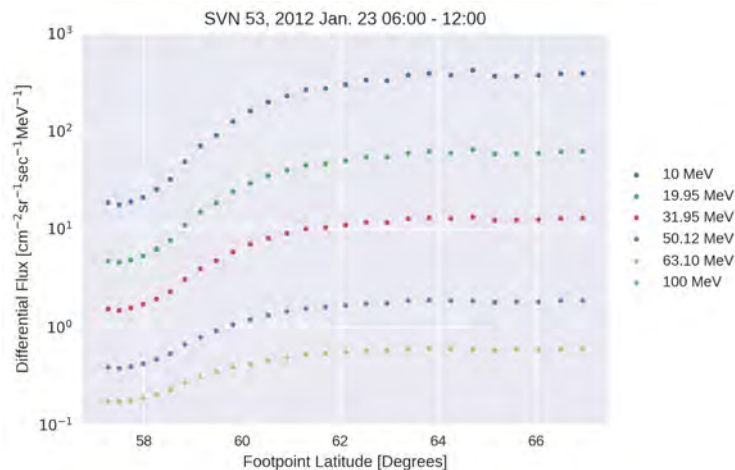


Figure 8: Log scaled differential flux for six proton energies vs. footpoint latitude from one GPS spacecraft (SVN 53) on Jan. 23rd from 06:00 - 12:00 UT.

To determine the geomagnetic cutoff L-shell from the GPS data, we binned all fluxes over 1 hour time periods and

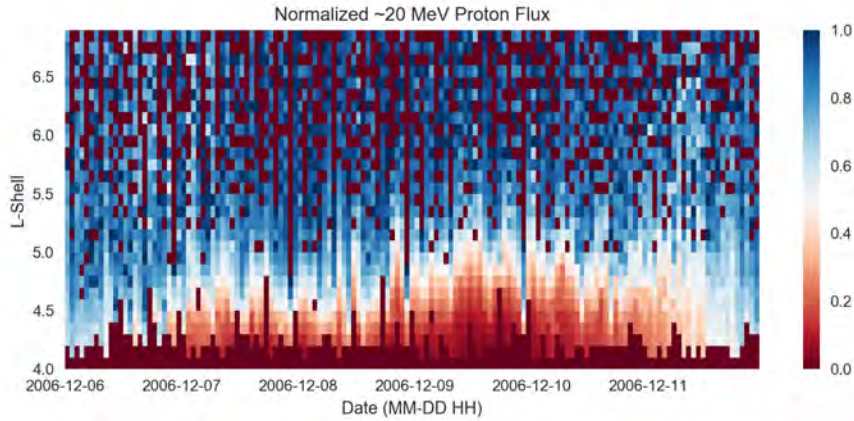


Figure 9: Dec. 2006 normalized proton flux plotted with respect to L-shell versus time. The cutoff is located along the white region separating the dominantly blue and red regions.

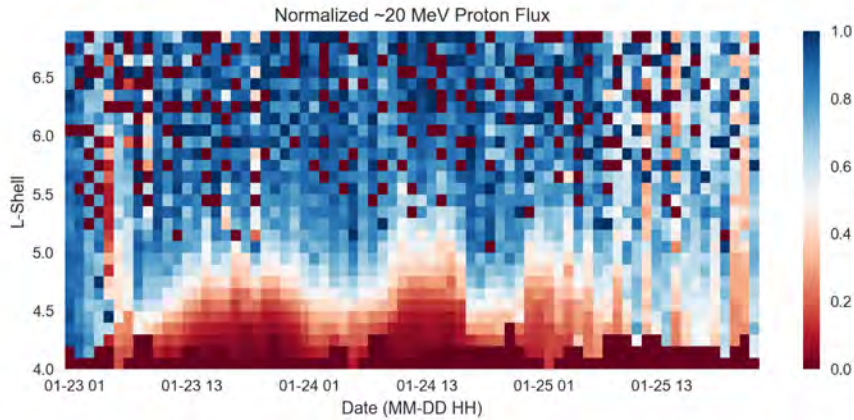


Figure 10: Jan. 2012 normalized proton flux plotted with respect to L-shell versus time. The cutoff is located along the white region separating the dominantly blue and red regions.

0.1 L-shell bins. For each time period, we normalized by the maximum flux in that bin so that values ranged from 0 (minimum flux) to 1 (maximum flux). Cutoff L-shell was then defined as the latitude where the normalized flux was closest to 0.5 (half of maximum flux). In Figures 9-12, we can see an evolution in the cutoff that changes with time. In Section 2.3, we compare the Jan. 2012 event to the  $K_p$  and Dst, two different geomagnetic storm indices. In Section 2.4, we compare the Jan. 2012 event with cutoff measured by Nesse Tyssøy et al. (2013) from NOAA/POES 16-19 and METOP02 data.

### 2.3. Compare to geomagnetic storm indices

We compare the GPS determined cutoff L-Shell to the Planetary K-index ( $K_p$ ) and the Disturbance Storm Time Index (Dst) to show the correlation between cutoff suppression and geomagnetic storms.  $K_p$  is a three hour index that characterizes geomagnetic activity from 0 to 9 with 0 being the lowest amount of activity and 9 being the highest. The  $K_p$  index is derived from ground-based magnetometer data. Dst is derived from near-equatorial geomagnetic observatories that measure the ring current.

As shown by Leske et al. (2001), the cutoff latitude is well correlated to the  $K_p$  index and the Dst index (Figure 7). For the Jan. 2012 event, Figures 13 and 14 show the GPS determined cutoff L-shell (blue) compared to the  $K_p$  index and the Dst index (red). Since  $K_p$  scales from 0 to 9 with increasing geomagnetic activity, it is plotted as



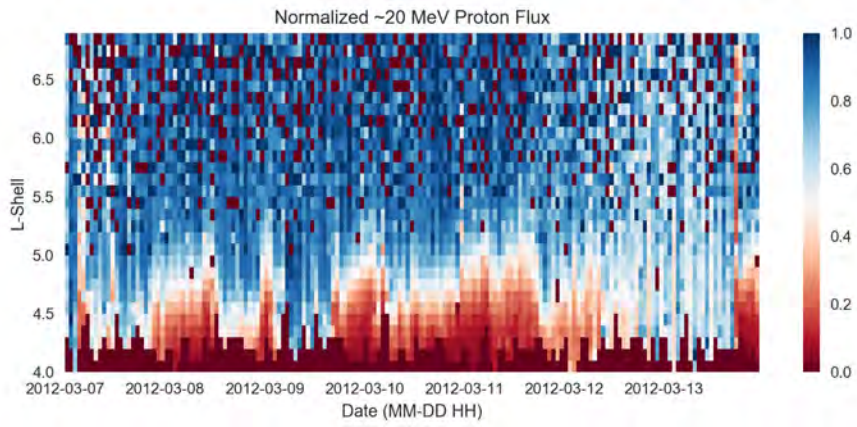


Figure 11: Mar. 2012 normalized proton flux plotted with respect to L-shell versus time. The cutoff is located along the white region separating the dominantly blue and red regions.

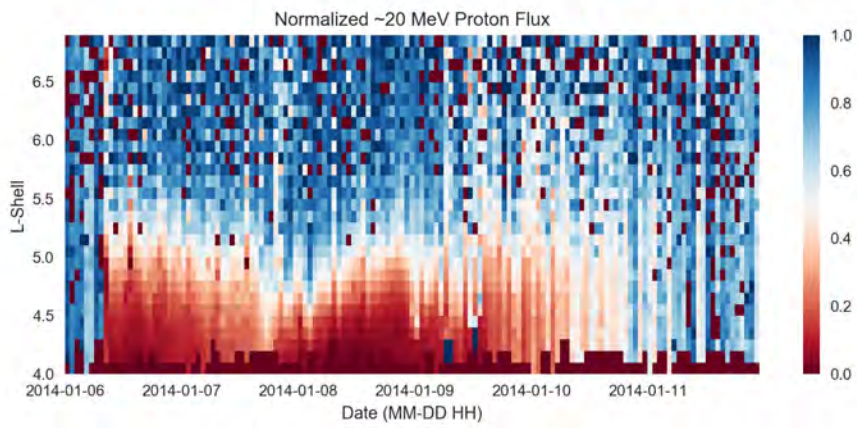


Figure 12: Jan. 2014 normalized proton flux plotted with respect to L-shell versus time. The cutoff is located along the white region separating the dominantly blue and red regions.

$(-1 \times K_p)$  to better show that the cutoff location decreases as  $K_p$  increases. Since the Dst decreases with increasing geomagnetic activity, we did not have to adjust this scale.

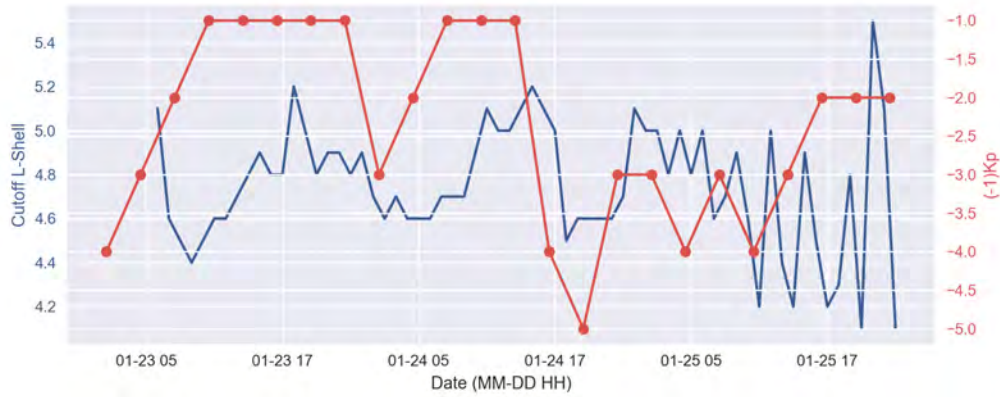


Figure 13: For the Jan. 2012 SEP event: cutoff L-shell in blue on the left axis;  $(-1 \times K_p)$  in red on the right axis.

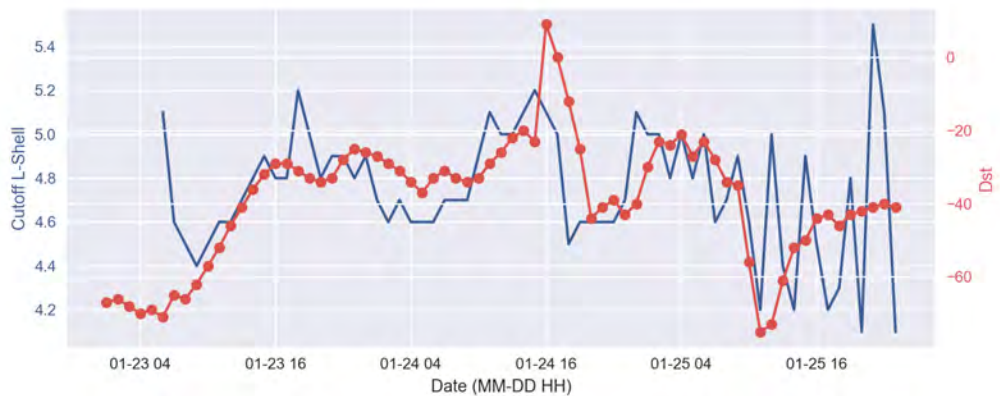


Figure 14: For the Jan. 2012 SEP event: cutoff L-shell in blue on the left axis; Dst in red on the right axis.

#### 2.4. Compare to other spacecraft measurements

We qualitatively compare our temporal cutoff evolution for the part January 2014 SEP interval (23rd-26th) with cutoff calculation from the same period determined from NOAA/POES 16-19 and METOP02 data by [Nesse Tyssøy et al. \(2013\)](#). In Figure 15, we see the GPS cutoff L-shell on the top plot and the POES/METOP02 cutoff latitude on the bottom plot. Boxed in pink on both plots, we see an initial rise and suppression of the cutoff from the 23rd-24th of the month. Next, in the orange boxes, we see a sharper increase and decrease in cutoff location on the 24th. In the yellow box, we see another increase followed by the sharpest cutoff suppression occurring on the 25th. Finally, in the green boxes, we see the cutoff position recovering after the intense geomagnetic suppression. The GPS measured cutoff correlation with the cutoff determined by [Nesse Tyssøy et al. \(2013\)](#) provides an initial validation our cutoff determination method.

#### 2.5. Compare to models

The first geomagnetic cutoff model we assess is the pure dipole field the cutoff rigidity (momentum per charge of a particle), expressed analytically as:

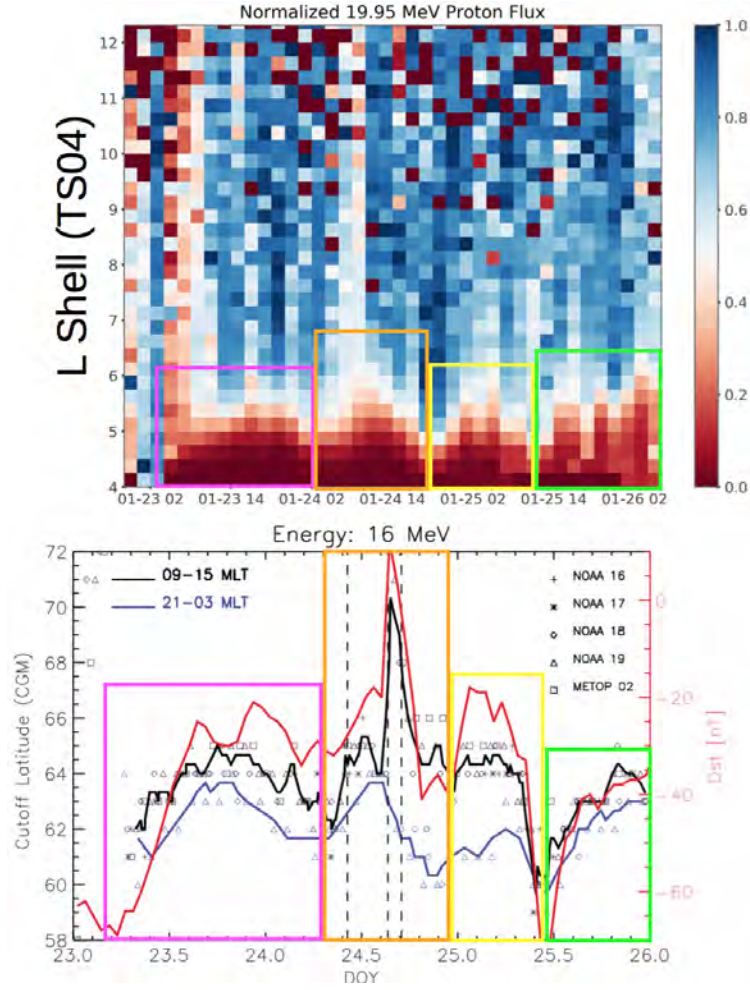


Figure 15: Correlation between GPS determined cutoff (top) and cutoff determined by Nesse Tysøy et al. (2013) from NOAA/POES 16–19 and METOP02 data (bottom). Matching colored boxes highlight matching trends in the cutoff evolution through time for both plots.

$$R_s = C_{St} \frac{1}{L^2} \frac{1}{(1 + \sqrt{1 + \cos \alpha \cos \lambda^3})^2} \quad (1)$$

where  $L = r \cos^2 \lambda$  is the dipole L-shell,  $\lambda$  is the magnetic latitude,  $\alpha$  is the angle between the particle arrival direction and magnetic west, and  $C_{St} = 60$  is a constant containing the dipole moment ( $8.06 \times 10^{25}$  Gauss cm<sup>3</sup>) and the conversion factors necessary to express  $R_s$  in units of GV (Störmer, 1955; Kress et al., 2015).  $R_s$  is plotted versus latitude and L-shell in Figures 16 and 17 for  $\alpha = 0$  and  $\alpha = \pi$  to show the minimum and maximum boundaries. As we decrease in latitude or L-shell, we see an increase in rigidity. Particles need higher rigidities to access lower latitudes.

Cutoff rigidity as the minimum rigidity a particle must possess to penetrate to a given geomagnetic latitude. Each cutoff latitude has a corresponding cutoff rigidity. Rigidity is a property of a particle defined as the momentum per unit charge. To compare this model of cutoff rigidity to our data, we obtained rigidity to energy conversions for protons from [https://ccmc.gsfc.nasa.gov/pub/modelweb/cosmic\\_rays/cutoff\\_rigidity\\_sw/rpt-6.doc](https://ccmc.gsfc.nasa.gov/pub/modelweb/cosmic_rays/cutoff_rigidity_sw/rpt-6.doc). This is an implementation of the Smart and Shea rigidity to energy conversion. In Figure 18, we show the cutoff L-shell as a function of proton energy. We see that cutoff latitude decreases as proton energy increases.

Figure 18 also compares the cutoff L-shells we computed for the different energy channels to this model. The yellow points are the mean cutoff L-shell for the Jan. 2012 period at 10 MeV, 19.95 MeV, 31.62 MeV, 50.12 MeV,

and 63.10 MeV. There is a slight decrease in cutoff L-Shell with increasing energy, but it is not well matched to the analytic model. This model makes several simplifications that account for some of the differences from the GPS determined cutoff. Most importantly, it assumes a simple dipole magnetic field and it does not include the effects of geomagnetic activity. We discuss models for future comparison in Section 3.

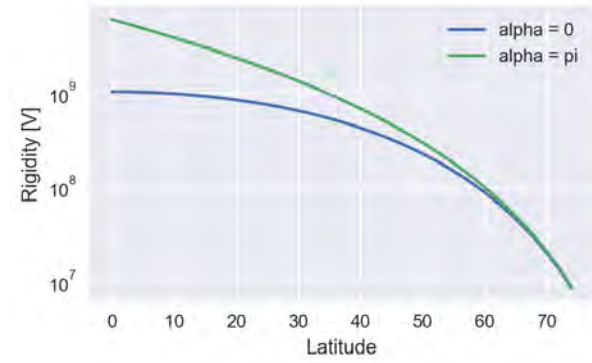


Figure 16: Modeled rigidity vs. cutoff latitude for  $\alpha = 0$  (blue) and  $\alpha = \pi$  (green), where  $\alpha$  is the angle between the particle arrival direction and magnetic west.

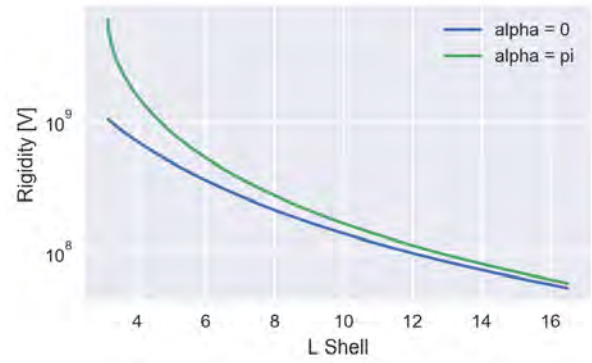


Figure 17: Modeled rigidity vs. cutoff L-shell for  $\alpha = 0$  (blue) and  $\alpha = \pi$  (green), where  $\alpha$  is the angle between the particle arrival direction and magnetic west.

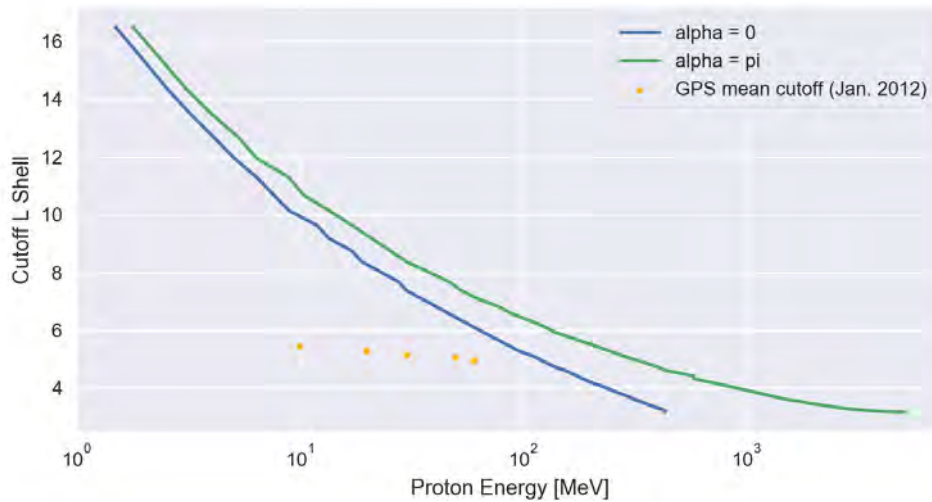


Figure 18: Modeled cutoff L-shell vs. proton energy for  $\alpha = 0$  (blue) and  $\alpha = \pi$  (green), where  $\alpha$  is the angle between the particle arrival direction and magnetic west. The mean cutoff L-Shell for the Jan. 2012 SEP event is shown in yellow for proton energies of 10 MeV, 19.95 MeV, 31.62 MeV, 50.12 MeV, and 63.10 MeV.

### 3. Conclusions & Future Work

The availability of the GPS particle detector data presents many opportunities for exploring physical phenomena of the geospace environment with better spatial distribution and longer temporal coverage than any previous science missions have achieved. In this report, we presented a first investigation into the ability of GPS proton measurements to be utilized to determine geomagnetic cutoff. We successfully determined cutoff L-shell locations during four SEP events. For the January 2012 event, we showed the correlation between cutoff suppression and geomagnetic activity

and performed a preliminary comparison to an analytic cutoff model. The next step in this project will be to utilize particle tracing codes to obtain an empirical model of cutoff with a more realistic field model.

## References

- Carver, M.R., Sullivan, J.P., Morley, S.K., Rodriguez, J.V., 2018. Cross calibration of the gps constellation cxd proton data with goes eps. *Space Weather* 16, 273–288. <https://agupubs.onlinelibrary.wiley.com/doi/pdf/10.1002/2017SW001750>.
- Knipp, D.J., Giles, B.L., 2016. Global positioning system energetic particle data: The next space weather data revolution. *Space Weather* 14, 526–527. <https://agupubs.onlinelibrary.wiley.com/doi/pdf/10.1002/2016SW001483>.
- Kress, B.T., Hudson, M.K., Selesnick, R.S., Mertens, C.J., Engel, M., 2015. Modeling geomagnetic cutoffs for space weather applications. *Journal of Geophysical Research: Space Physics* 120, 5694–5702. <https://agupubs.onlinelibrary.wiley.com/doi/pdf/10.1002/2014JA020899>.
- Leske, R.A., Mewaldt, R.A., Stone, E.C., 2001. Observations of geomagnetic cutoff variations during solar energetic particle events and implications for the radiation environment at the space station. *Journal of Geophysical Research: Space Physics* 106, 30011–30022. <https://agupubs.onlinelibrary.wiley.com/doi/pdf/10.1029/2000JA000212>.
- Morley, S.K., Sullivan, J.P., Carver, M.R., Kippen, R.M., Friedel, R.H.W., Reeves, G.D., Henderson, M.G., 2017. Energetic particle data from the global positioning system constellation. *Space Weather* 15, 283–289. <https://agupubs.onlinelibrary.wiley.com/doi/pdf/10.1002/2017SW001604>.
- Morley, S.K., Sullivan, J.P., Henderson, M.G., Blake, J.B., Baker, D.N., 2016. The global positioning system constellation as a space weather monitor: Comparison of electron measurements with van allen probes data. *Space Weather* 14, 76–92. <https://agupubs.onlinelibrary.wiley.com/doi/pdf/10.1002/2015SW001339>.
- Nesse Tyssøy, H., Stadsnes, J., Søråas, F., Sørbø, M., 2013. Variations in cutoff latitude during the january 2012 solar proton event and implication for the distribution of particle energy deposition. *Geophysical Research Letters* 40, 4149–4153.
- Rodger, C.J., Clilverd, M.A., Verronen, P.T., Ulich, T., Jarvis, M.J., Turunen, E., 2006. Dynamic geomagnetic rigidity cutoff variations during a solar proton event. *Journal of Geophysical Research: Space Physics* 111.
- Störmer, C., 1955. *The polar aurora*. Clarendon Press.



# Using High-Resolution 3D Hybrid Simulations to Investigate Plasma Turbulence at Ion-kinetic Scales

Lloyd D. Woodham<sup>a</sup>, Xiangrong Fu<sup>b</sup>, Misa M. Cowee<sup>c</sup>, Daniel Verscharen<sup>a,d</sup>, Robert T. Wicks<sup>a,e</sup>, S. Peter Gary<sup>c,f</sup>, Dan Winske<sup>c</sup>

<sup>a</sup>*Mullard Space Science Laboratory, University College London, Holmbury St. Mary, Dorking, Surrey, UK*

<sup>b</sup>*New Mexico Consortium, Los Alamos, NM, USA*

<sup>c</sup>*Los Alamos National Laboratory, Los Alamos, NM, USA*

<sup>d</sup>*Space Science Center, University of New Hampshire, NH, USA*

<sup>e</sup>*Institute of Risk and Disaster Reduction, University College London, Gower Street, London, UK*

<sup>f</sup>*Space Science Institute, Boulder, CO, USA*

---

## Abstract

The solar wind provides insights into the fundamental kinetic processes that occur in collisionless plasmas. One of the outstanding problems is how turbulent fluctuations dissipate into heat at small scales. At ion-kinetic scales, these fluctuations exhibit characteristics that are consistent with the properties of linear plasma waves such as polarisation, frequency and wavenumber, making wave-particle interactions viable dissipation mechanisms in the place of collisions. However, directly observing these heating processes is difficult due to the nature of in-situ spacecraft data. Conversely, present-day computational resources allow for three-dimensional high-resolution hybrid plasma simulations that can help us to understand turbulent dissipation without the restriction of single-point measurements. We analyse data from a 3D hybrid simulation to show that a coherent signature in the magnetic helicity spectrum associated with circularly-polarised fluctuations is associated with a steepening in the power spectrum of magnetic field fluctuations at scales  $kd_i \sim 1$ , as found by Woodham et al. (2018) using in-situ solar wind data. These results are consistent with wave-particle interactions between the ions and the wave-like fluctuations at these scales. Further work is ongoing to characterise the nature of these fluctuations and their importance regarding heating of the plasma.

*Keywords:* plasma, turbulence, hybrid simulations, dissipation, waves, kinetic physics

---

## 1. Introduction

Collisionless astrophysical plasmas are ubiquitous across the Universe. An example is the solar wind, a supersonic and super-Alfvénic outflow of plasma from the solar corona. The plasma flow carries with it the interplanetary magnetic field which permeates the entire heliosphere. The bulk properties of the solar wind are highly variable, with large changes in speed that form a bimodal distribution leading to the classification of two types of flow: highly variable slow wind at about 300 km/s, and less variable fast wind at about 600 km/s. While fast wind is typically associated with the outflow from coronal holes, the origins of the slow wind are still poorly understood, although slow wind streams often originate from areas of the Sun associated with active regions (Schwenn, 1990; Habbal et al., 1997).

Both the plasma moments (such as the density and velocity) and electromagnetic fields show fluctuations over a wide range of scales - at the largest scales, the magnetic field is frozen-in to the plasma, and together they act like a magnetofluid. This fluid exhibits turbulent fluctuations, driving a continual cascade of energy from large scales ( $\sim 10^6$  km) towards smaller scales of the order of the electron gyroradius ( $\sim 10^1$  km) (Goldstein et al., 1995; Tu and Marsch, 1995; Bruno and Carbone, 2013). The plasma can no longer behave as a fluid at scales of the order of the proton inertial length or gyroradius ( $\sim 10^2$  km) or smaller. At these so-called ion-kinetic scales, the plasma and

---

*Email address:* lloyd.woodham.16@ucl.ac.uk (Lloyd D. Woodham)

electromagnetic field fluctuations can interact directly with the proton velocity distribution, and the kinetic motions of plasma begin to dominate leading to the dissipation of energy from the fluctuations, heating the particles directly (Kiyani et al., 2015; Chen, 2016). At the same time, kinetic effects can lead to the generation of waves and instabilities that can extract free energy from the particle velocity distribution functions (Alexandrova et al., 2013).

This interplay of the continuous flow of energy between the particles and fields is made even more complicated by the relative lack of collisions in the solar wind. Turbulence in a neutral fluid dissipates via collisions, whereas in the solar wind the collision rate is low. At the same time, we observe heating of the solar wind plasma (Cranmer et al., 2009) such that it no longer follows the radial profile as described by adiabatic expansion (cooling) (Marsch et al., 1982; Richardson et al., 1995). The fluctuations at ion-kinetic scales exhibit specific characteristics that are consistent with the polarisation properties of linear plasma waves (Gary, 1986), making wave-particle interactions viable dissipation mechanisms in the place of collisions (Marsch, 2006, 2012). Understanding these physical processes is essential for our understanding of how energy and momentum flow in collisionless astrophysical plasmas.

In-situ spacecraft provide measurements of the solar wind plasma moments and electromagnetic fields - the fluctuations of these variables exhibit power laws over several decades in frequency. At frequencies,  $f < 0.1$  Hz, magnetohydrodynamic (MHD) theory adequately describes the turbulent fluctuations, which are predominantly Alfvénic, where the magnetic field fluctuations show a characteristic Kolmogorov spectrum of  $f^{-5/3}$  (Bruno and Carbone, 2013). That is, both the magnetic field and bulk velocity fluctuations are dominantly in the perpendicular components with respect to the background magnetic field and often (anti-)correlate with each other:  $\mathbf{b} = \pm \mathbf{u}$ , where  $\mathbf{u}$  represents the bulk velocity fluctuations,  $\mathbf{b} = \mathbf{B} \sqrt{4\pi\rho}$  is the fluctuating magnetic field in Alfvén (velocity) units, and  $\rho$  is the plasma density. This part of the spectrum with an exponent of  $-5/3$  is often termed the inertial range. Close to wavelengths of the order of proton kinetic scales, observed between 0.1-1 Hz in the spacecraft frame, the spectrum steepens and is more variable, with a spectral exponent between  $-2$  and  $-4$  that stabilises to around  $f^{-2.8}$  towards electron kinetic scales (Smith et al., 2006; Hamilton et al., 2008; Koval and Szabo, 2013; Bruno and Trenchi, 2014).

The fluctuating magnetic helicity, which describes the handedness of fluctuations at a particular frequency, is another useful parameter that can reveal information about the nature of the turbulent cascade (Matthaeus and Goldstein, 1982; Matthaeus et al., 1982). Throughout the inertial range, the helicity fluctuates almost randomly about zero (Matthaeus and Goldstein, 1982). At ion-kinetic scales a coherent signature appears, indicating the presence of circularly polarised fluctuations. Recent studies have used wavelet techniques to investigate this signature further, finding evidence of the presence of both left-handed parallel propagating Alfvén ion-cyclotron (AIC) waves and right-handed oblique kinetic Alfvén waves (KAWs) (Goldstein et al., 1994; Leamon et al., 1998; Podesta and Gary, 2011; He et al., 2011, 2012a,b; Bruno and Telsoni, 2015; Telsoni et al., 2015). These features are consistent with linear theory where the dispersion relation of Alfvén waves splits into two branches: one for AIC waves and the other for KAWs, depending on plasma properties and the direction of propagating with respect to the background magnetic field (Gary, 1986).

Observations of solar wind turbulence suggest that the power in the cascade is in wavevectors primarily perpendicular to the background magnetic field,  $k_{\perp} \gg k_{\parallel}$ , and that at kinetic scales the Alfvén wave cascade is replaced by KAWs (Horbury et al., 2008; Chen et al., 2010a,b; Wicks et al., 2010). The source of AIC waves is still under debate - the growth of waves due to plasma instabilities often explains their presence (e.g. Jian et al., 2009; Gary, 2015; Wicks et al., 2016). The break in the power spectrum at ion-kinetic scales has been interpreted as the onset of dissipation of the fluctuations, leading to heating of solar wind ions (Leamon et al., 1998; Galtier, 2006; Schekochihin et al., 2009). Numerous studies have focussed on identifying the physical mechanisms behind the break scales, although actual evidence of dissipation leading to heating has not been observed. However, Woodham et al. (2018) recently linked the spectral break to the presence of fluctuations with the properties of linear Alfvén waves at these scales.

The solar wind is an excellent laboratory to provide unique insights into the fundamental kinetic processes in collisionless plasmas because spacecraft are small enough not to affect the local properties of the plasma at these scales. A deeper understanding of the ongoing kinetic processes in the solar wind will provide insights into problems such as coronal heating and solar wind acceleration, as well as improved knowledge of the macroscopic properties of the solar wind. However, the complexity of these data can make it challenging to link phenomena with theory, mainly because the standard magnetohydrodynamic or kinetic equations that describe the plasma dynamics cannot be solved analytically. Many different physical phenomena occur over different time and spatial scales, often making it difficult to separate various processes. Various techniques have been developed or utilised to analyse in-situ data which are very powerful, e.g. spectral analysis. Plasma simulations also play a vital role in aiding our understanding of space



plasma dynamics, helping us verify analytical and empirical models of phenomena, or explain physical processes that we observe in space, particularly non-linear processes where analytical solutions are sparse.

Hybrid simulations treat ions kinetically and electrons as a fluid, and have been used extensively to explore plasma turbulence and heating at kinetic scales (e.g., Parashar et al., 2009, 2010, 2011; Valentini et al., 2010; Servidio et al., 2012; Verscharen et al., 2012; Vasquez et al., 2014; Hellinger et al., 2015; Servidio et al., 2015; Vasquez, 2015; Franci et al., 2015a,b, 2016, 2017, 2018; Cerri et al., 2016, 2017a,b, 2018; Cerri and Califano, 2017). These simulations retain all the relevant ion kinetic physics but do not include electron kinetic physics, making them less computationally expensive than fully kinetic particle-in-cell (PIC) codes. This quality is particularly useful when investigating turbulent phenomena that occur over a wide range of scales since a large simulation domain is needed to generate a cascade that is comparable to in-situ data from the solar wind.

In this report, we document research using hybrid plasma simulations to complement in-situ solar wind data analysis to probe the properties of the turbulence at ion-kinetic scales. We aim to understand the dissipation of the turbulent fluctuations and resultant heating of the plasma. In subsequent sections, we discuss the properties of Alfvénic turbulence, the hybrid simulations we use, analysis of simulation data, our simulation setup, and finally the results with a discussion on our interpretations.

## 2. Alfvénic Turbulence

Turbulence is a dynamical phenomenon observed in fluids and plasmas where the bulk parameters of the fluid show irregular fluctuations that appear almost stochastic but are chaotic. They non-linearly couple to create a cascade of energy to smaller scales, making turbulence a multi-fractal process. While turbulence appears to be stochastic, it is, in fact, deterministic - its chaotic nature makes it difficult to predict the precise properties of turbulent flow such as the velocity and pressure; instead, we use statistics to investigate the average properties. These properties are not sensitive to initial conditions or disturbances, and the deterministic nature of turbulence produces correlations that we can measure (Frisch, 1995; Biskamp, 2003).

In a plasma, turbulence is more complex than its neutral fluid counterpart due to the importance of magnetic fields in plasma dynamics that introduces anisotropy. At frequencies below the ion gyrofrequency,  $\Omega_i$ , the MHD approximation holds. In incompressible MHD, two coupled equations describe a plasma (Bruno and Carbone, 2013):

$$\frac{\partial \mathbf{u}}{\partial t} + (\mathbf{u} \cdot \nabla) \mathbf{u} = -\frac{\nabla p}{\rho} + \nu \nabla^2 \mathbf{u} + (\mathbf{b} \cdot \nabla) \mathbf{b}, \quad (1)$$

$$\frac{\partial \mathbf{b}}{\partial t} + (\mathbf{u} \cdot \nabla) \mathbf{b} = -(\mathbf{b} \cdot \nabla) \mathbf{u} + \eta \nabla^2 \mathbf{b}, \quad (2)$$

where  $p$  is the total plasma pressure (the sum of the magnetic and thermal pressure),  $\rho$  is the plasma density,  $\nu$  is the kinematic viscosity, and  $\eta$  is the magnetic diffusivity. The first equation is just a modified version of the Navier-Stokes equation including the magnetic field. The system is completed with  $\nabla \cdot \mathbf{u} = 0$  and  $\nabla \cdot \mathbf{b} = 0$ . Equations 1-2 contain four non-linear terms in  $\mathbf{b}$  and  $\mathbf{u}$ , and their cross-terms, as well two diffusion terms given by  $\nu \nabla^2 \mathbf{u}$  and  $\eta \nabla^2 \mathbf{b}$ . When the non-linear terms dominate over the diffusion terms, dissipation cannot occur and instead non-linear interactions dominate, leading to a turbulent cascade. To quantify this effect we use the Reynold's number,  $\text{Re}$ , and the magnetic Reynold's number,  $\text{R}_m$ :

$$\text{Re} = UL/\nu, \quad (3)$$

$$\text{R}_m = v_A L/\eta, \quad (4)$$

where  $U$  is the characteristic velocity scale,  $L$  is the characteristic length scale, and  $v_A$  is the Alfvén speed:  $v_A = \frac{B_0}{\sqrt{4\pi\rho}}$ , where  $B_0$  is the mean background field. These represent a measure of the relative strength between the non-linear terms and the dissipative terms. The higher the Reynold's number, the more turbulent a flow. In astrophysical plasmas such as the solar wind, often  $\text{R}_m > \text{Re}$ , leading to a dominance in magnetic field fluctuations over velocity

fluctuations, although this is not always the case (see for example, Roberts, 2010). Neglecting dissipative terms, the MHD equations conserve three quantities: the total energy,  $\langle u^2 + b^2 \rangle$ , the cross-helicity,  $\langle \mathbf{u} \cdot \mathbf{b} \rangle$ , and the magnetic helicity,  $\langle \mathbf{a} \cdot \mathbf{b} \rangle$ . Here lowercase letters represent the fluctuations in the fields (e.g.,  $\mathbf{B} = \mathbf{B}_0 + \mathbf{b}$ ),  $\mathbf{a}$  is the fluctuating magnetic vector potential,  $\mathbf{b} = \nabla \times \mathbf{a}$ , and angular brackets indicate an ensemble average.

A useful notation to make Equations 1-2 more symmetrical is to use Elsässer variables:  $\mathbf{z}^\pm = \mathbf{u} \pm \mathbf{b}$  (Elsässer, 1950). The equations then become  $\nabla \cdot \mathbf{z}^\pm = 0$  and

$$\frac{\partial \mathbf{z}^\pm}{\partial t} \mp (\mathbf{v}_A \cdot \nabla) \mathbf{z}^\pm + (\mathbf{z}^\mp \cdot \nabla) \mathbf{z}^\pm = -\frac{\nabla p}{\rho} + \nu \nabla^2 \mathbf{z}^\pm + \mathbf{F}^\pm, \quad (5)$$

where the dissipative coefficients are  $2\nu^\pm = \nu \pm \eta$  and  $\mathbf{F}^\pm$  represents external forcing terms. If we linearise the equation and neglect dissipative terms,

$$\frac{\partial \mathbf{z}^\pm}{\partial t} \mp (\mathbf{v}_A \cdot \nabla) \mathbf{z}^\pm \simeq 0, \quad (6)$$

which represents Alfvén waves propagating parallel and anti-parallel to the background magnetic field,  $\mathbf{B}_0$ . Hence, the non-linear interaction term involves counter-propagating Alfvén waves. This interaction leads to shearing and decay of the Alfvén waves into multiple daughter waves with smaller wavelengths, which are more inclined perpendicular to the magnetic field. Hence, as the cascade progresses to smaller scales, the turbulence becomes more anisotropic, i.e.,  $k_\perp \gg k_\parallel$ . More details on the phenomenology of Alfvénic turbulence can be found in Biskamp (2003) and Bruno and Carbone (2013).

### 3. Hybrid Simulations

Hybrid simulations combine the use of PIC methods and fluid equations. We treat ions kinetically and the electrons as a neutralising massless fluid, allowing us to explore ion-kinetic effects at small scales while still capturing low-frequency electromagnetic phenomena. By treating electrons as a fluid we are unable to resolve electron kinetic processes, i.e., ones on scales of the electron gyroradius,  $\rho_e$ , or frequencies comparable to the electron gyrofrequency,  $\Omega_e$ . However, the advantages of doing this mean the code will run faster than a fully kinetic code, allowing larger simulation boxes and more data. The relevant scales and frequencies of interest are the ion gyroradius,  $\rho_i$ , ion inertial length,  $d_i$  and ion gyrofrequency,  $\Omega_i$ . These characteristic lengths and timescales are relatively easily measured in space plasma by instrumentation since they are of the order of 10-100 km and seconds, respectively. With current computational resources, we can use a large-scale three-dimensional simulation domain ( $\sim 10^2 d_i$  in each dimension) with high resolution ( $\sim 10^{-1} d_i$ ), making hybrid simulations an ideal method for exploring turbulent phenomena in collisionless plasmas. For comparison, high-resolution 3D PIC simulations typically only have a simulation domain of  $\sim 10^1 d_i$  and so, struggle to capture large-scale effects.

Plasma phenomena require a description of the electromagnetic fields and the particles that make up the plasma, ions and electrons. Therefore, for hybrid simulations we use Maxwell's equations in the low frequency approximation (the displacement current is neglected):

$$\nabla \times \mathbf{B} = \frac{4\pi}{c} \mathbf{J} \quad (7)$$

$$\nabla \times \mathbf{E} = -\frac{1}{c} \frac{\partial \mathbf{B}}{\partial t}, \quad (8)$$

supplemented by the divergenceless condition:  $\nabla \cdot \mathbf{B} = 0$ . We use the equation for momentum conservation to describe the electron fluid in the limit of zero mass:

$$n_e m_e \frac{d\mathbf{V}_e}{dt} = -en_e \left( \mathbf{E} + \frac{\mathbf{v}_e \times \mathbf{B}}{c} \right) - \nabla \cdot \mathbf{P}_e + en_e \mathbf{R} \cdot \mathbf{J} = 0, \quad (9)$$

where  $\mathbf{V}_e$  is the bulk electron velocity and the finite electron temperature is included within the electron pressure

tensor  $\mathbf{P}_e = n_e T_e \mathbf{1}$ , which we assume is isotropic for simplicity. The final term in Equation 9 includes the resistivity tensor,  $\mathbf{R}$ , and represents the collisional drag (resistive coupling) between ions and electrons. Again for simplicity, we take a scalar resistivity:  $\mathbf{R} = \eta \mathbf{1}$ . To close the system of equations for electrons we assume an equation of state (see Equation 26) and assume quasi-neutrality between species:  $en_e = q_i n_i$ .

To treat the ions kinetically we use the following equations for individual particles:

$$\frac{d\mathbf{x}_i}{dt} = \mathbf{v}_i, \quad (10)$$

$$m_i \frac{d\mathbf{v}_i}{dt} = q_i \left( \mathbf{E} + \frac{\mathbf{v}_i \times \mathbf{B}}{c} \right) - q_i \eta \mathbf{J}, \quad (11)$$

where the subscript  $i$  indicates the ion species and  $\mathbf{J} = q_i n_i (\mathbf{V}_i - \mathbf{V}_e)$  is the total current density due to both ions and electrons. The final term in the second equation balances the corresponding term in Equation 9. The quasineutrality condition implies that  $\nabla \cdot \mathbf{E} = 0$  and the divergenceless condition is maintained when Equation 8 is evolved.

### 3.1. Numerical Set-up

To implement these equations numerically, we need to discretise them both in space and time and normalise them to dimensionless units. Hybrid codes are most useful for ion-kinetic effects at time scale  $\geq \Omega_i^{-1}$  and spatial scales  $\geq d_i = c/\omega_i$  or  $\rho_i$ , respectively. Several ion species, denoted by subscript  $s$ , each with its own initial density  $n_s(\mathbf{x})$ , mass  $m_s$ , charge  $q_s$ , and velocity distribution  $F_s(\mathbf{v})$ , can be included in the code. There is also a background magnetic field,  $\mathbf{B}_0(\mathbf{x})$ , which can have an arbitrary direction. These parameters can be used to derive the ion gyrofrequency  $\Omega_i = q_0 B_0 / m_0 c$ , and ion plasma frequency  $\omega_i^2 = 4\pi q_0^2 n_0 / m_0$ , where  $n_0$  is the ion density,  $q_0$  is the charge of a proton and  $m_0$  is the mass of a proton. The density  $n_0$  can be defined in several ways. Usually, if there is a dominant ion species throughout the simulation box,  $n_0$  is defined as the density of this species, usually as the average over the box. Then, the other ion species can be given different fractional values. Alternatively,  $n_0$  is defined as the total ion density,  $\sum_s q_s n_s$ , and fractions are assigned to all the different ion species. Taking the speed of light,  $c$ , as the units of velocity we can then describe spatial scales in terms of  $d_i = c/\omega_i$  and for temporal scales,  $\omega_i^{-1}$ . In these units, the electromagnetic fields are normalised such that there are no constants in Maxwell's equations.

To discretise in space we use a spatial grid with a length,  $L$ , in each dimension, often as a multiple of  $d_i$ , e.g.  $0 \leq x \leq L_x$ . The spatial dimensions can be varied from one to three; however, all three velocity and field components are retained. We will refer to a 1D grid here for simplicity. The grid is subdivided into  $N_x$  cells with equal length  $\delta x = L_x / N_x$ . The size of the domain is dependent on the physical constraints of the problem being investigated, and the cell size depends on the resolution required to study the problem. For turbulence, the domain needs to be large enough to support an inertial range power law over at least an order of magnitude, while the cell size is usually a fraction of  $d_i$  to be able to resolve the spectral break due to kinetic effects. Typically  $\delta x \geq 0.1 d_i$ , since massless electrons eliminates  $d_e = c/\omega_e$  scales. Simulations typically use 16-1024 particles per cell (PPC). Both  $L_x$  and  $\delta x$  are chosen so that  $N_x$  is between  $10^2$  and  $10^3$ , depending on the number of spatial dimensions. Current computational constraints limit 2D simulations to  $N_x, N_y = 10240$  and 3D simulations to  $N_x, N_y, N_z = 512$ .

The spatial grid is made up of  $N + 2$  mesh points which are the centre of each of the  $N$  cells in the simulation, including two 'ghost' cells at each end of the system. All of the electromagnetic fields and source terms (currents and densities) are discretised to these mesh points. Typically we use a staggered grid system, where  $\mathbf{E}$ ,  $\rho$ ,  $\mathbf{J}$  and  $p$  are known on the vertices of one grid and  $\mathbf{B}$  is known on the vertices of the second grid. These staggered grids ensure that  $\nabla \times \mathbf{E}$  be given correctly on both grids. Similarly, the particles and fields are discretised in time and stepped forward with a constant timestep,  $dt = \omega_i \delta t$ . The particle positions and fields are known at the beginning of each timestep and velocities at each half timestep, in a leapfrog fashion. The timestep must be small enough to resolve the problem of interest - most phenomena include low-frequency  $\omega \ll \Omega_i$  effects, so the timestep is usually limited to  $\Omega_i \delta t \leq 0.2$  so that ion gyromotion is resolved. There is also a requirement for numerical stability that particle increments are some fraction of the computational cell per timestep:  $v_{max} \delta t \leq \delta x / 2$ , where  $v_{max}$  is the maximum speed of the ions.

### 3.2. Ion Dynamics using Particle-in-Cell Methods

Ion dynamics in hybrid simulations are treated using PIC methods. To advance the particles forward in time, we first advance the velocity a full timestep from  $\mathbf{v}_i^{N-1/2}$  to  $\mathbf{v}_i^{N+1/2}$  using:

$$\mathbf{v}_i^{N+1/2} = \mathbf{v}_i^{N-1/2} + \frac{q_i \delta t}{m_i} \left( \mathbf{E}^N + \frac{\mathbf{v}_i^N \times \mathbf{B}^N}{c} \right) - \frac{q_i \delta t}{m_i} \eta \mathbf{J}^N. \quad (12)$$

where  $N$  is the timestep. The two last terms in this equation represent an effective electric field that accelerates the ions. This equation requires the knowledge of  $\mathbf{v}_i^N$  implicitly, which we calculate using  $\mathbf{v}_i^N = 1/2(\mathbf{v}_i^{N-1/2} + \mathbf{v}_i^{N+1/2})$ . Methods such as the Boris push can be used. To solve Equation 12 for  $\mathbf{v}_i^{N+1/2}$  we first determine  $\mathbf{E}^N(\mathbf{x}_i^N)$  and  $\mathbf{B}^N(\mathbf{x}_i^N)$ , i.e., at the position of each particle, using linear interpolation of the contribution from the surrounding mesh points. Higher order methods such as cubic splines are also sometimes employed. Then the particle position can be advanced from timestep  $N$  to  $N + 1$ :

$$\mathbf{x}_i^{N+1} = \mathbf{x}_i^N + \mathbf{v}_i^{N+1/2} \delta t \quad (13)$$

Finally, we determine the charge and current density due to the new particle positions at timesteps  $N + 1$  and  $N + 1/2$ , respectively, and then at the mesh points using linear interpolation to update the fields for the next iteration. Ghost cells become important here because charge and current density can be shared between multiple cells. Any accumulation inside these cells is placed back into the physical cell of the system depending on the boundary conditions for the fields. Often, periodic boundary conditions are chosen, so that accumulation in the first ghost cell is placed into the last physical cell and vice versa. Smoothing of the density and current is also sometimes applied to reduce noise in the fields.

### 3.3. Fluid Electrons

The electrons are treated using the fluid momentum equation described above (Equation 9), using the quasi-neutrality condition and an equation of state. The quasi-neutrality approximation means that at spatial scales larger than the electron Debye length,  $\lambda_e$ ,  $n_e = n_i$ . Therefore the ion density  $n_i$  is used as a substitute for  $n_e$  in Equation 9. The choice of an equation of state typically has only a small effect on the overall solution. Typically we assume an isothermal electron temperature ( $T_e = \text{const.}$ ) or an adiabatic model:  $T_e = T_{e,0}(n_e/n_0)^{\gamma-1}$  where  $\gamma = 5/3$ .

We also need to define the resistivity,  $\eta$  to remove high-frequency effects involving electrons, which are not modelled in hybrid simulations. We can do this by introducing an anomalous electron-ion collision frequency  $\nu_{an}$  which is related to  $\eta$  through:  $\eta = 4\pi\nu_{an}/\omega_e^2$ . In dimensionless form this is  $\eta = (\nu_{an}/\omega_i)(\Omega_i/\Omega_e)$ . Often we introduce a practical resistive length  $L_\eta \leq 0.1\delta x$  as a fraction of the cell size to eliminate unwanted high-frequency noise.

### 3.4. Calculating Electromagnetic Fields

Most codes calculate the fields explicitly, although implicit methods also exist. For an explicit scheme it is straightforward to advance  $\mathbf{B}$  from time step  $N$  to  $N + 1/2$  using Faraday's law:

$$\mathbf{B}^{N+1/2} = \mathbf{B}^N - \frac{c\delta t}{2} (\nabla \times \mathbf{E}^N). \quad (14)$$

The electric field can be advanced using the electron momentum equation (Equation 9) and solving for  $\mathbf{E}$ :

$$\mathbf{E}^{N+1/2} = -\frac{\mathbf{V}_i^{N+1/2} \times \mathbf{B}^{N+1/2}}{c} - \frac{\nabla p_e^{N+1/2}}{q_i n_i^{N+1/2}} - \frac{\mathbf{B}^{N+1/2} \times (\nabla \times \mathbf{B}^{N+1/2})}{4\pi q_i n_i^{N+1/2}}. \quad (15)$$

Here,  $\mathbf{V}_i$  is the fluid ion velocity and  $n_i^{N+1/2}$  is the average of the ion density between  $n_i^N$  and  $n_i^{N+1}$ :  $n_i^{N+1}$  has just been collected when moving the ions (Equation 13) and  $n_i^N$  has been saved from the previous time step. Since  $p_e$  is only a function of the density, all the quantities in Equation 15 are known and thus  $\mathbf{E}^{N+1/2}$  can be computed. We can then use Equation 14 a second time to determine  $\mathbf{B}^{N+1}$ . To advance the electric field to  $\mathbf{E}^{N+1}$  is not straightforward, however. If we use Equation 15 we need to know  $\mathbf{V}_i^{N+1}$ . Most hybrid codes then utilise different algorithms to determine  $\mathbf{V}_i^{N+1}$  and hence,  $\mathbf{E}^{N+1}$ . The simplest approach is a linear extrapolation of  $\mathbf{V}_i^{N+1/2}$  to  $\mathbf{V}_i^{N+1}$  which just requires keeping  $\mathbf{V}_i^{N-1/2}$

from the previous time step. See Winske et al. (2003) for a discussion of more complicated algorithms. Often more advanced methods are used to advance the magnetic field due to the presence of short wavelength whistler noise. To reduce this noise the timestep for advancing the magnetic field can be smaller than for the advancement of the particle positions and velocities. These methods often employ schemes such as the 4th-order Runge-Kutta algorithm to determine  $\mathbf{B}^{N+\theta}$  using subcycling at timestep  $\delta t' = \delta t/\theta$  to eventually obtain  $\mathbf{B}^{N+1}$ .

### 3.5. Initialisation

To initialise the simulation we need to load the particles in both physical and velocity space and set the electromagnetic fields at time  $t = 0$ . To load the particles in physical space, we set the initial densities to be uniform so that the particles are spread uniformly throughout the simulation domain. Different numbers of particles can be used to represent different ion species. To load the particles in velocity space we assume an initial velocity distribution,  $F_s(\mathbf{v})$ , often a Maxwellian, and determine the particle velocities randomly using a loading function  $R_s(\mathbf{v})$  that varies between 0 and 1. Electric and magnetic field fluctuations are usually assumed to be zero.

## 4. Analysing Simulation Data

Simulations are performed using a spatial grid and so do not use Taylor's hypothesis that is often used in analysing in-situ data from the solar wind (Taylor, 1938), meaning we can study the full 3D structure of the turbulence. From solar wind results reported in the literature, we often study the fluctuations with wavevectors parallel and perpendicular to the local mean magnetic field,  $k_{\parallel}$  and  $k_{\perp}$ , respectively. But here, we perform integrations over the simulation domain to study the fluctuations in full  $k_{\perp} - k_{\parallel}$  space, following Franci et al. (2018). We assume the power spectrum of magnetic field fluctuations is axis-symmetric. That is, they follow cylindrical symmetry with respect to the background magnetic field. In cylindrical coordinates:  $k_{\perp} = \sqrt{k_x^2 + k_y^2}$ ,  $k_{\parallel} = k_z$ , and  $\phi = \arctan(k_y/k_x)$  and varies between 0 and  $2\pi$ . In mathematical notation, the 3D power spectrum of the magnetic field,  $\mathbf{B}$ , is defined as:

$$P_{3D}(k_{\perp}, k_{\parallel}) = \frac{1}{k_{\perp}} \sum_{k_{\perp} = \sqrt{k_x^2 + k_y^2}} |\delta \mathbf{B}(\mathbf{k})|^2, \quad (16)$$

where  $|\delta \mathbf{B}|^2 = \sum_{i=j} \hat{B}_i \hat{B}_j^*$ ,  $i, j = x, y, z$  and the hat denotes Fourier transform. This equation represents the energy of the Fourier modes averaged over concentric rings normal to  $k_{\parallel}$  defined by  $k_{\perp}$  to  $k_{\perp} + dk_{\perp}$ , i.e., the sum of the power in the modes contained within each ring divided by the number of modes. Here,  $dk_{\perp} = 2\pi/L_{\text{box}}$ . The factor  $1/k_{\perp}$  accounts for the area of the rings scaling with  $dA = 2\pi k_{\perp} dk_{\perp}$ . To obtain the 2D spectrum, we need to integrate the 3D spectrum over all angles  $\phi$ :

$$P_{2D}(k_{\perp}, k_{\parallel}) = \int_0^{2\pi} P_{3D}(k_{\perp}, k_{\parallel}) k_{\perp} d\phi = 2\pi k_{\perp} P_{3D}(k_{\perp}, k_{\parallel}). \quad (17)$$

The extra factor of  $k_{\perp}$  inside the integral arises from the unit element of  $\mathbf{k}$ :  $d\mathbf{k} = dk_{\perp} \hat{k}_{\perp} + k_{\perp} d\phi \hat{\phi} + dk_{\parallel} \hat{k}_{\parallel}$ . To obtain the one-dimensional parallel and perpendicular spectra we further integrate the 2D spectrum:

$$P_{1D,\perp}(k_{\perp}) = \int_0^{\infty} P_{2D}(k_{\perp}, k_{\parallel}) dk_{\parallel} = \sum_{k_{\parallel}} P_{2D} \Delta k_{\parallel}, \quad (18)$$

$$P_{1D,\parallel}(k_{\parallel}) = \int_0^{\infty} P_{2D}(k_{\perp}, k_{\parallel}) dk_{\perp} = \sum_{k_{\perp}} P_{2D} \Delta k_{\perp}, \quad (19)$$

Since  $P_{2D}$  and  $P_{1D}$  are spectral densities, i.e.,  $S(k) = P(k)dk$ , when plotting in logarithmic space we need to account for extra factors of  $k$ :  $d(\log_{10} k) = dk/(k \log_{10} 10)$  (see He et al., 2012b). Therefore,

$$P_{2D}^{\log} d(\log_{10} k_{\perp}) d(\log_{10} k_{\parallel}) = P_{2D}^{\text{lin}} k_{\perp}(\log_{10} 10) d(\log_{10} k_{\perp}) k_{\parallel}(\log_{10} 10) d(\log_{10} k_{\parallel}), \quad (20)$$

$$P_{1D}^{\log} d(\log_{10} k) = P_{1D}^{\text{lin}} k(\log_{10} 10) d(\log_{10} k), \quad (21)$$

To compare the analysis of in-situ data from the solar wind by Woodham et al. (2018), we compute power spectra of the magnetic field using the methods outlined above. To investigate the properties of the break in the power spectrum and magnetic helicity, we focus on the 1D perpendicular spectrum. To determine the break in the spectrum,  $k_b$ , we fit the following equation to the spectrum using a sliding window of 10 points in  $k$ , shifted by one point each time:

$$\log_{10}(P_{1D}) = \alpha \log_{10}(k) + c. \quad (22)$$

Here, we fit straight lines in logarithmic space where  $\alpha$  is the spectral exponent and  $c$  is the intercept. Using the series of fits, we identify the fits starting at small  $k$  up to the last fit where  $\alpha = -5/3$  within 10%, as well as the fits within 10% of the minimum exponent at large  $k$ . We then determine a value for  $\alpha$  and  $c$  for the inertial range (1) and ion-kinetic range (2) by fitting a second time two power laws to the two ranges of the spectrum, respectively. The break in the spectrum is then the point at which the two lines intersect:

$$\log_{10}(k_b) = \frac{c_2 - c_1}{\alpha_1 - \alpha_2}. \quad (23)$$

To determine the magnetic helicity from simulation data we follow Howes and Quataert (2010). The helicity is defined as:  $H_m(\mathbf{k}) = \delta\mathbf{A}(\mathbf{k}) \cdot \delta\mathbf{B}^*(\mathbf{k})$ , where  $\mathbf{A} = \nabla \times \mathbf{B}$  is the magnetic vector potential and  $\delta\mathbf{A} = i(\mathbf{k} \times \delta\mathbf{B})/k^2$  assuming the Coulomb gauge:  $\nabla \cdot \mathbf{A} = 0$ . The helicity is then:

$$H_m(\mathbf{k}) = i \frac{\delta B_y \delta B_z^* - \delta B_y^* \delta B_z}{k_x} \equiv i \frac{\delta B_z \delta B_x^* - \delta B_z^* \delta B_x}{k_y} \equiv i \frac{\delta B_x \delta B_y^* - \delta B_x^* \delta B_y}{k_z}. \quad (24)$$

The normalised magnetic helicity is then defined as  $\sigma_m(\mathbf{k}) = k H_m(\mathbf{k}) / |\delta\mathbf{B}(\mathbf{k})|^2$  and takes a value between -1 and +1 for a right and left-handed circularly polarised wave, respectively. A value  $|\sigma_m| < 1$  indicates a coherent handedness of the fluctuations, whereas  $\sigma_m = 0$  indicates no coherent polarisation (Gary, 1986). To calculate 2D and 1D helicity spectra in a similar fashion to the power spectrum, we use:

$$\sigma_m(\mathbf{k}) = \frac{k \langle H_m(\mathbf{k}) \rangle}{\langle |\delta\mathbf{B}(\mathbf{k})|^2 \rangle}, \quad (25)$$

where the angular brackets represent the integration process discussed above, for example,  $\sigma_{2D} = k H_{2D} / P_{2D}$  where  $k = \sqrt{k_\perp^2 + k_\parallel^2}$ . Since helicity is not a spectral density, we do not need to include any extra factors of  $k$  when plotting spectra.

## 5. Simulation Set-up

We present here the results of our analysis of three-dimensional high-resolution hybrid simulations using kinetic ions and a massless electron fluid. We use the H3D hybrid code (Karimabadi et al., 2006; Podesta and Roytershteyn, 2017; Fu et al., 2018), which is optimised for turbulence simulators. This code advances the particles using the Boris push algorithm, the magnetic field using subcycling with a 4th-order Runge-Kutta scheme, and the electric field using a linear extrapolation of  $\mathbf{V}_i$ . The simulation is set-up with a  $N_x = N_y = N_z/3 = 512$  cubic grid with dimensions  $L_x = L_y = L_z/3 = 128d_i$ , making the box elongated along the z-direction. The corresponding spacing between grid points is  $\delta x = \delta y = \delta z = 0.25d_i$ . There is an initial uniform background magnetic field orientated along the z-direction,  $\mathbf{B}_0 = B_0 \hat{\mathbf{z}}$ . We use 512 marker particles per cell (PPC) to represent protons. We use a timestep of  $\delta t \Omega_i = 0.01$  and to conserve total energy in the system we use a small resistivity of  $\eta = 10^{-7} 4\pi / \omega_{pi}$ . We set the initial ion temperature so that  $\beta_i = 8\pi n_0 T_i / B_0^2 = 1$ , which is typical for fast solar wind conditions at 1 AU. The box is given periodic boundary conditions for fields and particles, and initially, we set  $T_e / T_i = 1/2$ . The electrons follow the adiabatic equation of state with  $\gamma = 5/3$ :

$$T_e / n_e^{\gamma-1} = \text{const} \quad (26)$$

The elongation of the simulation box allows the development of an anisotropic ( $k_\perp \gg k_\parallel$ ) MHD turbulent cascade (Perez and Boldyrev, 2010). To initiate this forward cascade of energy we inject pairs of critically balanced

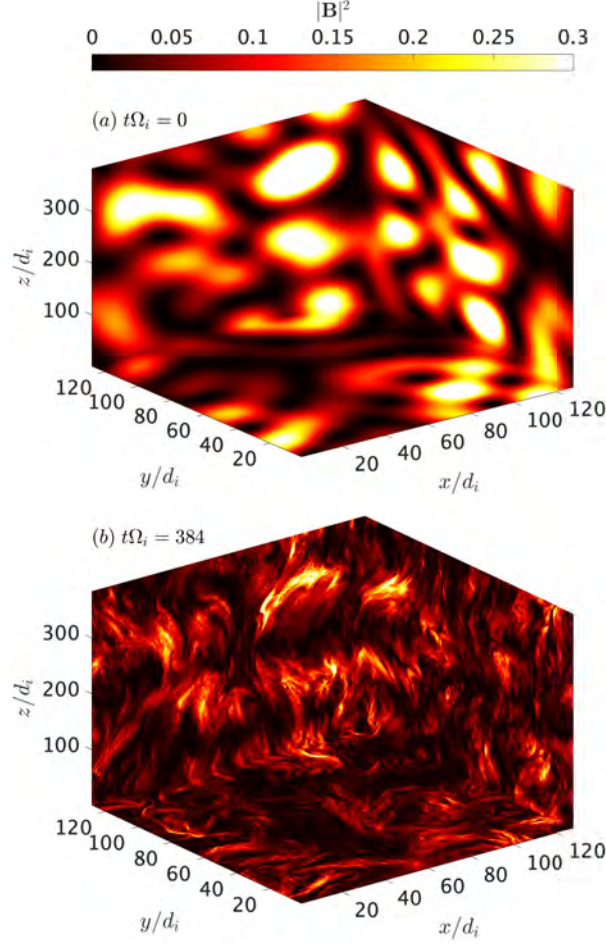


Figure 1: (a) Snapshots of the fluctuating magnetic field,  $|\mathbf{B}|^2$ , at the box faces for (a)  $t\Omega_i = 0$  and (b)  $t\Omega_i = 384$ , the Alfvén time,  $t_A$ .

(Goldreich and Sridhar, 1995) counter-propagating long wavelength Alfvén waves into the box at time  $t = 0$ . The fluctuating magnetic field of these waves is (Podesta and Roytershteyn, 2017):

$$\Delta\mathbf{B} = \mathbf{B} - \mathbf{B}_0 = \sum_m \Delta\mathbf{B}_m \cos(\mathbf{k}_m \cdot \mathbf{x} + \phi_m), \quad (27)$$

Here, the sum consists of 32 terms with random phases,  $\phi_m$ . The wavevectors are given by:

$$\mathbf{k}_m = \left( \pm \frac{2\pi m_1}{L_x}, \pm \frac{2\pi m_2}{L_y}, \frac{2\pi m_3}{L_z} \right), \quad (28)$$

where the indices  $m_1, m_2, m_3 = 1, 2$ . The amplitude of the waves, given by  $\Delta\mathbf{B}_m$ , are chosen so that  $\mathbf{k}_m \cdot \Delta\mathbf{B}_m = 0$  and  $\mathbf{B}_0 \cdot \Delta\mathbf{B}_m = 0$  to ensure Alfvénic perturbations. The magnitude of the waves,  $|\Delta\mathbf{B}_m|$ , are the same for every wavevector and normalised so that  $\langle \Delta\mathbf{B}^2 \rangle / B_0^2 = L_x^2 / L_z^2$ , where  $\langle \Delta\mathbf{B}^2 \rangle$  is a volume average over the whole simulation domain. The perturbation in the bulk velocity field is then zero since the fluctuations due to counter-propagating Alfvén waves will completely cancel. These waves interact non-linearly and shear, producing daughter waves that will initiate the forward cascade. These waves are injected at a driving scale that is much larger than kinetic scales ( $kd_i \sim 1$ ) and

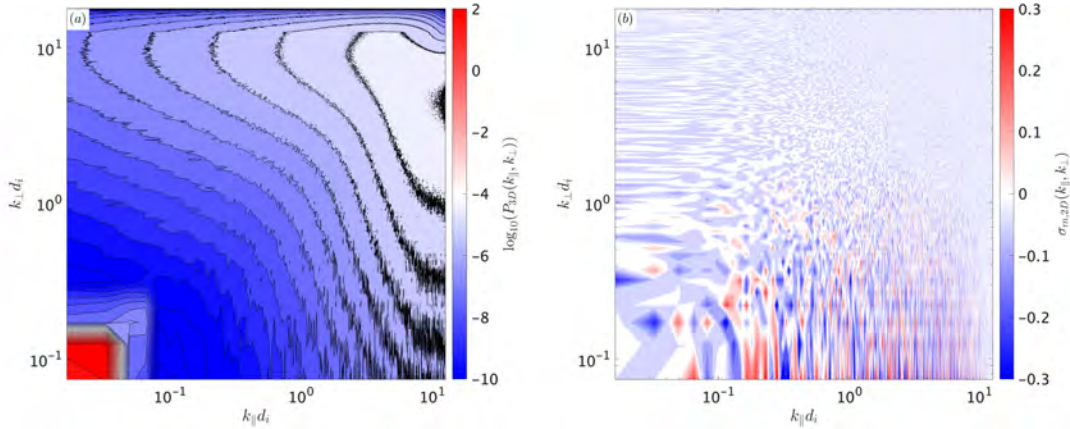


Figure 2: (a) Two-dimensional power spectrum of magnetic field fluctuations in the simulation box  $t\Omega_i = 0$ , given by  $P_{2D}(k_{\parallel}, k_{\perp})$ . (b) The corresponding two-dimensional magnetic helicity spectrum,  $\sigma_{m,2D}(k_{\parallel}, k_{\perp})$ .

so will allow an inertial range to develop over at least an order of magnitude in  $k$  before a break in the spectrum is observed, the focus of this work.

## 6. Results

In Figure 1 we show snapshots of the fluctuating magnetic field,  $|\mathbf{B}|^2$ , at the box faces for times  $t\Omega_i = 0$  and  $t\Omega_i = 384$ . We choose the latter time because  $t = \tau_A$  where  $\tau_A = L_z/v_A$  is the Alfvén crossing time so that the initial injected waves have travelled across the simulation box at least once. We can see in panel (a) the large-scale Alfvén waves injected into the box and in panel (b) these waves have interacted with other waves, leading to a forward cascade that produces smaller and smaller eddies, vortices and filament-like structures. We explore these features in spectral space in Figures 2 and 3, showing the two-dimensional power spectrum of magnetic field fluctuations,  $P_{2D}(k_{\parallel}, k_{\perp})$ , and the corresponding two-dimensional magnetic helicity spectrum,  $\sigma_{m,2D}(k_{\parallel}, k_{\perp})$ . From Figure 2 ( $t\Omega_i = 0$ ), we see in panel (a) the injected power of the large-scale Alfvén waves at small wavenumbers,  $k_{\perp}d_i \sim 0.1$  and  $k_{\parallel}d_i \sim 0.02$ , and very little power at higher wavenumbers. Likewise, in the helicity spectrum in panel (b) we see no coherent signature in wavenumber space, and in the parallel direction the helicity oscillates about zero.

In Figure 3 we show the same spectral plots for  $t\Omega_i = 384$ . Here, we can see that the power in the magnetic field fluctuations initially injected at small wavenumbers has cascaded towards higher wavenumbers, primarily in the perpendicular direction, as expected for anisotropic Alfvénic turbulence which we also see in the solar wind. In the helicity spectrum, we see a coherent signature across both perpendicular and parallel wavenumbers. This signature is positive indicating that the fluctuations are left-hand polarised, and could be AIC waves. The signature extends towards smaller wavenumbers  $kd_i \sim 0.1$ , but is strongest at  $k_{\perp}d_i \sim 1$  and  $k_{\parallel}d_i = 0.6$ . It is also interesting that this signature is co-located with the steepest gradient in panel (a), towards higher parallel wavenumbers, where the power drops significantly with increasing  $k_{\parallel}$ . This signature may be a sign of dissipation of the fluctuations at these scales, although more investigation is needed.

While we use  $t\Omega_i = 384$  to study the turbulence, the time of maximum dissipation (Podesta and Roytershteyn, 2017) is  $t\Omega_i \simeq 230$ . We also plot two-dimensional spectra for this time in Figure 4. In panel (a) we see that the power spectrum is almost identical to that at  $t\Omega_i = 384$ . However, the signature in the helicity spectrum is dominantly negative, suggesting the presence of right-handed fluctuations at proton kinetic scales that may be indicative of KAWs. This result suggests that the helicity signature is highly localised in both  $k$ -space and time, and is constantly evolving as the turbulence evolves. Solar wind data are consistent with this observation and suggest this signature is related in some way to the damping of fluctuations at these scales and subsequent proton heating. Since signatures of dissipation have been found to be bursty, this is also consistent with the continuously evolving helicity signature we observe (e.g., Mangeney, 2012).



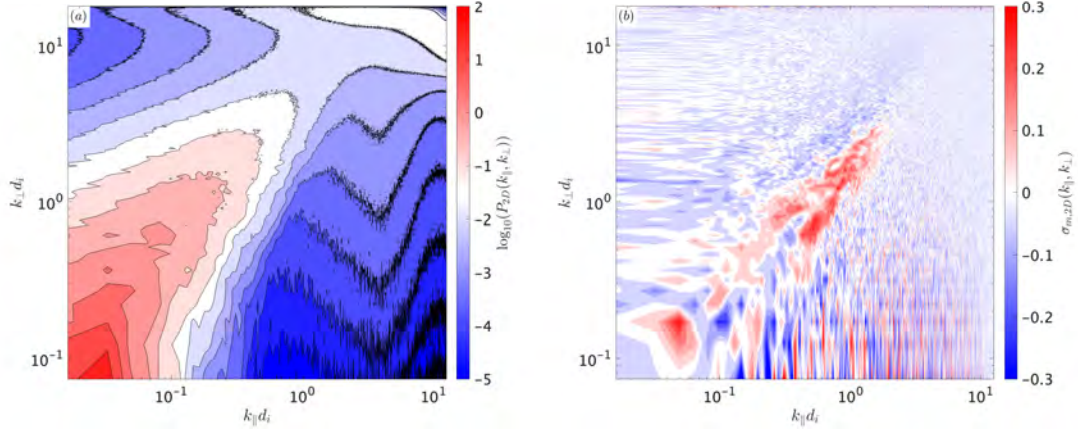


Figure 3: (a) Two-dimensional power spectrum of magnetic field fluctuations in the simulation box  $t\Omega_i = 384$ , given by  $P_{2D}(k_{||}, k_{\perp})$ . (b) The corresponding two-dimensional magnetic helicity spectrum,  $\sigma_{m,2D}(k_{||}, k_{\perp})$ .

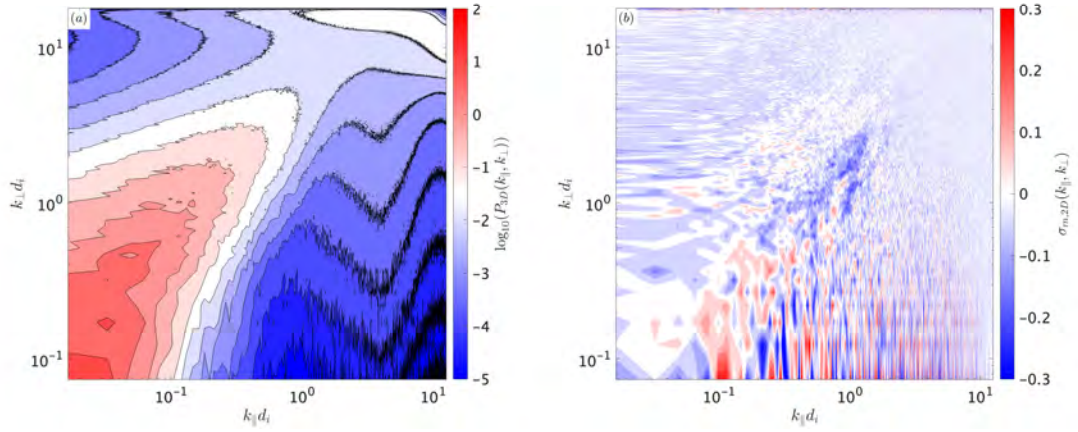


Figure 4: (a) Two-dimensional power spectrum of magnetic field fluctuations in the simulation box  $t\Omega_i \approx 230$ , given by  $P_{2D}(k_{||}, k_{\perp})$ . (b) The corresponding two-dimensional magnetic helicity spectrum,  $\sigma_{m,2D}(k_{||}, k_{\perp})$ .

Finally, in Figure 5 we show the one-dimensional perpendicular and parallel power spectra,  $P_{1D,\perp}(k_{\perp})$  and  $P_{1D,\parallel}(k_{||})$ , for  $t\Omega_i = 384$ . We find that in the inertial range the perpendicular spectrum is close to  $k_{\perp}^{-5/3}$  and the parallel spectrum close to  $k_{||}^{-2}$ , as expected from critical balance. Close to  $k_{\perp}d_i \sim 1$ , the spectrum steepens as expected from solar wind measurements. The location of the break in the perpendicular spectrum when compared with Figure 3 (b) is within the centre of the coherent peak in helicity, which also suggests that the presence of coherent circularly polarised fluctuations at these scales is linked to dissipation or a steepening in the power spectrum. We intend to investigate this result in future work further. At the highest wavenumbers, the spectra both flatten and increase, which is likely due to numerical and high-frequency whistler noise and is not physical.

We do not plot one-dimensional helicity spectra here since the integration to reduce the 2D spectrum does not capture the localised coherent helicity signature well and so we are unable to quantify the helicity signature this way. However, if we take a cut of the helicity spectra at  $k_{||}d_i = 1$ , we can produce helicity spectra that are representative of solar wind measurements. We show two of these cuts for  $t\Omega_i \approx 230$  and  $t\Omega_i = 384$  in Figure 6. We can see that for both cuts the helicity oscillates about zero at small  $k_{\perp}$ , and at  $k_{\perp}d_i \sim 1$  a coherent signature appears, with opposite sign and similar magnitude of about 0.2. Then at a higher  $k_{\perp}$ , the helicity returns to zero. These helicity spectra are very similar to those observed in the fast solar wind by Woodham et al. (2018). The next step in this analysis is to

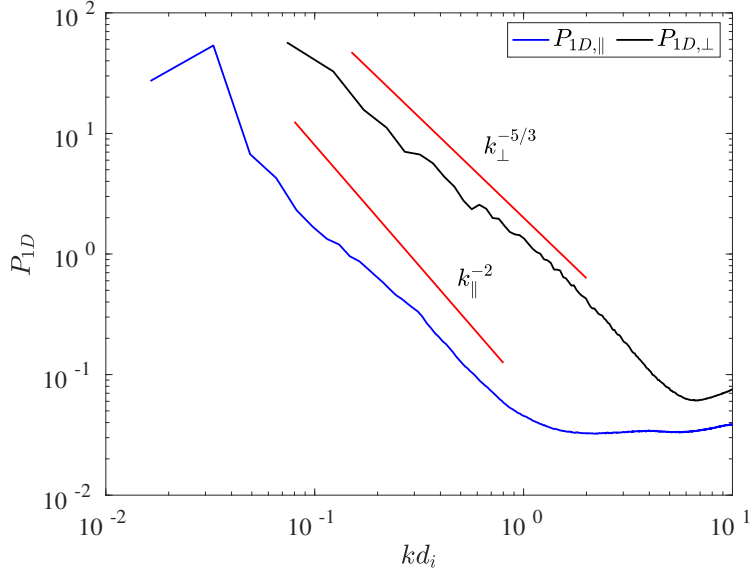


Figure 5: One-dimensional perpendicular  $P_{1D,\perp}(k_{\perp})$  and parallel  $P_{1D,\parallel}(k_{\parallel})$  power spectra at  $t\Omega_i = 384$ . The red lines show the reference power laws  $k_{\perp}^{-5/3}$  and  $k_{\parallel}^{-2}$  as expected from critical balance.

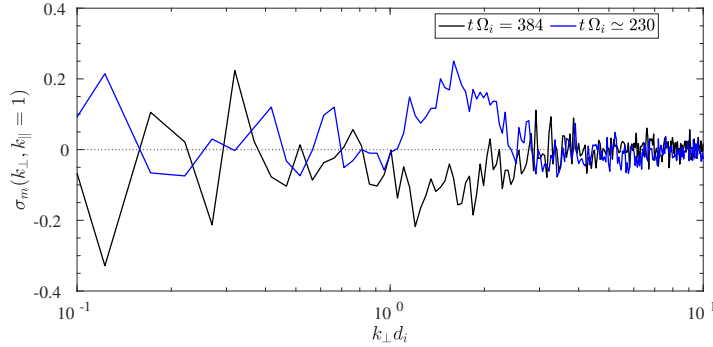


Figure 6: Cuts of the two-dimensional magnetic helicity spectrum  $\sigma_{m,2D}(k_{\parallel}, k_{\perp})$  at  $k_{\parallel} d_i = 1$  for  $t\Omega_i = 384$  and  $t\Omega_i \approx 230$ .

determine how the 2D helicity spectrum appears if it were measured by a single spacecraft.

## 7. Conclusions

In this report, we present initial results from our analysis of plasma turbulence using a three-dimensional high-resolution hybrid simulation. We use our experience of analysing in-situ solar wind data in order to develop the necessary tools to analyse simulation data and explore the physical processes at proton kinetic scales. Initial results are promising and suggest that the coherent helicity signature seen at proton kinetic scales is associated with the break in the power spectrum, as suggested by in-situ data analysis (Woodham et al., 2018), and linked to the dissipation of the turbulent fluctuations. This research is currently ongoing, and we plan further work to compare our simulation results with in-situ data. For example, spectra from single spacecraft are similar to integrating the simulation spectrum along the direction perpendicular to the direction of plasma flow past the spacecraft. Therefore, we plan to try integrating along  $k(\theta)$  where  $\theta$  is the angle from the z-direction to explore how the simulation results appear if they were measured by a single spacecraft. Initial investigation of these ideas from Figure 6 is promising. We also aim to identify any

dissipation mechanisms associated with the coherent helicity signature, as well as explore how changing plasma beta,  $\beta_i$ , affects the results presented here.

Large-scale simulations such as those presented here are challenging to set up and require extensive computational resources. Simulations retain full three-dimensional information of the turbulent fluctuations, whereas solar wind measurements lose some of this information during the integration to a one-dimensional spectrum due to Taylor's hypothesis. Also, by tracing sample particles and analysing their energisation processes, we may gain further insights into the wave-particle interactions during the dissipation. Therefore, by understanding simulation results that are comparable to solar wind measurements, we can better understand turbulent phenomena in collisionless plasmas and apply our knowledge to other astrophysical plasmas.

## 8. Acknowledgments

L.W. would like to thank J. Podesta and V. Roytershteyn for supplying the data from their simulation run, the Center for Space and Earth Sciences at Los Alamos National Laboratory for hosting the Space Weather Summer School, and J. Woodroffe for his support during the school.

## References

- Alexandrova, O., Chen, C.H.K., Sorriso-Valvo, L., Horbury, T.S., Bale, S.D., 2013. Solar wind turbulence and the role of ion instabilities. *Space Science Reviews* 178, 101–139. 1306.5336.
- Biskamp, D., 2003. *Magnetohydrodynamic Turbulence*. Cambridge University Press.
- Bruno, R., Carbone, V., 2013. The solar wind as a turbulence laboratory. *Living Reviews in Solar Physics* 10.
- Bruno, R., Telloni, D., 2015. Spectral Analysis of Magnetic Fluctuations at Proton Scales from Fast to Slow Solar Wind. *The Astrophysical Journal Letters* 811, L17. 1509.04866.
- Bruno, R., Trenchi, L., 2014. Radial Dependence of the Frequency Break Between Fluid and Kinetic Scales in the Solar Wind Fluctuations. *The Astrophysical Journal Letters* 787, L24.
- Cerri, S.S., Califano, F., 2017. Reconnection and small-scale fields in 2D-3V hybrid-kinetic driven turbulence simulations. *New Journal of Physics* 19, 0–15.
- Cerri, S.S., Califano, F., Jenko, F., Told, D., Rincon, F., 2016. Subproton-Scale Cascades in Solar Wind Turbulence: Driven Hybrid-Kinetic Simulations. *The Astrophysical Journal Letters* 822, L12. 1604.07674.
- Cerri, S.S., Franci, L., Califano, F., Landi, S., Hellinger, P., 2017a. Plasma turbulence at ion scales: a comparison between PIC and Eulerian hybrid-kinetic approaches. *Journal of Plasma Physics* 83, 1–19. 1703.02443.
- Cerri, S.S., Kunz, M.W., Califano, F., 2018. Dual phase-space cascades in 3D hybrid-Vlasov-Maxwell turbulence. 1802.06133.
- Cerri, S.S., Servidio, S., Califano, F., 2017b. Kinetic cascade in solar-wind turbulence: 3D3V hybrid-kinetic simulations with electron inertia. *The Astrophysical Journal Letters* 846, L18. 1707.08429.
- Chen, C.H.K., 2016. Recent progress in astrophysical plasma turbulence from solar wind observations. *Journal of Plasma Physics* 82, 1–28. 1611.03386.
- Chen, C.H.K., Horbury, T.S., Schekochihin, A.A., Wicks, R.T., Alexandrova, O., Mitchell, J., 2010a. Anisotropy of Solar Wind Turbulence between Ion and Electron Scales. *Physical Review Letters* 104, 255002. 1002.2539.
- Chen, C.H.K., Wicks, R.T., Horbury, T.S., Schekochihin, A.A., 2010b. Interpreting Power Anisotropy Measurements in Plasma Turbulence. *The Astrophysical Journal* 711, L79–L83.
- Cranmer, S.R., Matthaeus, W.H., Breech, B.A., Kasper, J.C., 2009. Empirical Constraints on Proton and Electron Heating in the Fast Solar Wind. *The Astrophysical Journal* 702, 1604–1614. 0907.2650.
- Elsasser, W.M., 1950. The Hydromagnetic Equations. *Physical Review* 79, 183.
- Franci, L., Cerri, S.S., Califano, F., Landi, S., Papini, E., Verdini, A., Matteini, L., Jenko, F., Hellinger, P., 2017. Magnetic reconnection as a driver for a sub-ion scale cascade in plasma turbulence. *The Astrophysical Journal Letters* 850, L16. 1707.06548.
- Franci, L., Landi, S., Matteini, L., Verdini, A., Hellinger, P., 2015a. High-resolution hybrid simulations of kinetic plasma turbulence at proton scales. *Astrophysical Journal* 812, 21. 1506.05999.
- Franci, L., Landi, S., Matteini, L., Verdini, A., Hellinger, P., 2016. Plasma Beta Dependence of the Ion-Scale Spectral Break of Solar Wind Turbulence: High-Resolution 2D Hybrid Simulations. *The Astrophysical Journal* 833, 91. 1610.05158.
- Franci, L., Landi, S., Verdini, A., Matteini, L., Hellinger, P., 2018. Solar Wind Turbulent Cascade from MHD to Sub-ion Scales: Large-size 3D Hybrid Particle-in-cell Simulations. *The Astrophysical Journal* 853, 26.
- Franci, L., Verdini, A., Matteini, L., Landi, S., Hellinger, P., 2015b. Solar Wind Turbulence from MHD to Sub-ion Scales: High-resolution Hybrid Simulations. *Astrophysical Journal Letters* 804, 1–5. 1503.05457.
- Frisch, U., 1995. *Turbulence: The Legacy of A.N. Kolmogorov*. Cambridge University Press.
- Fu, X., Li, H., Guo, F., Li, X., Roytershteyn, V., 2018. Parametric Decay Instability and Dissipation of Low-frequency Alfvén Waves in Low-beta Turbulent Plasmas. *The Astrophysical Journal* 855, 139. 1710.04149.
- Galtier, S., 2006. Wave turbulence in incompressible Hall magnetohydrodynamics. *Journal of Plasma Physics* 72, 721–769. 0608227.
- Gary, S.P., 1986. Low-frequency waves in a high-beta collisionless plasma: polarization, compressibility and helicity. *Journal of Plasma Physics* 35, 431–447.

- Gary, S.P., 2015. Short-wavelength plasma turbulence and temperature anisotropy instabilities: recent computational progress. *Philosophical Transactions of the Royal Society A: Mathematical, Physical and Engineering Sciences* 373, 20140149–20140149.
- Goldreich, P., Sridhar, S., 1995. Toward a theory of interstellar turbulence II: Strong Alfvénic turbulence. *The Astrophysical Journal* 438, 763.
- Goldstein, M.L., Roberts, D.A., Fitch, C.A., 1994. Properties of the fluctuating magnetic helicity in the inertial and dissipation ranges of solar wind turbulence. *Journal of Geophysical Research* 99, 11,519–11,538.
- Goldstein, M.L., Roberts, D.A., Matthaeus, W.H., 1995. Magnetohydrodynamic turbulence in the solar wind. *Annual Review of Astronomy and Astrophysics* 33, 283–325.
- Habbal, S.R., Woo, R., Fineschi, S., O’Neal, R., Kohl, J., Noci, G., Korendyke, C., 1997. Origins of the Slow and the Ubiquitous Fast Solar Wind. *The Astrophysical Journal* 489, L103–L106. 9709021.
- Hamilton, K., Smith, C.W., Vasquez, B.J., Leamon, R.J., 2008. Anisotropies and helicities in the solar wind inertial and dissipation ranges at 1 AU. *Journal of Geophysical Research: Space Physics* 113, A01106.
- He, J., Marsch, E., Tu, C.Y., Yao, S., Tian, H., 2011. Possible Evidence of Alfvén-Cyclotron Waves in the Angle Distribution of Magnetic Helicity of Solar Wind Turbulence. *The Astrophysical Journal* 731, 85.
- He, J., Tu, C.Y., Marsch, E., Yao, S., 2012a. Do Oblique Alfvén/Ion-Cyclotron or Fast-Mode/Whistler Waves Dominate the Dissipation of Solar Wind Turbulence Near the Proton Inertial Length? *The Astrophysical Journal Letters* 8.
- He, J., Tu, C.Y., Marsch, E., Yao, S., 2012b. Reproduction of the Observed Two-Component Magnetic Helicity in Solar Wind Turbulence By a Superposition of Parallel and Oblique Alfvén Waves. *The Astrophysical Journal* 749, 86.
- Hellinger, P., Matteini, L., Landi, S., Verdini, A., Franci, L., Trávníček, P.M., 2015. PLASMA TURBULENCE AND KINETIC INSTABILITIES AT ION SCALES IN THE EXPANDING SOLAR WIND. *The Astrophysical Journal* 811, L32. 1508.03159.
- Horbury, T.S., Forman, M.A., Oughton, S., 2008. Anisotropic scaling of magnetohydrodynamic turbulence. *Physical Review Letters* 101. 0807.3713.
- Howes, G.G., Quataert, E., 2010. On the Interpretation of Magnetic Helicity Signatures in the Dissipation Range of Solar Wind Turbulence. *The Astrophysical Journal Letters* 709, L49–L52. arXiv:0910.5023v1.
- Jian, L.K., Russell, C.T., Luhmann, J.G., Strangeway, R.J., Leisner, J.S., Galvin, A.B., 2009. ION CYCLOTRON WAVES IN THE SOLAR WIND OBSERVED BY STEREO NEAR 1 AU. *The Astrophysical Journal* 701, L105–L109.
- Karimabadi, H., Vu, H.X., Krauss-Varban, D., Omelchenko, Y., 2006. Global hybrid simulations of the Earth’s magnetosphere, in: *Numerical Modeling of Space Plasma Flows*, ASP Conference Series, pp. 257–263.
- Kiyani, K.H., Osman, K.T., Chapman, S.C., 2015. Dissipation and heating in solar wind turbulence: from the macro to the micro and back again. *Philosophical Transactions of the Royal Society A: Mathematical, Physical and Engineering Sciences* 373, 20140155–20140155.
- Koval, A., Szabo, A., 2013. Magnetic field turbulence spectra observed by the wind spacecraft, in: *AIP Conference Proceedings*, pp. 211–214.
- Leamon, R.J., Smith, C.W., Ness, N.F., Matthaeus, W.H., Wong, H.K., 1998. Observational constraints on the dynamics of the interplanetary magnetic field dissipation range. *Journal of Geophysical Research* 103, 4775.
- Mangeney, A., 2012. Intermittency and regularity in the Alfvénic range of solar wind turbulence, in: *AIP Conference Proceedings*, pp. 26–41.
- Marsch, E., 2006. Kinetic physics of the solar corona and solar wind. *Living Reviews in Solar Physics* 3, 1–100.
- Marsch, E., 2012. Helios: Evolution of distribution functions 0.3–1 AU. *Space Science Reviews* 172, 23–39.
- Marsch, E., Mühlhäuser, K.H., Schwenn, R., Rosenbauer, H., Pilipp, W.G., Neubauer, F.M., 1982. Solar Wind Protons: Three-Dimensional Velocity Distributions and Derived Plasma Parameters Measured Between 0.3 and 1 AU. *Journal of Geophysical Research* 87, 52–72.
- Matthaeus, W.H., Goldstein, M.L., 1982. Measurement of the rugged invariants of magnetohydrodynamic turbulence in the solar wind. *Journal of Geophysical Research* 87, 6011–6028.
- Matthaeus, W.H., Goldstein, M.L., Smith, C.W., 1982. Evaluation of magnetic helicity in homogeneous turbulence. *Physical Review Letters* 48, 1256–1259.
- Parashar, T.N., Servidio, S., Breech, B., Shay, M.A., Matthaeus, W.H., 2010. Kinetic driven turbulence: Structure in space and time. *Physics of Plasmas* 17.
- Parashar, T.N., Servidio, S., Shay, M.A., Breech, B., Matthaeus, W.H., 2011. Effect of driving frequency on excitation of turbulence in a kinetic plasma. *Physics of Plasmas* 18.
- Parashar, T.N., Shay, M.A., Cassak, P.A., Matthaeus, W.H., 2009. Kinetic dissipation and anisotropic heating in a turbulent collisionless plasma. *Physics of Plasmas* 16. 0801.0107.
- Perez, J.C., Boldyrev, S., 2010. Strong magnetohydrodynamic turbulence with cross helicity. *Physics of Plasmas* 17, 055903. 1004.3798.
- Podesta, J.J., Gary, S.P., 2011. Magnetic Helicity Spectrum of Solar Wind Fluctuations As a Function of the Angle With Respect To the Local Mean Magnetic Field. *The Astrophysical Journal* 734, 15.
- Podesta, J.J., Roytershteyn, V., 2017. The most intense electrical currents in the solar wind: Comparisons between single-spacecraft measurements and plasma turbulence simulations. *Journal of Geophysical Research: Space Physics* 122, 6991–7004.
- Richardson, J.D., Paularena, K.I., Lazarus, A.J., Belcher, J.W., 1995. Radial Evolution of the Solar Wind from IMP-8 to Voyager 2. *Geophysical Research Letters* 22, 325–328.
- Roberts, D.A., 2010. Evolution of the spectrum of solar wind velocity fluctuations from 0.3 to 5 AU. *Journal of Geophysical Research: Space Physics* 115, A12101.
- Schekochihin, A.A., Cowley, S.C., Dorland, W., Hammett, G.W., Howes, G.G., Quataert, E., Tatsuno, T., 2009. Astrophysical Gyrokinetics: Kinetic and Fluid Turbulent Cascades in Magnetized Weakly Collisional Plasmas. *The Astrophysical Journal Supplement Series* 182, 310–377.
- Schwenn, R., 1990. Large-Scale Structure of the Interplanetary Medium, in: *Physics of the Inner Heliosphere I*. Springer Physics and Chemistry in Space, pp. 99–181.
- Servidio, S., Valentini, F., Califano, F., Veltri, P., 2012. Local kinetic effects in two-dimensional plasma turbulence. *Physical Review Letters* 108, 1–4.
- Servidio, S., Valentini, F., Perrone, D., Greco, A., Califano, F., Matthaeus, W.H., Veltri, P., 2015. A kinetic model of plasma turbulence. *Journal of Plasma Physics* 81.
- Smith, C.W., Vasquez, B.J., Hamilton, K., 2006. Interplanetary magnetic fluctuation anisotropy in the inertial range. *Journal of Geophysical*

- Research: Space Physics 111, 1–12.
- Taylor, G.I., 1938. The spectrum of turbulence. *Proceedings of the Royal Society A: Mathematical and Physical Sciences* 164, 476–490.
- Telloni, D., Bruno, R., Trenchi, L., 2015. Radial Evolution of Spectral Characteristics of Magnetic Field Fluctuations At Proton Scales. *The Astrophysical Journal* 805, 46.
- Tu, C.Y., Marsch, E., 1995. MHD structures, waves and turbulence in the solar wind: Observations and theories. *Space Science Reviews* 73, 1–210.
- Valentini, F., Califano, F., Veltri, P., 2010. Two-dimensional kinetic turbulence in the solar wind. *Physical Review Letters* 104, 1–4.
- Vasquez, B.J., 2015. HEATING RATE SCALING OF TURBULENCE IN THE PROTON KINETIC REGIME. *Astrophysical Journal* 806, 33.
- Vasquez, B.J., Markovskii, S.A., Chandran, B.D.G., 2014. Three-Dimensional Hybrid Simulation Study of Anisotropic Turbulence in the Proton Kinetic Regime. *The Astrophysical Journal* 788, 178.
- Verscharen, D., Marsch, E., Motschmann, U., Müller, J., 2012. Kinetic cascade beyond magnetohydrodynamics of solar wind turbulence in two-dimensional hybrid simulations. *Physics of Plasmas* 19. 1201.2784.
- Wicks, R.T., Alexander, R.L., Stevens, M.L., Wilson III, L.B., Moya, P.S., Viñas, A.F., Jian, L.K., Roberts, D.A., O’Modhrain, S., Gilbert, J.A., Zurbuchen, T.H., 2016. A Proton-Cyclotron Wave Storm Generated By Unstable Proton Distribution Functions in the Solar Wind. *The Astrophysical Journal* 819, 6.
- Wicks, R.T., Horbury, T.S., Chen, C.H.K., Schekochihin, A.A., 2010. Power and spectral index anisotropy of the entire inertial range of turbulence in the fast solar wind. *Monthly Notices of the Royal Astronomical Society: Letters* 407, L31–L35. 1002.2096.
- Winske, D., Yin, L., Omid, N., Karimabadi, H., Quest, K., 2003. Hybrid Simulation Codes: Past, Present and Future - A Tutorial, in: *Space Plasma Simulation*, pp. 136–165.
- Woodham, L.D., Wicks, R.T., Verscharen, D., Owen, C.J., 2018. The Role of Proton-Cyclotron Resonance as a Dissipation Mechanism in Solar Wind Turbulence: A Statistical Study at Ion-Kinetic Scales. *The Astrophysical Journal* 856, 49. 1801.07344.



Los Alamos Space Weather Summer School  
PO Box 1663, MS B241  
Los Alamos, NM 87545

<http://swx-school.lanl.gov>

